Surface modification and functionalization of natural zeolite – clinoptilolite

Kalebić, Barbara

UNIVERSITY OF BELGRADE
FACULTY OF TECHNOLOGY AND METALLURGY

and

UNIVERSITY OF ZAGREB
FACULTY OF MECHANICAL ENGINEERING AND NAVAL ARCHITECTURE

University of Belgrade

University of Zagreb

Barbara Kalebić

SURFACE MODIFICATION AND FUNCTIONALIZATION OF NATURAL ZEOLITE – CLINOPTILOLITE

International Dual Doctorate

Belgrade, 2023

UNIVERZITET U BEOGRADU
TEHNOLOŠKO-METALURŠKI FAKULTET

i

SVEUČILIŠTE U ZAGREBU
FAKULTET STROJARSTVA I BRODOGRADNJE

University of Belgrade

University of Zagreb

Barbara Kalebić

POVRŠINSKA MODIFIKACIJA I FUNKCIONALIZACIJA PRIRODNOGA ZEOLITA – KLINOPTILOLITA

međunarodni dvojni doktorat znanosti

Beograd, 2023

Mentors:

Dr. Nevenka Rajić, Full Professor
University of Belgrade, Faculty of Technology and Metallurgy

Dr. Lidija Ćurković, Full Professor
University of Zagreb, Faculty of Mechanical Engineering and Naval Architecture

Committee Members:

Dr. Nikola Škoro
University of Belgrade, Institute of Physic Belgrade

Dr. Vladimir Pavićević, Associate Professor
University of Belgrade, Faculty of Technology and Metallurgy

Dr. Maja Đolić, Assistant Professor
University of Belgrade, Faculty of Technology and Metallurgy

Dr. Davor Ljubas, Full Professor
University of Zagreb, Faculty of Mechanical Engineering and Naval Architecture

Dr. Hrvoje Cajner, Full Professor
University of Zagreb, Faculty of Mechanical Engineering and Naval Architecture

Dr. Vilko Mandić, Associate Professor
University of Zagreb, Faculty of Chemical Engineering and Technology

Dr. Nataša Novak Tušar, Full Professor
University Nova Gorica, National Institute of Chemistry

Date of defense:

September 27, 2023

Acknowledgements

First, I would like to express my gratitude to the European Commission for providing funding for the NOWELTIES project and to all those who contributed to its inception and progress. I am immensely thankful to my supervisors, Prof. Dr. Nevenka Rajić and Prof. Dr. Lidija Ćurković, for being remarkable supervisors from whom I have learned a lot. Their kindness, patience, and unwavering support throughout these three years, have been truly invaluable. I appreciate the effort and assistance of Dr. Nikola Škoro, my co-supervisor at NOWELTIES project, who introduced me to the world of plasma, facilitated my understanding of plasma physic, and helped me write the part of the dissertation related to plasma regeneration.

I want to thank everybody who worked directly or indirectly with me at the University of Belgrade: professors and colleagues from the Department of General and Inorganic Chemistry of TMF, especially to Dr. Jelena Pavlović and Dr. Jelena Dikić who provided immense help not only with the work but also outside of it, making my stay in Belgrade never-to-be-forgotten. I appreciate the help of Prof. Dragan Povrenović in thesis defense organization. I also want to thank the whole team at the Centre of Non-Equilibrium Processes for making my workdays at IPB pleasant, interesting, and enjoyable.

I would also like to acknowledge Dr. Janez Kovač, Dr. Aleksander Rečnik and Dr. Sašo Gyergyek from the Jožef Stefan Institute for their contribution to the analyses and articles writing.

At the University of Zagreb, I would like to thank Prof. Dr. Davor Ljubas for enabling me to perform the adsorption experiments in his laboratory. Many thanks to my colleagues Rea Veseli and Marko Skozrit for their assistance during the adsorption experiments at FSB. My acknowledgement to Prof. Dr. Hrvoje Cajner for his expertise in statistical analysis, which benefited the interpretation of the obtained adsorption data, Arijeta Bafti, mag. chem., and Prof. Vilko Mandić for their assistance with XRD and Raman analyses, and Dr. Marijan Marciuš from Ruđer Bošković Institute for the magnetic particles analyses.

I am grateful to have had other 13 early-stage-researchers from the NOWELTIES project as my colleagues, whose support has meant a lot to me. I am particularly happy to have had Amit Kumar in Belgrade as a colleague and friend with whom I could share my concerns as well as many memorable moments. I also want to thank Barbara Topolovec for listening to me and addressing my scientific and other concerns over the phone throughout the entire three years.

Last but not least, I truly appreciate the support I received at home. Thanks to my mother and brother for believing in me no matter what, and I am glad to have Marin, who made complex things simple.

Thank you.

Barbara

This work is supported by the European Union's Horizon 2020 research and innovation program under the Marie Skłodowska-Curie grant agreement No. 812880 – NOWELTIES ITN-EJD project.

Surface modification and functionalization of natural zeolite – clinoptilolite

ABSTRACT

The goal of the dissertation was to develop new, environmentally friendly, and economically profitable adsorbents based on natural zeolite – clinoptilolite (CLI) for the removal of the antibiotic ciprofloxacin (CIP) from aqueous solutions. CLI was chosen as it is readily available, while CIP as it is a widely used fluoroquinolone-type antibiotic.

In this study, the CLI is first modified with iron oxide nanoparticles (MAG) by two methods: 1) co-precipitation (MAG_{CP}-CLI) from a Fe(II) salt solution and 2) microwave crystallization also from Fe(II) solution (MAG_{MW}-CLI). Finally, the third modification procedure involved the deposition of graphene oxide on MAG_{MW}-CLI using ultrasonic treatment (GO-MAG_{MW}-CLI).

The CIP adsorption on the obtained adsorbents was investigated for different initial CIP concentrations, temperatures, pH values and reaction times. The design of experiment (DoE) was used to analyse the influence of these parameters on the adsorption efficiency. Using the response surface methodology and the application of the central composite design (RSM-CCF), the following was determined: the highest possible adsorbed CIP concentration (12.40 mg g^{-1}) is achieved onto GO-MAG_{MW}-CLI for an initial concentration of 48.47 mg dm^{-3} at pH = 5 and 24.78 °C, after 19.20 min.

Adsorption kinetics and mechanism were investigated by applying the most commonly used kinetic and adsorption isotherms models at 10, 15 and 20 °C and pH = 5. For all investigated temperatures, the adsorption kinetics follows the pseudo-second-order Lagergren equation, while the mechanism of the adsorption process is best described by the Langmuir isotherm. The adsorption mechanism of CIP for the investigated adsorbents includes ion exchange reaction and electrostatic attraction between the negatively charged aluminosilicate lattice of the adsorbent and CIP-cations.

Modification of CLI with mixed iron oxides (12 wt.%) conferred magnetic properties to the adsorbents, enabling their separation from the liquid phase by an external magnetic field. Also, the presence of graphene oxide on the surface contributed to an increase in the specific surface area and adsorption capacity.

For the adsorbents' regeneration, a novel method of non-thermal plasma (NTP) was applied. In this work, NTP was tested for the first time to remove organic species from the surface of minerals. Various reactive gas species formed during NTP treatment contributed to the mineralization of adsorbed CIP. The results showed that in five consecutive adsorption/regeneration cycles, more than 90% of the adsorption capacity was preserved.

Key words: natural zeolite, clinoptilolite, magnetic nanoparticles, graphene oxide, ciprofloxacin, adsorbent regeneration, non-thermal plasma.

Scientific filed: Technological Engineering
Scientific subfield: Environmental Engineering

Površinska modifikacija i funkcionalizacija prirodnoga zeolita – klinoptilolita

SAŽETAK

Cilj ove doktorske disertacije bio je razvoj novog, ekološki prihvatljivog i ekonomski isplativog adsorbensa na bazi prirodnog zeolita – klinoptilolita (CLI) za uklanjanje antibiotika ciprofloksacina (CIP) iz vodenih rastvora. Za modifikaciju je izabran CLI kao jedan od najdostupnijih prirodnih zeolita, dok je CIP izabran kao široko upotrebljivan antibiotik iz grupe fluorohinolona.

U radu, CLI je modifikovan na tri načina. Prvo, nanočesticama gvožđe-oksida (MAG) primenom dve metode: 1) ko-precipitacijom (MAG_{CP}-CLI) iz rastvora Fe(II)-soli i 2) mikrotalasnom kristalizacijom takođe iz Fe(II)-rastvora (MAG_{MW}-CLI). Treći postupak modifikacije podrazumevao je nanošenje grafen-oksida na MAG_{MW}-CLI pomoću ultrazvučnog tretmana (GO-MAG_{MW}-CLI).

Adsorpcija CIP-a na dobijene adsorbense ispitana je za različite početne koncentracije, temperature, vrednosti pH i reakciona vremena. Za anlizu uticaja ovih parametara na efikasnost adsorpcije korišćena je metoda za dizajn eksperimenta (DoE). Metodom odzivnih površina i primenom centralnog kompozitnog dizajna (RSM-CCF) određeno je sledeće: najveća moguća koncentracija CIP-a od 12.40 mg g^{-1} postignuta je na GO-MAG_{MW}-CLI za početnu koncentraciju 48,47 mg dm^{-3} pri pH = 5 i 24,78 °C, nakon 19,20 minuta.

Kinetika i mehanizam adsorpcije ispitivane su pomoću najčešće korišćenih kinetičkih modela i adsorpcionih izotermi na 10, 15 i 20 °C i pH = 5. Za sve ispitivane temperature, kinetika adsorpcije sledi Lagergrenovu jednačinu pseudo-drugog reda, dok se mehanizam procesa adsorpcije najbolje opisuje Langmuirovom izotermom. Zaključeno je da mehanizam adsorpcije CIP-a za ispitivane adsorbense uključuje dva procesa: reakciju jonske zamene i elektrostatičko privlačenje između negativno naelektrisane aluminosilikatne rešetke adsorbensa i CIP-katjona.

Modifikacija CLI-a mešovitim oksidima gvožđa (12 mas.%) doprinela je da adsorbensi dobiju magnetna svojstva i da se pomoću spoljašnjeg magnetnog polja lako mogu odvojiti od tečne faze. Takođe, prisustvo grafen-oksida na površini doprinelo je povećanju specifične površine i adsorpcionog kapaciteta.

Za regeneraciju adsorbenasa primenjena je nova metoda netermalne plazme (NTP) koja je prvi put ispitana u ovom radu za uklanjanje organskih vrsta sa površine minerala. U NTP tretmanu došlo je do stvaranja različitih reaktivnih gasnih vrsta koje su doprinele mineralizaciji adsorbovanog CIP-a. Rezultati su pokazali da u pet uzastopnih ciklusa adsorpcije/regeneracije, ostaje očuvano više od 90% adsorpcionog kapaciteta.

Ključne reči: prirodni zeolit, klinoptilolit, magnetne nanočestice, grafen-oksid, ciprofloksacin, regeneracija adsorbensa, netermalna plazma.

Naučna oblast: Tehnološko inženjerstvo
Uža naučna oblast: Inženjerstvo zaštite životne sredine

PROŠIRENI SAŽETAK NA HRVATSKOM

Klimatske promjene i konstantni porast broja svjetske populacije, utječu na količinu i kvalitetu izvora slatke vode. Rastuća potražnja za čistom vodom dovela je do istraživanja i razvoja novih tehnologija obrade vode koje bi mogle učinkovito ukloniti antibiotike kao organska mikroonečišćivala (engl. *organic micropollutants*, OMPs). Iako je koncentracija tih onečišćujućih tvari u okolišu još uvijek niska, one su vrlo postojane u okolišu te imaju tendenciju ka bioakumulaciji, što ozbiljno ugrožava zdravlje okoliša, ali neizravno i zdravlje ljudi. Učinci OMP-ova na žive organizme su raznoliki i nepredvidivi. Dodatni problem OMP-a u vodi je taj što se ne mogu učinkovito ukloniti konvencionalnim procesima obrade vode zbog prisutnosti u niskim koncentracijama i spore biološke razgradnje.

Prisutnost antibiotika (jedne grupe OMP-a) u prirodnim vodama potiče razvoj bakterija otpornih na antibiotike. Taj je fenomen zabilježen ubrzo nakon uvođenja prvog učinkovitog antimikrobnog sredstva te ga je Svjetska zdravstvena organizacija (engl. *World Helath Organization*, WHO) 2019. godine proglasila jednim od najvećih prijetnji globalnom zdravlju, sigurnosti hrane i razvoju današnjice. Poboljšanje učinkovitosti metaboliziranja postojećih antibiotika, brži izlazak novih antibiotika na tržište te razvoj novih tehnologija sposobnih za uklanjanje antibiotika iz vodenih sustava mogli bi biti glavni načini borbe protiv antimikrobne rezistencije. Ciprofloksacin (CIP) jedan je od najčešće korištenih antibiotika te je često detektiran u prirodnim vodama diljem svijeta. S obzirom na to da je molekula CIP-a zwitterion s dvije p*K*a vrijednosti (5,9 i 8,9 za aminsku, odnosno karboksilnu grupu), njezin naboj značajno ovisi o pH vrijednosti otopine u kojoj se nalazi što utječe na njegovo uklanjanje iz vode.

Adsorpcija predstavlja potencijalno rješenje za uklanjanje OMP-ova iz vode, s obzirom na to da se pokazala učinkovita u uklanjanju biološki nerazgradivih tvari prisutnih u niskim koncentracijama. Već se široko koristi u uklanjanju različitih onečišćivala iz (otpadne) vode, a jednostavnost samoga procesa, relativno jednostavna implementacija u postojeće sustave obrade, ne stvaranje nusprodukata i otpada te široki raspon dostupnih materijala za adsorbense neke su od glavnih prednosti adsorpcije u usporedbi s drugim istraživanim procesima. Među različitim adsorbensima, prirodni zeoliti ističu se svojom rasprostranjenošću u prirodi i jedinstvenim strukturnim svojstvima. Klinoptilolit (CLI) je znanstveno najistraživaniji prirodni zeolit, upravo zbog svoje dostupnosti, ekonomičnosti te širokog raspona mogućih primjena.

Iako prirodni CLI pokazuje izvrsnu adsorpcijsku učinkovitost u uklanjanju anorganskih onečišćivala, poput kationa teških metala i amonijaka te određenih organskih tvari iz vodenih medija, današnja istraživanja sve su više usmjerena ka njegovoj modifikaciji s ciljem poboljšanja adsorpcijskih svojstava. Najčešće primjenjivane metode modifikacije CLI-a uključuju konvencionalne fizikalne i kemijske metode. Fizikalno tretiranje podrazumijeva zagrijavanje CLI-a (mogući različiti izvori zračenja) što rezultira čišćenjem strukture CLI-a od nečistoća te poboljšanjem ionsko izmjenjivačkih svojstava, dok se kemijske metode temelje na tretiranju CLI-a kiselinom ili bazom čime se potencijalno povećava poroznost zeolitske strukture i izmjenjuju interstrukturni kationi s onima iz otopine. Modifikacije CLI-a mogu dovesti do povećanja specifične površine i volumena pora ili promjena u raspodjeli veličina pora te do promjene naboja površine. Tako, npr. precipitacija magnetskih nanočestica željezovog oksida na površini CLI-a može povećati aktivnu površinu CLI-a te ga učiniti magnetičnim. Magnetska svojstva

adsorbensa mogu doprinijeti njegovoj lakšoj separaciji iz vodene faze nakon adsorpcije uz pomoći vanjskog magnetskog polja. Nadalje, specifičnu površinu CLI-a moguće je povećati nanošenjem sloja materijala na bazi ugljika, kao što je grafen ili grafen oksid, ili biopolimera poput hitozana i sl.

U ovoj doktorskoj disertaciji, istraživan je potencijal prirodnog CLI-a i modificiranog CLI-a za uklanjanje antibiotika CIP-a iz vodenih sustava procesom adsorpcije. Prvi korak istraživanja uključivao je modifikaciju CLI-a nanočesticama željezovog oksida (MAG) i nanolistovima grafen oksida (GO). Modifikacija CLI-a nanočesticama MAG-a provedena je standardnom metodom koprecipitacije (MAG_{CP}-CLI) te metodom potpomognutom mikrovalnim zračenjem (MAG_{MW}-CLI). Novi i inovativni pristup primjene mikrovalova u sintezi nanočestica na CLI-u značajno je reducirao vrijeme sinteze (s 1 h na 5 min) i potrošnju energije. Usporedba ove dvije metode napravljena je na temelju oksidnih faza željeza formiranih na CLI-u, u svrhu čega je korištena Mössbauerova spektroskopija. Nadalje, uzorak MAG_{MW}-CLI je ultrazvučno tretiran u vodenoj disperziji GO kako bi se MAG_{MW}-CLI obložio nanolistovima GO (GO-MAG_{MW}-CLI).

Nakon sinteze adsorbensa uslijedila je detaljna karakterizacija istih. Strukturnom analizom CLI-a i pripravljenih adsorbensa utvrđeno je da modifikacijom nije došlo do značajnih promjena u kristaliničnosti CLI-a te da je njegova struktura ostala sačuvana nakon modifikacija. PXRD analiza potvrdila je očuvanost kristaliničnosti CLI-a nakon modifikacija. Difraktogrami CLI-a modificiranog s MAG ukazuju na koprecipitaciju jedne od faza željezovog oksida – magnetita (Fe_3O_4) ili maghemita (α-Fe_2O_3). Budući da te dvije faze željezovog oksida imaju identičnu spinalnu kristalnu strukturu i gotovo iste parametre kristalne rešetke, kvantitativnom (RIR) analizom dobivenih difraktograma utvrđeno je da je u MAG_{MW}-CLI uzorku prisutno više faza željezovog oksida, u kojem je dominantna faza α-Fe_2O_3 s Fe_3O_4 i getitom (FeO(OH)) kao sporednim fazama. Međutim, analizom površinske morfologije koristeći TEM analizu pokazano je da MAG_{CP}-CLI uzorak sadrži jedino Fe_3O_4 nanočestice (5–30 nm) ravnomjerno dispergirane po površini CLI-a. Također, TEM analizom je u uzorku MAG_{MW}-CLI potvrđeno prisustvo štapićastih kristala željezovog oksida – FeO(OH), prethodno detektiranog RIR metodom. Prema prosječnom kemijskom sastavu pripremljenih adsorbenata dobivenom EDS analizom, utvrđena je djelomična dealuminacija CLI-a prilikom modifikacije s MAG konvencionalnom metodom koprecipitacije. Također, udio MAG u MAG_{CP}-CLI i MAG_{MW}-CLI određen EDS-om iznosio je 12 mas.%, dok se izmjeren udio ugljika od 9.94 mas.% u GO-MAG_{MW}-CLI uzorku može pripisati nanesenom sloju GO-a. Kako bi se pobliže analizirale faze željezovog oksida dobivene novom metodom sinteze potpomognute mikrovalnim zračenjem, primijenjena je Mössbauerova spektroskopija. Njome je potvrđeno da je faza željezovog oksida formirana na CLI-u α-Fe_2O_3. Nastanak α-Fe_2O_3 obično je rezultat spore oksidacije prethodno nastalog Fe_3O_4. MAG_{MW}-CLI i GO-MAG_{MW}-CLI uzorci su također podvrgnuti XPS analizi kako bi se bolje utvrdila njihova površinska svojstva. Dobiveni XPS spektri visoke rezolucije za Fe 2p i C 1s regije ukazuju da je željezo prisutno u Fe^{3+} oksidacijskom stanju te da su u GO-MAG_{MW}-CLI uzorku prisutni oksidirani listovi grafena. BET metodom utvrđeno je da se poroznost CLI-a lagano mijenja s modifikacijama uz povećanje specifične površine (S_{BET}) tri puta uslijed sinergijskog učinka nanočestica MAG-a i GO-a. Interakcija nanočestica željezovog oksida i GO s CLI-om ispitana je FTIR analizom, dok je prisutnost GO u pripravljenom kompozitu GO-a i CLI-a (GO-CLI) potvrđena Ramanovom spektroskopijom. Mjerenjem zeta potencijala površina uzoraka CLI i modificiranog CLI-a pokazalo je da modificirani,

kao i čist CLI uzorci imaju negativno nabijenu površinu u širokom rasponu ispitivanih pH vrijednosti (2–12). Nadalje, određivanjem magnetskih svojstava, pokazano je da modifikacija CLI-a s magnetskim česticama CLI-u daje magnetska svojstva. Ovo svojstvo omogućilo je jednostavno uklanjanje adsorbensa iz vodene otopine nakon adsorpcije.

U sljedećem koraku uslijedili su eksperimenti adsorpcije šaržnom metodom. Eksperimenti adsorpcije provedeni su s antibiotikom ciprofloksacinom kao modelnim onečišćivalom. Metodom odzivnih površina uz centralno kompozitni dizajn određeni su optimalni uvjeti procesa adsorpcije koristeći Design Expert softver. Za dobivanje modela procesa, urađeno je 90 eksperimenata u kojima je ispitan utjecaj sljedećih parametara na adsorpcijski kapacitet za CIP: početne koncentracije CIP-a, pH, temperature, vremena kontakta te vrste adsorbensa. Varijable s najznačajnijim utjecajem na adsorpciju CIP-a su početna koncentracija CIP-a, pH i tip adsorbensa. Kao što je i očekivano, najveći adsorpcijski kapacitet za CIP pri svim ispitivanim početnim koncentracijama CIP-a, temperaturama i pH vrijednostima pokazao je GO-MAG_{MW}-CLI što se može pripisati značajnim povećanjem broja površinskih mjesta CLI-a dostupnih za adsorpciju CIP-a nakon modifikacije s GO-om koji je i zasebno pokazao odličan adsorpcijski kapacitet za CIP.

Kinetika adsorpcije ispitana na 10, 15 i 20 °C za različite početne koncentracije CIP-a (15–50 mg dm^{-3}) pokazala je da adsorpcijski kapacitet raste s vremenom za sve ispitivane adsorbense. Unutar prvih 10 minuta postiže se više od 85% ravnotežnog adsorpcijskog kapaciteta, što ukazuje na brzu kinetiku adsorpcije. Nadalje, Lagergrenov kinetički model pseudo-drugog reda najbolje opisuje kinetiku adsorpcije CIP-a na adsorbensima na bazi CLI-a, dok prema rezultatima primjene Weber-Morrisovog modela difuzije, difuzija između čestica nije limitirajući korak u adsorpciji CIP-a.

Dobiveni ravnotežni podaci adsorpcije analizirani su s dva empirijska modela adsorpcijskih izotermi – Langmuirovom i Freundlichovom izotermom. Općenito, Langmuirov model malo bolje opisuje adsorpciju CIP-a na svim ispitivanim adsorbensima. Taj rezultat ukazuje na to da adsorpcijski mehanizam uključuje nastajanje monosloja CIP-a na energetski homogenoj površini CLI-a, bez interakcija između susjednih adsorbiranih molekula CIP-a. Prema maksimalnim adsorpcijskim kapacitetima dobivenim iz Langmuirovog modela, najviša dobivena vrijednost je 47.91 mg CIP g^{-1} na 15 °C za GO-MAG_{MW}-CLI.

Adsorbensi zasićeni CIP-om korišteni su u ispitivanju otpuštanja adsorbiranog CIP-a te ispitivanju antibakterijske aktivnosti tako utrošenih adsorbensa. Dobiveni rezultati pokazali su da MAG sloj sprječava otpuštanje vezanog CIP-a te da je adsorpcija CIP-a na adsorbense na bazi CLI-a ireverzibilan proces. Test antibakterijske aktivnosti pokazao je značajnu aktivnost CIP-om zasićenih adsorbensa prema patogenim mikroorganizmima (*E. coli* i *S. aureus*), što otvara mogućnost korištenja ovako utrošenih adsorbensa u dezinfekciji vode.

Kako bi se pripremljeni adsorbensi na bazi CLI-a mogli smatrati u potpunosti učinkovitima, potrebno je ispitati i mogućnost njihove regeneracije. Korištenje adsorbensa u više ciklusa adsorpcije doprinosi njegovoj ekonomskoj isplativosti što je od velike važnosti prilikom razmatranja korištenja adsorbensa u većem, industrijskom mjerilu. U ovoj disertaciji, regeneracija sintetiziranih adsorbensa na bazi CLI-a istražena

je primjenom niskotemperaturne ili netermičke plazme. U eksperimentima je korišten plazma izvor s dielektričnim barijernim pražnjenjem (engl. *dielectric barrier discharge*, DBD) u zraku. Naime, različite reaktivne vrste generirane u plazmi (od elektrona do nabijenih i neutralnih atoma i molekula te fotona) mogu razgraditi adsorbirane molekule CIP-a na površini adsorbensa i time povratiti adsorpcijski kapacitet. Ovakvim „čišćenjem“ površne adsorbensa ne dolazi do stvaranja sekundarnog otpada niti je potrebno koristiti dodatne kemijske tvari. Ove karakteristike čine plazma tretman ekološki i ekonomski isplativom tehnologijom za regeneraciju materijala adsorbensa.

Rezultati regeneracije CIP-om zasićenih adsorbensa (čist CLI, GO-CLI i GO-MAG_{MW}-CLI) pokazali su vrlo dobru regenerabilnost adsorbensa nakon plazma tretmana. Svi ispitani adsorbensi imaju relativno stabilan adsorpcijski kapacitet za CIP kroz pet ispitanih ciklusa adsorpcije/plazma regeneracije. Također, ispitan je utjecaj plazma tretman na strukturu CLI-a analizom regeneriranog CLI-a PXRD-om i XPS-om uz ispitivanja njegove teksture BET metodom. Analize su pokazale da plazma ne utječe na strukturu i svojstva CLI-a, što je čini prihvatljivom metodom za regeneraciju mineralnih adsorbensa.

Ključne riječi: prirodni zeolit, klinoptilolit, magnetske nanočestice, grafen oksid, adsorpcija, ciprofloksacin, regeneracija adsorbensa, netermička plazma.

TABLE OF CONTENTS

LIST OF FIGURES

LIST OF TABLES

ABBREVIATIONS

AAS	Atomic adsorption spectroscopy
ANOVA	Analysis of variance
AOPs	Advanced oxidation processes
CCF	Central composite factorial design
CEC	Cation exchange capacity
CECs	Contaminants of emerging concern
CIP	Ciprofloxacin
CLI	Clinoptilolite
CLI-CIP	Ciprofloxacin-containing clinoptilolite
CLI-CIP_PL1	Clinoptilolite after 1st regeneration cycle
CLI-CIP_PL5	Clinoptilolite after 5th regeneration cycle
DBD	Dielectric barrier discharge
DoE	Design of experiment
EDA	Electron-donor/acceptor
EDS	Energy dispersive X-ray spectroscopy
FE-SEM	Field emission scanning electrone microscopy
FTIR	Fourier transform infrared spectroscopy
GO	Graphene oxide
GO-CIP	Ciprofloxacin-containing graphene oxide
GO-CLI	Graphene oxide-coated clinoptilolite
GO-CLI-CIP	Ciprofloxacin-containing graphene oxide-coated clinoptilolite
GO-MAG$_{MW}$-CLI	Graphene oxide-coated magnetic clinoptilolite
GO-MAG$_{MW}$-CLI-CIP	Ciprofloxacin-containing graphene oxide-coated magnetic clinoptilolite
LAE	Loss of adsorption efficieny
MAG	Magnetic nanoparticles
MAG$_{CP}$	Magnetic nanoparticles obtained by standard method
MAG$_{CP}$-CLI	Magnetic clinoptilolite obtained by standard method
MAG$_{CP}$-CLI-CIP	Ciprofloxacin-containing magnetic clinoptilolite
MAG$_{MW}$	Magnetic nanoparticles obtained by microwave-assisted method
MAG$_{MW}$-CLI	Magnetic clinoptilolite obtained by microwave-assisted method

MW	Microwave
NP	Nanoparticles
NTP	Non-thermal plasma
NZ	Natural zeolite
OES	Optical emission spectroscopy
OMPs	Organic micropollutants
PBU	Primarily building unit
PXRD	Powder X-ray diffraction
RIR	Reference intensity ratio
RNS	Reactive nitrogen species
ROS	Reactive oxygen species
RSM	Response surface methodology
SAED	Selected area electron diffraction
SBU	Secondary building unit
SDBD	Surface dielectric barrier discharge
TEM	Transmission electrone microscopy
TG/DTG	Thermal analysis
US	Ultrasound
WWTP	Wastewater treatment plant
XPS	X-ray photoelectrone spectroscopy

1. INTRODUCTION

Moderate and rational use of natural resources in accordance with the principles of sustainable development is one of the main global challenges in the field of environmental protection today. The constant growth of the world's population leads to higher living-standard demands, which among others, implies access to fresh and potable water. The limited availability of freshwater sources (which is less than 2% of the total planet's water), along with its uneven distribution, highlights the significance of smart water management and maintenance of water quality.

In light of the aforementioned, water pollution is considered a rising global crisis these days. From large pieces of waste to invisible chemicals, a wide range of contaminants end up in natural water bodies. The presence of contaminants of emerging concern (CECs) has been identified throughout the hydrological cycles, including surface and groundwater, and even in the food chain, which represents a risk to the environment and human health. Besides, as water scarcity continues to be a pressing issue and concerns over emerging contaminants grow, it is crucial to develop innovative and sustainable water treatment technologies. These technologies must be able to effectively remove the anthropogenic substances, preventing their accumulation and persistence in the environment, enabling contaminated water reuse in industries, agriculture, and human consumption. The inefficiency of conventional water treatment in the removal of these contaminants makes the development of new and advanced technologies even more crucial.

In the last decades, antibiotics are one of the most widely detected emerging contaminants in water bodies. Among various adverse effects that they have on environmental organisms, the development of antibiotic resistant bacteria is considered one of the most significant consequences of the antibiotics' presence in the environment. The annual consumption of antibiotics worldwide is already a dizzyingly high number and is estimated to continue to grow. Some types of antibiotics, such as amoxicillin and ciprofloxacin, have been a part of the European Union's Watch List monitoring since they were demonstrated to be toxic to aquatic organisms and/or humans.

Besides the simplicity of operation and relatively easy implementation into existing treatments, the adsorption process has shown great potential in removing organic micropollutants (OMPs) from water due to the wide range of available adsorbent materials and the ability to tailor removal mechanisms based on different adsorbent-OMP interactions. Separation and regeneration of adsorbent appear to be the main disadvantages of adsorption. The development of adsorbents with magnetic properties overcomes the separation issue. The use of an external magnetic field enables easy separation of the magnetic adsorbent from the liquid phase. In addition, proper separation of the adsorbent is inevitable for its regeneration and use of adsorbent in multiple adsorption cycles. The reusability of the adsorbent significantly increases the process's economic feasibility and is one of the main advantages of the adsorption process. The most commonly used conventional regeneration methods, including chemical and thermal treatments, have shown promising results in the regeneration of some types of adsorbents, such as activated carbon and minerals. However, these methods come with certain disadvantages in terms of high energy requirements and involvement of non-environmentally friendly chemicals. Additionally, both methods are time-consuming and

require more than one step, which decreases efficiency and increases operational costs. Moreover, they can lead to partial or even complete destruction of the adsorbent's structure.

Abundant and environmentally friendly natural zeolites have been recognized as a perspective material for adsorption. Due to their unique structural properties, they show selectivity in the adsorption. Also, zeolite's performance can be improved by different modifications without affecting its structure.

The main goals of this doctoral thesis were:

- Development of novel, efficient, environmentally friendly, and cost-effective adsorbents based on natural zeolite – clinoptilolite. To achieve this goal, the natural clinoptilolite was modified with iron oxide nanoparticles and graphene oxide nanosheets. The modification was carried out by a standard co-precipitation method and a novel microwave-assisted method.

- Study of the removal process of the antibiotic ciprofloxacin from aqueous solutions by prepared adsorbents. The adsorption capacity of the adsorbents, as well as the influence of specific parameters on ciprofloxacin adsorption, were investigated by a batch method. The optimal parameters in the adsorption were determined by the response surface methodology approach. Adsorption kinetics and mechanism were investigated using different kinetic and adsorption models.

- Study of the reusability of the prepared adsorbents. For this task, a novel method including the plasma technique was tested. Satisfactory results were achieved by using non-thermal atmospheric pressure plasma treatment.

The hypotheses of the research included:

- The efficiency of clinoptilolite in the adsorption process of different pollutants. Possibility of clinoptilolite modification by: (i) magnetic nanoparticles which facilitate the separation of the spent adsorbent, (ii) graphene oxide which significantly increases the adsorption capacity towards pollutants.

- The efficiency of plasma in degradation of ciprofloxacin species present in water media. Since the reactive species formed in the plasma destroy organic species in a liquid phase, it was assumed that they would be also effective in destroying the adsorbed species on the solid adsorbent.

2. THEORETICAL PART

2.1. Water pollution by organic micropollutants (OMPs)

Many regions of the world continue to face the challenge of accessing clean and safe drinking water. The state of global water distribution (Figure 1) shows that less than 1% of fresh water is available, which makes this challenge difficult to solve. The key question is whether this amount of fresh water is sufficient to meet the basic water needs of eight billion people. The fact is that around 30% of the global population lacks access to safe fresh water, while the water needs of the remaining population are constantly increasing. Recently, it has been reported that some regions (India, China, some European countries, and Africa) have already experienced a "*water crunch*" (Bijekar *et al.*, 2022).

The world's growing population together with rising living standards, and technological advancements have led to the everyday application of many novel chemicals. According to the Eurostat report[1], in 2021, the European Union only produced a total of 279 million tonnes of hazardous and non-hazardous industrial chemicals and consumed 299 million tonnes, which is 4% more than in 2020. These chemicals certainly improved the quality of everyday life and provided life-saving medical treatments, but the unintended result is that they also become contaminants entering the environment (Deere *et al.*, 2020). Over the past few decades, the production and consumption of different types of novel chemicals have significantly increased, drawing global attention to the issue of water pollution caused by contaminants of emerging concern (CECs) (Chávez-Mejía *et al.*, 2019). One of the main problems of CECs is their persistence in the environment due to their low biodegradability and tendency to bioaccumulate (Chávez-Mejía *et al.*, 2019; Wilkinson *et al.*, 2017). Their complex chemistry makes them present in the air, soil, water body, river, and ocean sediment, as well as in the tissues of aqueous organisms (Enyoh *et al.*, 2020; Frade *et al.*, 2014; Luo *et al.*, 2014; Maddela *et al.*, 2022; Rzodkiewicz *et al.*, 2022).

[1]Eurostat: Production and consumption of chemicals up in 2021; env_chmhaz.

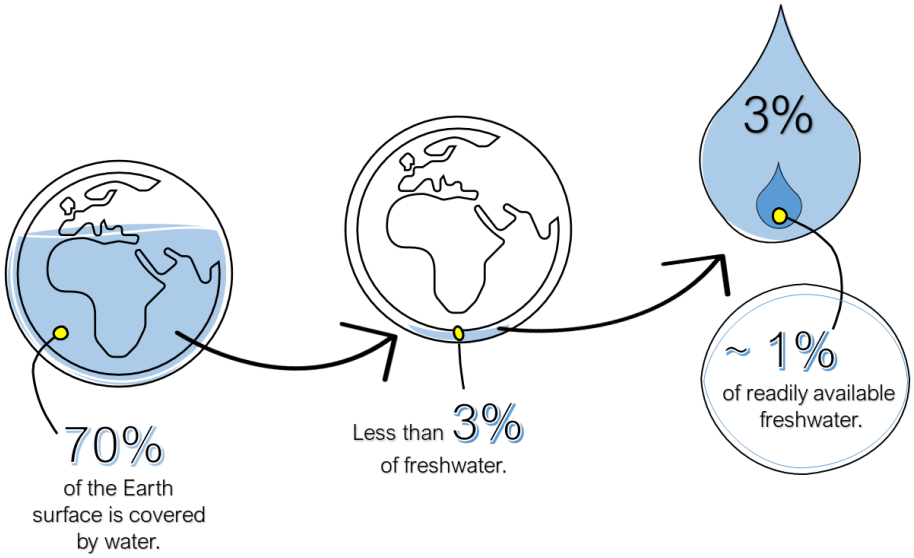

Figure 1. Global water distribution.

The CECs include various chemicals such as pesticides, pharmaceuticals, personal care products, microplastics, steroid hormones, surfactants, industrial chemicals, flame-retardants, etc. (Kasonga *et al*., 2021; Luo *et al*., 2014; Patel *et al*., 2019; Wilkinson *et al*., 2017). Many of them are also classified as organic micropollutants (OMPs). As the term itself implies, OMPs refer to organic carbon-based compounds present in the environment at the micrograms or nanograms per litre, regardless of their chemical structure, usage, or mode of action (Kümmerer, 2011; Luo *et al*., 2014).

The occurrence of OMPs in the aquatic environment, even at trace concentrations, has been frequently associated with a range of adverse effects, such as short- and long-term toxicity, behavioural changes, endocrine disrupting effects, reduced fertility, and the development of antibiotic resistance microorganisms (Kasonga *et al*., 2021). More precisely, these substances can cause metabolic dysfunction and affect the behaviour of fish populations (Meador *et al*., 2018), be highly toxic to green algae (with direct toxicity at a few µg dm^{-3}) (Shao *et al*., 2019), and interfere with the hormonal system of freshwater mussels, reducing their reproductive ability (Rzodkiewicz *et al*., 2022). Long-term exposure to multiple OMPs in water poses an even greater concern as it increases the complexity of the potential hazards to human health. Although knowledge about the adverse effect of water OMPs on humans is scarce, endocrine disruption, reproductive problems, and increased risk of cancer have been reported as health consequences. OMPs have also been associated with some neurological and immune system effects (Xue *et al*., 2021). An additional concern is the presence of a complex mixture of OMPs in the water environment (known as the *cocktail effect*), which could lead to undesirable synergetic effects, making the assessment of the effluent's toxicity unpredictable (Petrie *et al*., 2015).

Since water became an inevitable resource for every human activity, the OMPs can easily enter the water environment through diverse pathways. The major OMPs sources in the environment include industrial and household wastewater, hospital effluents, and runoff from agricultural fields and livestock (Golovko *et al*., 2020).

To detect and control the OMPs in water bodies and to increase public awareness of their potential adverse health and environmental effects, European Union established the Water Framework Directive 2000/60/EC (WFD) in 2000. As fundamental legislation for water quality control, WFD provides the basis for the assessment of the chemical and ecological status of surface and ground waters. According to European Environmental Agency (EEA, 2018), a total of 38% of surface water bodies in the EU were in good chemical status, 46% were not, while for 16% the status was "unknown". The goal of WFD is to achieve good chemical and ecological status of all water within the EU by 2027. The concentration of substances in the water is compared with their environmental quality standards (EQSs) specified by the WDF amendment 2008/105/EC (Directive 2008/105/EC). Contaminants that most frequently exceed their EQSs in surface waters are mercury and polycyclic aromatic hydrocarbons from atmospheric depositions; surfactants and flame retardants from urban settlements; heavy metals and different insecticides and herbicides from agriculture (Whalley, 2018). As a part of the WFD, the EU's Watch List of Contaminants of Emerging Concern was established in 2015 as an additional tool for risk determination of CECs and whether EQSs should be set for them at the EU level. Generally, the monitoring period for one substance was determined to be three years, and if sufficient data is collected, a substance can be removed from the list. The first watch list, implemented by decision EU 2015/495, included ten substances belonging to different groups of contaminants: hormones, antibiotics, anti-inflammatories, pesticides, and food oxidants (EU 2015/495, 2015). The list is regularly updated, with the latest version in 2020 by the decision EU 2020/1161 (EU 2020/1161, 2020).

2.1.1. Water pollution by antibiotics

Ever since Flaming's discovery of the so-called "wonder drug" in 1929, antibiotics have been widely used as pharmaceutical agents for the treatment of different bacterial infections in both human and veterinary medicine. Additionally, their application has been extended to livestock production where they are intensively used as growth promoters and in prophylaxis[2] (Johnson *et al.*, 2015). Due to the wide range of their applications, the global production of antibiotics is constantly increasing. According to Klein *et al.*, global antibiotics consumption increased by 65% between 2000 and 2015, indicating that the presence of antibiotics in the environment is increasing and causing a variety of problems (Klein *et al.*, 2018). Many researchers have ranked antibiotics as pharmaceuticals of greatest concern for the aquatic environment (Johnson *et al.*, 2015; Patel *et al.*, 2019). Therefore, despite saving a million lives, the uncontrolled consumption of antibiotics is nowadays one of the major environmental issues.

Due to their structural complexity, antibiotic molecules are stable, exhibiting long-lived persistence in the environment and therefore posing a risk to the environment with already noticeable consequences for human health as well (Verlicchi *et al.*, 2012). Only a small portion of the consumed antibiotics is adsorbed by the human or animal body. Most of the active part (10%–90%) is discharged unmetabolized. The unchanged antibiotics together with their metabolites reach the water bodies through untreated sewage and wastewater streams from households, hospitals, pharmaceuticals industries, and animal husbandry (Frade *et al.*, 2014).

[2] Treatment given to prevent disease.

Elevated concentrations of antibiotics in the environment, in addition to their toxic effect on non-target aquatic organisms even in low concentrations, lead to the appearance of antibiotic-resistant bacteria (Frade *et al*., 2014; Johnson *et al*., 2015; Kraemer *et al*., 2019). Bacterial resistance refers to a bacterium's ability to withstand or tolerate the effects of antibiotics. The inefficiency of antibiotics to treat the infection for which they were specifically designed, makes the treatment of some infections (such as pneumonia, tuberculosis, or blood poisoning) less effective or even impossible. Resistance mechanisms are evolving and spreading globally very fast, reducing the treatment ability of common infectious diseases. The fact that currently, more than 95% of *Staphylococcus aureus* isolates worldwide are penicillinase-resistant reflects the severity of the situation (Chinemerem Nwobodo *et al*., 2022). In 2014, the World Health Organization (WHO) recognized this phenomenon as one of the top ten global public health challenges, with antibiotic-resistant diseases predicted to claim up to 10 million lives per year by 2050 (Antimicrobial Resistance, WHO, 2020). In addition to increased mortality, antibiotic resistance also leads to higher medical costs and prolonged hospital stays. Aside from the development of antibiotic resistance, some other effects of antibiotics on aquatic organisms were also reported. According to their toxicity, antibiotics could be classified as extremely toxic to microorganisms with EC_{50}[3] below 0.1 mg dm^{-3}, and very toxic to algae with EC_{50} in the range 0.1–1 mg dm^{-3} (Jones *et al*., 2002). The inhibition of growth in certain algae at different antibiotic concentrations from even 6 µg dm^{-3} and effects on nitrification activity at 9 mg dm^{-3} was observed (Santos *et al*., 2010). Kümmerer reported adverse antibiotics effects on reproduction, hatching and viability of juvenile stage of crustaceans at concentrations less than 1 mg dm^{-3} (Kümmerer, 2011).

Despite the implementation of monitoring systems in some countries to curb the improper use of antibiotics, regulation of water pollution by antibiotics remains lax. Yet, no clear legal requirements have been set for discharging of these persistent and biologically active substances into surface water bodies (Verlicchi *et al*., 2012). Consequently, different types of antibiotics can be found in surface and ground waters as well as in drinking water (Kraemer *et al*., 2019).

2.2. A brief overview of wastewater treatments

The main goal of any wastewater treatment is to enable either the reuse of produced wastewater streams or their safe discharge into waterways. The Wastewater Treatment Plant (WWTP) is based on procedures that include physical, chemical, and biological processes for removal of suspended and/or dissolved pollutants.

A conventional WWTP includes four stages. First, *preliminary treatment* aimed at coarse screening (rocks, twigs and leaves, and other large objects) and grit removal. The second stage or *primary treatment* consists of settleable organic and inorganic solids removal by sedimentation, and removal of floating materials by skimming. Here, the coagulants are added to accelerate the sedimentation process. In the following *secondary treatment*, the aerobic microorganisms (bacteria and protozoa) metabolize the organic matter in the presence of oxygen. The system conditions, such as temperature, pH, oxygen level and water flux, are controlled to maintain the activity of microorganisms. Also, a presence of some substances, such as heavy metals can hamper the degradation due to the bacteria

[3] Half maxima effective concentration.

sensitivity to environmental conditions. The obtained biomass or secondary sludge is separated from the water and combined with the primary sludge for sludge processing. In the final stage (*tertiary* or *advanced treatment*), the water effluent from secondary treatment goes through a disinfection process by chlorination, ozonation, or UV light treatment.

The obtained solid sludge from primary and secondary treatments can be subjected to anaerobic digestion for drying and stabilization before its further reuse or discharged in a landfill. Since the activated sludge from conventional treatment may contain nutrients such as nitrogen and phosphorous, additional process stages can be applied for their extraction from the sludge and reuse.

Advanced processes in WWTP are employed when the required level of water quality cannot be achieved by secondary treatment. This stage should be used for removal of trace amounts of toxic substances such as heavy metals and/or OMPs. Additional treatment steps beyond WWTP may be necessary to ensure that the water meets all regulatory standards for drinking water or for reuse which includes irrigation, industrial processes, or domestic purposes. In the latter, the water does not necessarily need to be potable, but it must meet criteria for the particular application.

2.2.1. Antibiotics removal from wastewater

Research studies have shown that conventional WWTPs do not completely remove antibiotics (20–90%) (Watkinson *et al.*, 2007). Primary treatment is ineffective in antibiotics' removal, while the variety of processes in the secondary treatment are shown to be efficient in reduction of antibiotic concentration in WWTP (Jia *et al.*, 2012). Thus, a combination of adsorption on activated sludge and degradation by microorganisms showed good results in removal of antibiotic lincomycin (58–74%) and fluoroquinolone ciprofloxacin (about 80%) (Hazra & Durso, 2022; Huang *et al.*, 2021). However, this treatment is quite inactive for antibiotics that are resistant to biodegradation. The predominant processes currently used in removal of antibiotics from wastewater streams include the use of biological aerated filters, anaerobic digestion, sequencing batch reactor, and membrane bioreactor. Furthermore, the constructed wetlands treatment system, where water is purified by filtration, co-precipitation, ion exchange, plant adsorption and biodegradation, remove quinolone-type antibiotics from breeding wastewater in a range from 82 to 100% (Hazra & Durso, 2022; Huang et al., 2021). Liu *et al*. reported that a zeolite-medium vertical flow constructed wetland can reduce ciprofloxacin level for 85% (Liu *et al*., 2013). Additionally, hydrolysis has shown to be important for prediction of antibiotics' persistent in the environment. It is one of the main degradation pathways for antibiotics with amide and ester functional groups (Lin *et al*., 2007).

State-of-the-art treatment processes investigated for the antibiotic removal from effluents of different origins are summarized in Figure 2. The process of coagulation–flocculation (C–F) can be applied at different stages of water treatment, as a primary or tertiary treatment. The C–F proved to be efficient as a pre-treatment of hospital effluents, with 30–60% efficiency in removal of certain antibiotics (Suarez *et al*., 2009). The removal of ciprofloxacin from hospital effluents by adsorption onto powdered activated carbon (PAC) showed high efficiency (more than 98%) suggesting that PAC can be used for pre-treatment of hospital effluents. Although activated carbon proved to be suitable for removing different types of antibiotics, removal efficiency is affected by type of activated

carbon, initial antibiotic concentration, pH, temperature, content of dissolved organic carbon, etc. Thus, granular form of activated carbon (GAC) has twice lower efficacy for ciprofloxacin than PAC (Kovalova *et al*., 2013). Moreover, inorganic polymers such as zeolites are more effective for the fluoroquinolone antibiotics than organic biopolymer - cellulose (efficiency of 90% and 27%, respectively) (Suarez *et al*., 2009).

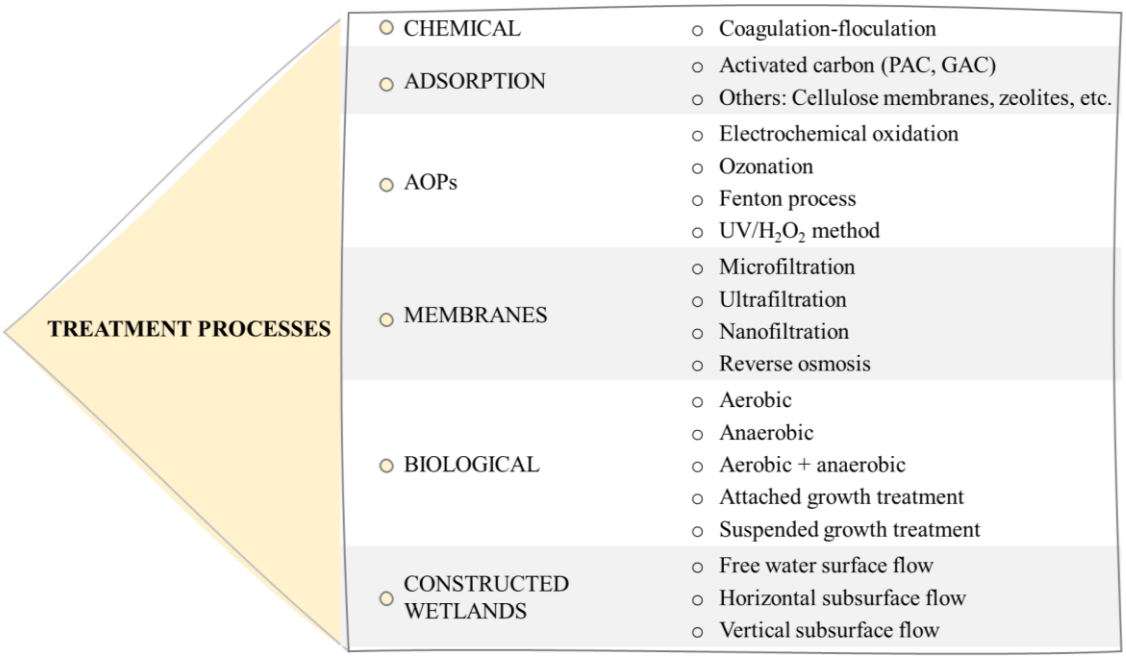

Figure 2. Single treatment processes for antibiotics removal (adapted from de Ilurdoz *et al*., 2022).

Among the studied advanced oxidation processes (AOPs), ozonation and UV/H_2O_2 processes proved to be the most effective ones for antibiotic removal by oxidation. Namely, the ozonation showed a high removal efficiency (>98%) for different types of antibiotics such as sulfamethoxazole or trimethoprim. The high removal efficiency of ozonation has been explained by two mechanisms: (i) by direct O_3 oxidation and (ii) by indirect oxidation carried out by free radicals (Gerrity *et al.*, 2011; B. S. Silva *et al.*, 2022). UV/H_2O_2 process showed a good efficiency in removal of antibiotics from domestic wastewater. Degradation efficacy is in the range from 52% to 100% depending on the type of antibiotic (Rosenfeldt *et al*., 2006).

The retention of molecules in the small pores of membranes during wastewater flow is used for removal of various types of antibiotics in membrane filtration process. This procedure has a high removal efficacy (~ 100%) and was tested both in pilot and in industrial plants for the treatment of different types of wastewaters (de Ilurdoz *et al*., 2022).

2.2.2. Target pollutant in this research

Antibiotics ciprofloxacin and amoxicillin are on the EU's Watch List of CECs from 2018. The inclusion of these two antibiotics was related to the European *One Health Action Plan against Antimicrobial Resistance* which has an important task to "improve knowledge of the occurrence and spread of antimicrobial in environment".

Ciprofloxacin

Ciprofloxacin (CIP, molecular formula $C_{17}H_{18}FN_3O_3$) is one of the most widely used fluoroquinolone antibiotics of the second generation worldwide. It has been extensively used in treatment of different bacterial infections (such as urinary and respiratory tract infections, skin and soft tissue infection, and gastrointestinal infections) due to its excellent activity against both Gram-positive and Gram-negative bacteria. Its extensive use results in the CIP presence in surface water in different ranges of concentrations that can be even 50 mg dm^{-3} near drag manufacturing plant (Rakshit *et al.*, 2013). An interesting but also more concerning fact is that until 2013, among 200 different pharmaceuticals that have been reported in rivers worldwide, CIP was one of antibiotics with the highest concentration of up to 6.5 mg dm^{-3} (Petrie *et al.*, 2015). The predicted PNEC[4] of CIP in fresh water is found to be 0.089 µg dm^{-3}.

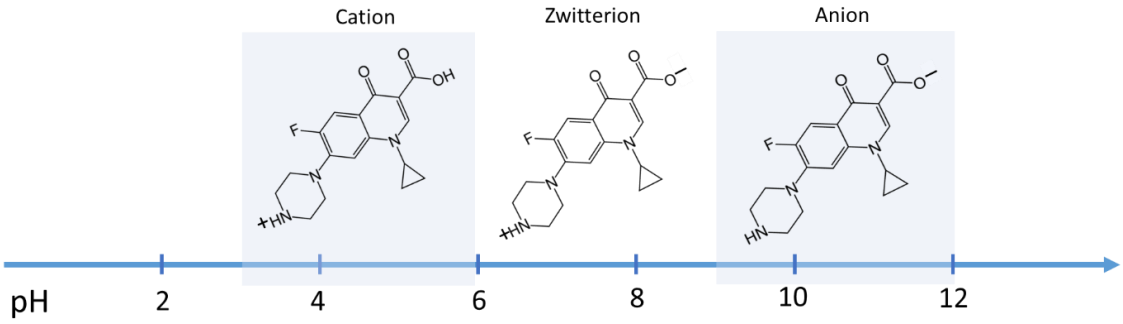

Figure 3. CIP molecular structure depending on pH: cationic form (3–6), zwitterionic form (6–9), and anionic form (9–12).

The structure of CIP molecule (Figure 3) has an extended aromatic region (quinolone moiety) and two ionizable groups – amine and carboxyl, with p*K*a = 5.90 ± 0.15 and 8.89 ± 0.11, respectively. Therefore, depending on the pH value, CIP molecule can exist as a cation, zwitterion, or anion. Accordingly, the adsorption efficiency and the CIP removal mechanism strongly depend on the pH value of the initial solution (Carabineiro *et al.*, 2012; Genç & Dogan, 2015). The presence of fluorine atom in the CIP structure makes the molecule highly stable, resulting in its low degradation rate in the environment. CIP is soluble in water, with the solubility at 25 °C of about 1.35 mg cm^{-3} (Al-Musawi *et al.*, 2021).

2.3. Natural zeolites: structural properties

Zeolites are hydrated aluminosilicates with crystal structure composed of $[SiO_4]^{4-}$ and $[AlO_4]^{5-}$ tetrahedra as primarily building units (PBUs). PBUs are connected in all three dimensions by oxygen atoms forming secondary building units (SBUs) or cages, which contribute to formation of a three-dimensional framework of channels and cavities (Figure 4). The channel system gives zeolites porosity and affects their chemical and physical properties. The apertures at channel systems are in the range from 0.3 and 3 nm allowing diffusion and adsorption of appropriate species (molecules, atoms, ions) (Sobuś *et al.*, 2020). Aluminosilicate lattice of zeolites are negatively charged. Electroneutrality of the structure is achieved by the presence of extra-framework exchangeable cations (i.e.

[4] Predicted No-Effect Concentration; NORMAN Ecotoxicology Database

alkali and earth alkaline cations) (Cakicioglu-Ozkan & Ulku, 2005). The cations are situated inside the channels and cavities together with water molecules. They interact with the lattice via electrostatic interactions, they are mobile and can be exchanged by other cations. Additionally, the removal of water molecules is reversible, which makes zeolites an efficient drying agent (van Reeuwijk, 1974).

Due to the porosity, zeolites have a relatively large specific surface area which results in excellent adsorption and molecular sieve properties. Moreover, the size and shape of the openings influence zeolites' adsorption behaviour and enable only molecules with diameter smaller than the openings to enter the lattice. Zeolites have different Si/Al molar ratio which affects interactions of zeolite surface and external species. For example, zeolites with a smaller Si/Al ratio more likely interact with polar molecules in contrast to those with higher Si/Al ratio which are favourable for non-polar molecules.

Finally, zeolites can be converted to solid acids and exhibit catalytic activity in various chemical reactions. The acidity of zeolites can be expressed as Brønsted or Lewis acidity. It can be significantly enhanced through chemical or thermal treatment. The Brønsted acidity is related to the presence of bridging Si–OH–Al bonds, while Lewis's acid sites originate from extra-framework aluminium species (Grifoni *et al.*, 2021; Trachta *et al.*, 2022).

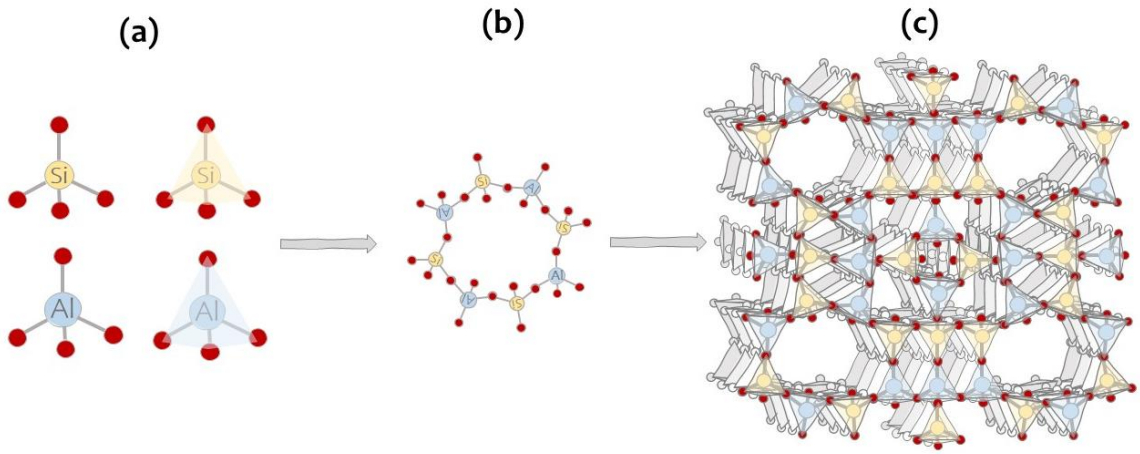

Figure 4. Basic structural units of zeolites: (a) primary building units; (b) secondary building unit – cage; and (c) 3D framework.

Natural zeolites are formed through hydrothermal transformation of aluminosilicates present in sedimentary environments. The most abundant natural zeolites include analcime, chabazite, clinoptilolite, mordenite and stilbite. Because of availability around the world as well as a low prise, clinoptilolite is the most studied natural zeolite.

The name of clinoptilolite (CLI) is derived from three Greek words: *klinos* meaning diagonal, *ptylon* meaning feather, and *lithos* meaning stone (Ghobarkar *et al.*, 2003). The crystal structure of CLI was determined as monoclinic with C1 2/m space group (International Zeolite Association – IZA, 2022).

The three-dimensional CLI framework consists of three different straight channel systems along x- and z-axes. They are marked as:

- A channels formed by tightly packed ten-membered rings (with aperture of 0.3 × 0.76 nm),
- B channels constituted by eight-membered rings (0.33 × 0.46 nm), and
- C channels formed by eight-membered rings (0.26 × 0.47 nm).

Channels A and B ran parallel to the z-axis (Figure 5a), while the C intersects the channels A and B, extending along the x-axis (Figure 5b). The types of exchangeable metal cations play a crucial role in adsorption capacity of CLI.

The chemical composition of CLI differs depending on the geographical area of deposits. CLI deposits occur in several countries worldwide, with the most significant ones in Bulgaria, Hungary, Turkey, Cuba, Mexico, Russia, Italy, Serbia, and United States (IZA, 2022; Cinar & Beler-Baykal, 2005).

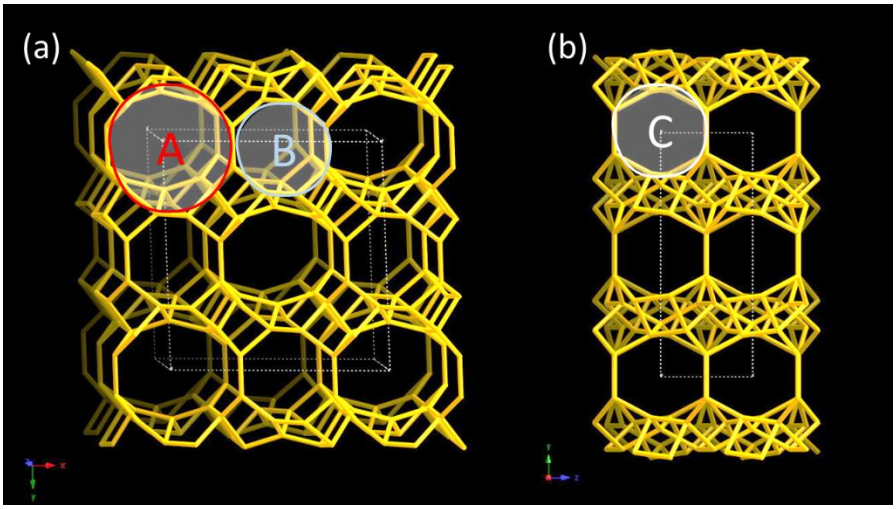

Figure 5. CLI framework: (a) viewed along [001], and (b) along [100] plane (IZA, 2022).

The clinoptilolite has gained significant attention in research not only because of its numerous potential applications but also due to its cost-effectiveness. At a cost of 100–600 dollars per ton, clinoptilolite is more affordable compared to synthetic zeolites (Dosa *et al*., 2022).

2.4. Application of clinoptilolite

CLI has been deemed a promising and eco-friendly natural reagent for the preparation of various materials with applications in ion-exchange, adsorption, catalysis, etc. Its effectiveness is closely influenced by zeolite's physical-chemical properties.

One of the most perspective areas of CLI application is in the *water treatment*. CLI has been widely studied in removal of different types of pollutants from water media. The pollutants are toxic heavy metals cations (Cu^{2+}, Zn^{2+}, Ni^{2+}, Cd^{2+}, Pb^{2+}, Fe^{3+}, etc.) (Cerjan Stefanović *et al*., 1996; Ćurković *et al*., 2014; Rajic *et al*., 2010; Stojakovic *et al*., 2012) and anions (NO_3^-, PO_4^{3-}, SeO_3^{2-}, SeO_4^{2-}, etc.) (Jevtić *et al*., 2014; Pavlović *et al.*, 2014), ammonia removal as well as various organic species such as chemical warfare agent simulants, pesticides, dyes, or pharmaceuticals (Muir *et al*., 2016; Rožić *et al.*, 2002; Tušek *et al*., 2017). CLI has shown a high degree of selectivity in removing ammonia from water media through adsorption and ion-exchange (Nan *et al*., 2019; Zabochnicka-

Świątek & Malińska, 2010). CLI has also been applied to stabilize ammonia levels in aquariums, ponds, drinking water, and other aqueous systems. NASA has been studied Ca-rich CLI for ammonia removal from advanced life support wastewater system to provide a long-term human presence in space (Armbruster, 2001). CLI is commonly used as a water softener capturing Ca^{2+} and Mg^{2+} ions. Moreover, CLI can promote the growth of nitrifying bacteria, prevent algae growth, stabilizes pH, and improve water clarity as well as reduce the odours. Since CLI is classified as GRAS[5] material for aqueous organisms and plants, it can be used in pools, hot tubs, and natural ponds to regulate the concentration of undesirable harmful substances. Moreover, CLI can adsorb 98% of the Methylene Blue (MB) dye (C_0 = 100 mg dm^{-3}) from synthetic aqueous solution in only 15 minutes (Dosa *et al*., 2022).

CLI unique pore structure allows its use in *gases separation* and *air purification*. Smaller molecules such as CO_2 and N_2 can diffuse in the CLI structure quickly, preventing the diffusion of slightly larger molecules such as CH_4. In addition, good thermal stability, and acid resistance of CLI enable its use in *fuel gas clean-up applications* (Ackley *et al*., 2003).

CLI and its modified forms have been studied in *medical and pharmacological applications*. It has been intensively studied as a drug-carrier for biomedicine and pharmaceutics since it is stable in the gastrointestinal tract and non-toxic. The possibility of encapsulation of ions and drug molecules in the aluminosilicate open framework followed by their controlled release is one of the most valuable pharmacological applications of natural CLI today. CLI had been tested as a carrier for different types of drugs. Thus, the magnetic CLI and surfactant-modified CLI showed a potential in the controlled delivery of hypericin and cephalexin, respectively (Hovhannisyan *et al*., 2021; Nezamzadeh-Ejhieh & Tavakoli-Ghinani, 2014). It also possesses biocatalytic potential and antioxidative activity, which enable its use in cancer treatment (Yaneva *et al*., 2021).

In *agriculture*, CLI has been used as a soil supplement or a component of fertilizers in order to improve the soil efficiency by retaining plant nutrients (such as nitrogen, potassium, calcium, etc.). It was reported that use of CLI reduces utilization of the fertilizer and prevent the groundwater pollution caused by nutrients leaching (Polat *et al*., 2004). The addition of CLI to the soil also contributes to *remediation of the soil* polluted by toxic metals (Nuić *et al*., 2022). Furthermore, CLI is used as dietary supplement in animal husbandry to improve the productive performance. The proposed mechanisms include ammonia binding which reduces toxic effects of ammonia produced by intestinal microbial activity, enables enhanced pancreatic enzymes activity, and improves energy and protein retention (Marc & Tulcan, 2019).

The conversion of waste biomass into high value-added products or green reaction pathway in production of widely applicable chemicals have gain much attention in the last decades due to these processes' feasibility and commercial perspectives. To use environmentally friendly catalyst and to achieve sustainable processes, the catalytic activity of CLI and its modified forms has been investigated for different organic reactions, such as isomerization, catalytic reduction, oxidation, or esterification. In these

[5] Gennerally Regarded as Safe

reactions, CLI shows a high activity as a catalyst and as a catalyst support (Miądlicki *et al*., 2021; Pavlović *et al.*, 2019).

2.4.1. Adsorption

Among different technologies that have been investigated and applied in water treatment, adsorption is found to be a promising and efficient technique for removal of different types of water contaminants (de Andrade *et al*., 2018; Mojiri *et al*., 2020; Xiao *et al*., 2021). Relatively simple design, ease of operation and low maintenance and operational costs as well as applicability of a wide range of adsorbents demonstrate the superiority of the adsorption in comparison with the other methods (Lin & Lee, 2020; Salem Attia *et al*., 2013).

Since the costs of adsorption-based treatments mainly depend on the cost of the adsorbent and the management of the spent adsorbent, a variety of low-cost adsorbents, such as carbon-based materials (El-Shafey *et al*., 2012; Zhang *et al*., 2017), and naturally occurring minerals (clay minerals and natural zeolites) (Ashiq *et al*., 2019; Cheng *et al*., 2018; Ngeno *et al*., 2019) have been explored. Accordingly, CLI has been intensively studied as an efficient adsorbent for the removal of different inorganic and organic pollutants, such as organic dyes (Dosa *et al*., 2022; Qiu *et al*., 2009), pesticides (Pavlinović *et al*., 2021) and pharmaceuticals (Ngeno *et al*., 2019).

Adsorption of antibiotics

In addition to chemical and biological degradation, adsorption plays a crucial role in controlling the fate of organic pollutants in the environment. It has also shown a promising efficiency in antibiotics removal (de Andrade *et al*., 2018). The suggested mechanism of antibiotic molecules adsorption onto zeolite-based adsorbents includes the following interactions:

- electrostatic,
- cation-exchange,
- electron-donor/acceptor (EDA),
- hydrogen bonds,
- complex formation.

Electrostatic interaction is greatly affected by pH and ionic strength of water media and is one of the most important interactions in adsorption of organic molecules onto CLI. It involves the interaction of ionizable organic species with negatively charged CLI surface. The pH value of the medium induces either the attraction or repulsion between the CLI surface and organics. The surface properties of CLI as well as ionization of organics strongly depend on the pH. Cation-exchange occurs when organics are present as cations with appropriate dimensions relative to the size of lattice pore openings. Furthermore, the EDA interactions usually occur between aromatic species and the CLI surface. The EDA interactions include π–π electron donor/acceptor interactions between the protonated rings and negative CLI surface (Igwegbe *et al*., 2021). Hydrogen bonding includes weak partial intermolecular bonds of special type of dipole-dipole moment. It exists between a carbon-oxygen functional groups of organic molecules and adsorbent surface involving hydrogen ions (El-Shafey *et al*., 2012; Igwegbe *et al*., 2021). Complex formation is characteristic for interactions between organic species and metal oxides. The surface complexation can be monodentate or bidentate where the functionalities of organic

molecules (such as carboxylic group) are coordinated to a metal centre through oxygen atoms, causing strong adsorption via inner-sphere complexation (Rakshit *et al.*, 2013).

Adsorption of ciprofloxacin (CIP)

Different types of adsorbent materials (from natural to synthetic ones) have been studied for the CIP adsorption from water media. The removal efficiency of CIP on different adsorbents, adsorption conditions and reusability of the adsorbents are listed in Table 1. Electrostatic interactions accompanied by cation-exchange have been reported as adsorption mechanism. This can be explained by the fact that CIP exhibits pronounced zwitterion character.

Table 1. Removal efficiency of CIP onto different types of adsorbents.

Adsorbent	Experimental conditions	CIP removal efficiency (%)	Recyclability	Ref.
Nano-sized magnetite	C_0[a] = 33 mg dm^{-3} AD[b] = 10 g dm^{-3} pH = 5.97 t = 24 h	80	n.r.[c]	(Rakshit *et al.*, 2013)
Graphene hydrogel	C_0 = 50 mg dm^{-3} T = 25 °C $T \approx$ 36 h	75	n.r.	(Ma *et al.*, 2017)
Carbon from date palm leaflets	C_0 = 100 mg dm^{-3} AD = 2 g dm^{-3} pH = 6 T = 45 °C t = 48 h	56	n.r.	(El-Shafey *et al.*, 2012)
Activated carbon derived from mangosteen peel	C_0 = 50 mg dm^{-3} AD = 3 g dm^{-3} pH = 6 T = 25 °C t = 60 min	98	n.r.	(Tran *et al.*, 2022)
Fe_3O_4-modified PAC	C_0 = 100 mg dm^{-3} AD = 1 g dm^{-3} pH = 7 T = 25 °C t = 60 min	100	88% after eight cycles	(Al-Musawi *et al.*, 2021b)
GAC	C_0 = 10 mg dm^{-3} AD = 0.05 g dm^{-3} pH = 7 T = 25 °C t = 24 h	70	n.r.	(Zhu *et al.*, 2015)
Halloysite nanotubes	C_0 = 30 mg dm^{-3} AD = 1.7 g dm^{-3} pH = 5–6 T = 20 °C t = 90 min	95	95% after five cycles	(Cheng *et al.*, 2018)

γ-Al_2O_3 nanoparticles	C_0 = 20 mg dm^{-3} AD= 0.775 g dm^{-3} pH = 7.5 t = 46.25 min	53	n.r.	(Najafpoor *et al.*, 2019)
Biomaterials from banyan aerial roots	C_0 = 60 mg dm^{-3} AD = 1.2 g dm^{-3} pH = 8 T = 25 °C t = 48 h	97	n.r.	(Fan *et al.*, 2020)
Biochar-montmorillonite	C_0 = 25 mg dm^{-3} AD = 1 g dm^{-3} pH = 5–6 t = 400 min	86	n.r.	(Ashiq *et al.*, 2019)
Bentonite	C_0 = 20 mg dm^{-3} AD = 0.25 g dm^{-3} pH = 4.5 T = 22 °C t = 60 min	91	n.r.	(Genç & Dogan, 2015)
Fe-based carbon nanocomposite	C_0 = 80 mg dm^{-3} AD = 0.8 g dm^{-3} pH = 7 T = 25 °C t = 60 min	90	45% after six cycles	(Zahoor *et al.*, 2022)
Coal fly ash	C_0 = 160 mg dm^{-3} AD = 40 g dm^{-3} T = 40 °C t = 100 min	39	n.r.	(Zhang *et al.*, 2017)
Clinoptilolite	C_0 = 5 mg dm^{-3} AD = 2 g dm^{-3} pH = 6 T = 25 °C	99	n.r.	(Ngeno *et al.*, 2019)
Synthesized zeolites (A, X, Y)	C_0 = 150 mg dm^{-3} AD = 0.5 g dm^{-3} pH = 3 T = 20 °C t = 24 h	27–61.4	n.r.	(Zide *et al.*, 2018)
Commercial zeolites (A, X, Y)	C_0 = 150 mg dm^{-3} AD = 0.5 g dm^{-3} pH = 3 T = 20 °C t = 24 h	34–87	n.r.	(Zide *et al.*, 2018)

[a]Inital concentration, [b]adsorbent dose; [c]not reported.

2.4.2. Improving the CLI adsorption efficiency by modification

Although CLI has a good performance in removal of inorganic pollutants, particularly of heavy metal cations, ammonia, and different types of organics from water medium, many research efforts are directed towards modification of CLI in order to improve its

adsorption ability. A brief review on commonly applied methods is given in the following text.

Physical modification

This type of modification includes heating (thermal, microwave) or ultrasound treatments. High temperatures and physical irradiation eliminate impurities present onto surface or inside the pore of the CLI's lattice and improve ion exchange reaction (Zieliński *et al*., 2016).

Chemical modification

This modification includes acid-base treatments, use of cationic surfactants or conversion of CLI to a certain cation form (such as Na-CLI or H-CLI).

Acid treatments contribute to removing impurities and increasing porosity. In the treatment, hydrogen ions partially replace K^+, Ca^{2+} and Mg^{2+}.

Alkali treatments leads to decrease of the Si/Al ratio and increase in mesoporosity.

Treatments of CLI with water solution of different inorganic salts can lead to ion-exchange between parent cations and cations in the solution and/or to precipitation of metal species onto the CLI surface.

All mentioned modifications usually lead to increase of the specific surface area, pore volume, and change in pore size distribution. The surface charge and morphology of CLI can also be changed, or the new surface functional groups can be induced (Jevtić *et al*., 2014; Lofù *et al*., 2016). Table 2 shows change in the zeolite specific surface area with different types of modifications.

Table 2. Change in active surface area of zeolites after different modifications.

Zeolite	**Modifier**	**S_{BET}[a] ($m^2\ g^{-1}$)**		**Ref.**
		pristine	***modified***	
Natrolite	γ-Fe_2O_3	65	126	(Salem Attia *et al*., 2014)
Na-CLI	Fe(III) ions	42	117	(Jevtić *et al*., 2014)
CLI	Chitosan + Fe_3O_4	14	28	(Javanbakht *et al*., 2016)
H-CLI	GO* nanosheets	12	18	(Yu *et al*., 2013)

[a]Specific surface area obtained by BET analysis; *graphene oxide.

Since CLI surface is negatively charged, it exhibits a weak affinity towards anions and hydrophobic species, which limits its application in adsorption. Chemical modification of CLI can generate positively charged species (such as complex oxi-hydroxy species) or surfactant micelles, which allows CLI surface to become available to negatively charged ions or hydrophobic species (Muir *et al*., 2016).

The CLI surface can also be covered with different oxide particles which changes the surface charge, increases the active surface area, or forms new active sites for adsorption. It has been shown that co-precipitation of iron oxide nanoparticles, such as magnetite and

maghemite, can significantly enhance adsorption capacity of CLI for heavy metal cations and different organic substances.

Moreover, use of magnetite nanoparticles (Fe_3O_4-NPs) in adsorption process have been widely studied due to their high surface area and magnetic properties. However, pure Fe_3O_4-NPs as adsorbent are not economically feasible due to the particles' tendency to agglomeration. This can be overcome by coating zeolite with Fe_3O_4-NPs. The coating enlarges specific surface area and induce magnetism to zeolite.

Magnetic Fe_3O_4-NPs can be synthetized onto natural zeolite (NZ) by chemical co-precipitation of Fe(II) and Fe(III) salts from aqueous solution by addition of NH_4OH of NaOH. The synthesis involves the following reactions (Mohseni-Bandpi *et al*., 2016):

$$FeCl_2 \cdot 4H_2O + 2FeCl_3 \cdot 6H_2O + 8NH_4OH \rightarrow Fe_3O_4 + 8NH_4Cl + 14H_2 \qquad (1)$$

$$Fe_3O_4 + NZ + 14H_2O \rightarrow Fe_3O_4 - NZ \qquad (2)$$

It has been reported that the coating significantly increases CLI capacity for antibiotic cephalexin (CEP) (from 28% to 93%). This was explained by the increase of surface area and in number of active sites available for the CEP adsorption. The study also showed that the adsorption of CEP on zeolite strongly depends on pH, and partially on solution ionic strength, which indicates that electrostatic interactions are prevalent in the adsorption mechanism (Mohseni-Bandpi *et al*., 2016).

Furthermore, modification of NZ with maghemite nanoparticles (γ-Fe_2O_3-NPs) is shown to be a promising method for the efficient removal of different pharmaceuticals (e.g., diclofenac, naproxen, gemfibrozil, and ibuprofen). γ-Fe_2O_3-NPs has a high adsorption removal efficiency (more than 95% within 10 minutes) for pharmaceuticals (Salem Attia *et al*., 2013). In addition, γ-Fe_2O_3-NPs can also promote the removal of arsenic ions from aqueous solution. The removal efficiency achieved was 96% in only 15 minutes.

The prepared magnetic composite showed good separation properties by external magnetic field and good recovery ability by NaOH solution (0.1 M). About 94% of the initial capacity retained after five cycles (Salem Attia *et al*., 2014). Since both, magnetic Fe_3O_4 and CLI possess good ion trapping ability, the magnetic CLI-based composite (Fe_3O_4/CLI) was tested in selective removal of ions from sea and brackish water, i.e., desalination process (Kouli *et al*., 2018).

CLI was also modified with graphene oxide (GO) – a single layer nanosheet of oxygenated graphene. The oxygen functionalities in GO include epoxy and hydroxyl groups, which lie on the basal planes of the GO sheets, while carboxyl groups are mostly found at the GO edges. These oxygen containing functional groups make the GO nanosheets negatively charged and hydrophilic. GO has a strong propensity to interact with positively charged species such as metal ions, dyes, and biomolecules (Baig *et al*., 2019; W. Xu *et al*., 2019).

Modification of CLI with GO includes formation of hydrogen bonds between the hydroxyl and carboxyl groups on the GO surface and the silanol groups on the surface of CLI. This leads to the deposition of a monolayer of GO onto CLI surface, which can enhance the surface area and create new active sites. Also, electrostatic interactions between the negatively charged GO and the positively charged metal cations on the

zeolite surface can be driving force for GO deposition onto CLI (Gebhardt *et al*., 2014; M. R. Silva *et al*., 2020). This led to the formation of a stable GO/zeolite composite enhancing the adsorption of organics. These two mechanisms are illustrated in Figure 6. The oxygen functionalities present on the GO surface can also contribute to the formation of additional active sites, which improves the adsorption performance (Manjili *et al*., 2020).

Yu *et al*. coated CLI with GO nanosheets coupled with diazonium salt (carboxy-GO/CLI) and obtained an effective adsorbent for cationic dye rhodamine B. GO coating increased the CLI surface area for around 30%, increasing CLI capacity for dye for 26%, and adsorption equilibrium was reached within 60 minutes. The suggested mechanism includes electrostatic interactions, hydrophobic interactions (π–π stacking) and hydrogen bonding (Yu *et al*., 2013).

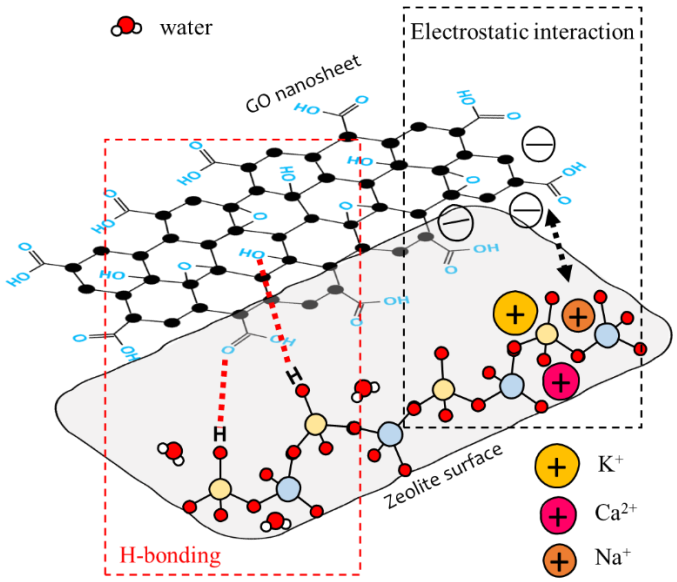

Figure 6. Possible mechanisms of GO-coated CLI.

2.5. Regeneration of spent adsorbents

One of the basic criteria for assessing the applicability of adsorption in a water treatment procedure is the ability of adsorbent to be reused. During adsorption, pollutant can be irreversibly adsorbed onto surface, which curbs adsorbent potential for reuse. Finding the adequate regeneration process for different adsorbent–adsorbate interactions (electrostatic, hydrophobic, π–π interaction, H-bonding) is of great importance for further commercialization of the procedure since the reusability of adsorbents can significantly reduce the process cost.

Desorption process depends on chemical nature of the adsorbate, its polarity and charge, surface properties of adsorbent (chemical nature of functional groups), adsorbent structural features (pore dimensionality and geometry), and thermal and chemical stability of the adsorbent. Generally, *desorption efficiency* is determined as relationship between

the removed amount of adsorbate and the amount of adsorbate retained on the exhausted adsorbent. This parameter is generally used to analyse the efficiency of the regeneration method without causing degradation. On the other hand, *regeneration efficiency* is measured by difference between the adsorbent's capacity in the first adsorption cycle and after the reactivation cycle.

The unique structural features as well as physico-chemical properties of natural zeolite enable zeolites to be regenerated. Regeneration of the zeolite-based adsorbents is usually based on relatively simple methods: desorption of the adsorbate, reverse ion-exchange, or adsorbate degradation.

The usual methods for regeneration can include the following treatments:

- Thermal,
- Chemical,
- Biological.

To classify these treatments, double criterion based on two fundamental aspects is used: (i) *the mechanism of the regeneration* which considers a different regeneration pathways and (ii) *the type of regeneration agent* that induces the regeneration. The regeneration methods are shown in Figure 7.

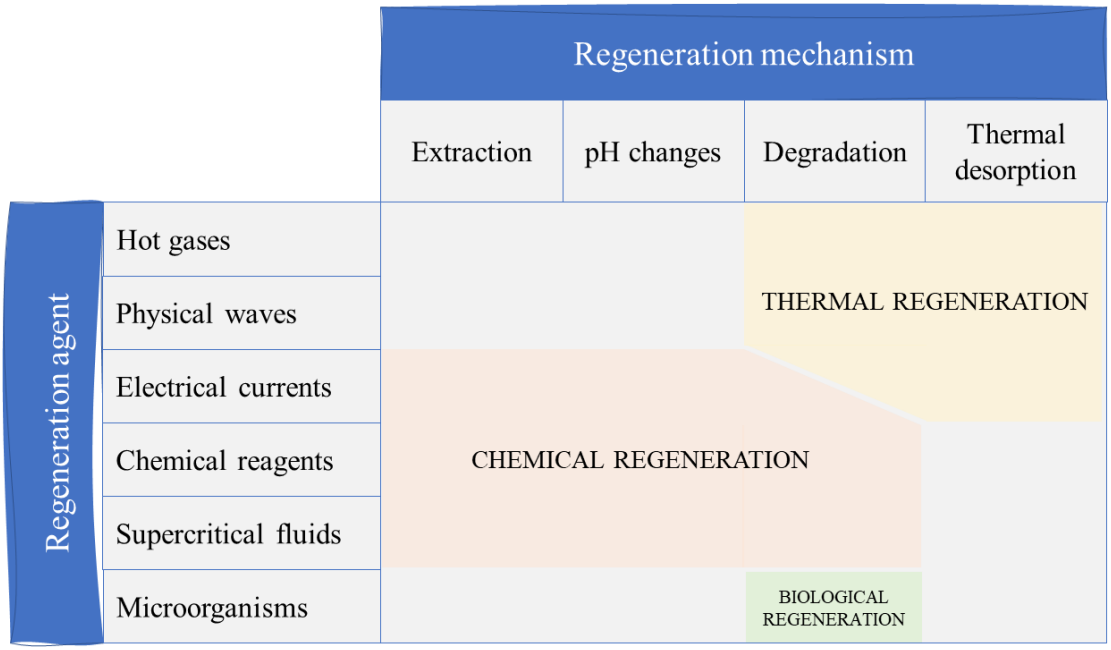

Figure 7. Classification of regeneration methods of zeolite-based adsorbents (adapted from Salvador *et al.*, 2015a).

Thermal regeneration

Thermal methods involve heating of the spent adsorbent by different heating techniques (hot inert gases or steam). It is necessary to provide enough energy needed for removal the adsorbate and preserve the zeolite structure. Thermal regeneration was mainly investigated for desorption of organic and carbon species from zeolite surface (Wang et al., 2006). Depending on chemical nature of adsorbate, the regeneration mechanism can include (Salvador *et al.*, 2015a):

- *One-step physical desorption* of adsorbate in its parent form (e.g., volatile organic adsorbate),
- *Thermal cracking* or *decomposition* of adsorbate,
- *Combination of partial desorption and thermal cracking* of the adsorbate (in case of chemisorption).

While one-step physical desorption does not leave any residue on the adsorbent, soot formation during thermal cracking is inevitable, reducing further regeneration efficiency.

Regeneration studies based on thermal treatments indicate positive results. Phenol adsorbed on the synthetic zeolite can be fully desorbed by thermal desorption up to 200 °C (Damjanović *et al.*, 2010). Mixtures of organic compounds (methyl tert-butyl ether/toluene, and methyl tert-butyl ether/1,2 dichloroethane) adsorbed onto high-silica ZSM-5 can be efficiently removed by thermal desorption (Rodeghero *et al.*, 2017). Graphene oxide/faujasite composite saturated with organic dye – methylene blue can be successfully regenerated by thermal annealing at 300 °C for 2 h. The adsorption capacity of composite was well preserved after four adsorption-regeneration cycles (Kim et al., 2018).

However, thermal treatments have disadvantages due to soot formation and usually high energy requirements. During the last decade, non-traditional thermal methods have been developed. The application of physical waves overcomes the insufficient heat and mass transfer during the regeneration process. The main advantage of non-traditional regeneration methods is their capability for molecular level heating, which enables homogeneous and fast regeneration rates, saving a significant amount of energy relative to other traditional thermal methods. So far, the microwave (MW)- and ultrasound (US)-assisted regeneration has been investigated for the zeolite adsorbents treatment. Around 86% of the adsorption capacity of natural zeolite saturated with cationic dye was regenerated using the MW irradiation for 10 minutes (Han *et al.*, 2010). The use of US-assisted regeneration showed good effect on water desorption from synthetic zeolite 13X (Daghooghi-Mobarakeh *et al.*, 2020).

Chemical methods

Chemical methods include solvent-assisted methods. This method is mainly applied for restoring the exchange capacity of zeolite since it is based on a reverse ion exchange reaction (Wang et al., 2006). Thus, the treatment of ammonia-loaded CLI with NaCl solution under alkaline conditions restored 96% of the CLI initial capacity (Castro *et al.*, 2021; Kaplanec *et al.*, 2017). The adsorbed phosphates can be removed from the spent Fe(III)-modified CLI by NaOH solution (Kaplanec *et al.*, 2017). Treatment with NaOH solution (< 0.1 M) was also found to be effective in desorption of arsenic ions from magnetic particle-coated zeolite and aluminium-loaded zeolite (94% and 91% of As ions was desorbed, respectively) (Salem Attia et al., 2014; Xu et al., 2002). Desorption of Pb(II) adsorbed on chitosan/CLI/magnetite composite was performed using HNO_3, $CaCl_2$ and NaCl solutions. Treatment in $CaCl_2$ and NaCl led to formation of a steady complex with Pb(II) ions, whereas in HNO_3 Pb(II) was replaced by H^+ ions. The highest regeneration rate was achieved in NaCl due to strong affinity of zeolite towards Na^+ ions (Javanbakht *et al.*, 2016). Similarly, in KCl solution Pb(II) also desorbed efficiently from CLI (up to 80%) (Katsou *et al.*, 2011). Good desorption rates were reported for Fe(II),

Cu(II), Zn(II) and Mn(II)) adsorbed onto CLI by using H_2SO_4 as desorbing agent (Motsi *et al*., 2009).

Chemical regeneration was also studied for desorption of organic species adsorbed onto different minerals. NaOH solution (0.01 M) was applied for desorption of insecticide diazinon from clay/graphene oxide/Fe_3O_4 composite. About 97% of the composite initial adsorption capacity was preserved after ten adsorption-regeneration cycles (Sohrabi *et al*., 2021). The CIP adsorbed onto clay mineral halloysite can be efficiently desorbed by 0.1 M NaOH, with the re-adsorption rate of 81.3% after four cycles (Duan *et al*., 2017).

Chemical regeneration also includes *oxidative* and *electrochemical regeneration* processes (Salvador et al., 2015). The oxidative regeneration of toluene-saturated CLI by O_3 combined with traditional thermal regeneration significantly reduced the amount of adsorbed toluene (Alejandro *et al*., 2014). According to Lei *et al.*, NH_3-loaded CLI can be completely regenerated through the electrochemical regeneration (Lei *et al*., 2009).

Although chemical regeneration methods reduce energetic requirements and improve the regeneration efficiency in comparison to traditional thermal methods, they also have drawbacks. Apart from the possible adverse effects of acid or base on adsorbent chemical structure (and subsequently decrease in adsorption capacity), the environmental footprint due to the generation of waste solvents may end up making this method less attractive (Dutta *et al*., 2019).

Regeneration based on biological processes

Biological methods refer to the processes of adsorbent recovering by degradation of the adsorbed organic species using different microorganism cultures. The advantages of biodegradation are its simplicity, low investment requirements, and environmentally friendly nature. This type of regeneration is mainly applied for the regeneration of NH_4-loaded CLI (Kalló, 2001). Semmens & Goodrich reported that the NH_4-saturated CLI can be regenerated up to 80% in a period of 1–3 h by nitrifying sludge at about 27 °C (Semmens' & Goodrich, 1977). However, long treatment time and low efficiency make this method generally unfeasible from a practical point of view (Dutta *et al*., 2019).

2.5.1. Application of plasma in regeneration process

Although conventional regeneration methods are still the most applied, their effectiveness are limited due to the complex interactions between adsorbent and organics. In addition, high energy demands, and sludge formation impose the need for the development of alternative technologies that can overcome these limitations and improve the efficiency of regeneration from ecological and economic points of view.

Recently, regeneration using plasma has brought novelty to the field of material functionalization. Plasma is partially or fully ionized gas which is in terrestrial conditions formed by an electric field. Generally, plasma consists of neutral and excited molecules, ions, free radicals, and UV and other photons which provide sufficient energy to promote different chemical reactions (Mirzaei *et al*., 2019). According to the difference in temperature of species inside plasma, plasmas can be divided as:

- thermal plasmas, and
- non-thermal or low-temperature plasmas.

In thermal plasmas, a condition for local thermodynamic equilibrium is fulfilled, which means that all species in plasma have approximately the same temperature (usually in the range 4000–20,000 K). These kind of plasmas have high density of charged species. On the other hand, non-thermal plasma (NTP), also known as *cold plasma*, exists in thermodynamically non-equilibrium state in which electrons reach much higher temperatures than other species. Thus, non-thermal plasmas are a source of high energy electrons and various species under ambient conditions (Lee *et al.*, 2017). In these systems densities of charged species are much less in comparison to the thermal plasmas.

Non-thermal plasma can be produced at low and atmospheric pressure. In low-pressure plasmas, a lower breakdown potential to ignite plasma is required enabling a possibility to acquire a chemically rich environment in larger active plasma volumes. Species generated in plasma, such as ions, radicals, and electrons, interact with the surface of treated material through several mechanisms, including physical sputtering, etching, and deposition, as well as chemical reactions such as polymerization, etc. However, requirement of low-pressure environment for their generation limits application of these plasma systems. On the other hand, atmospheric-pressure plasmas can be generated without pressure reduction providing a plasma-generated chemically rich environment at atmospheric pressure. But creating reactive chemistry in ambient air make interactions between plasma species and treated material more complex than in low-pressure plasma. Nevertheless, reactive species formed in atmospheric-pressure plasma can still interact with the surface of material and cause changes in its properties. The high-energy ions and radicals can induce physical and chemical modifications in materials, leading to enhancement of surface reactivity. Figure 8 summarizes the plasma classification by means of temperature and pressure characteristics.

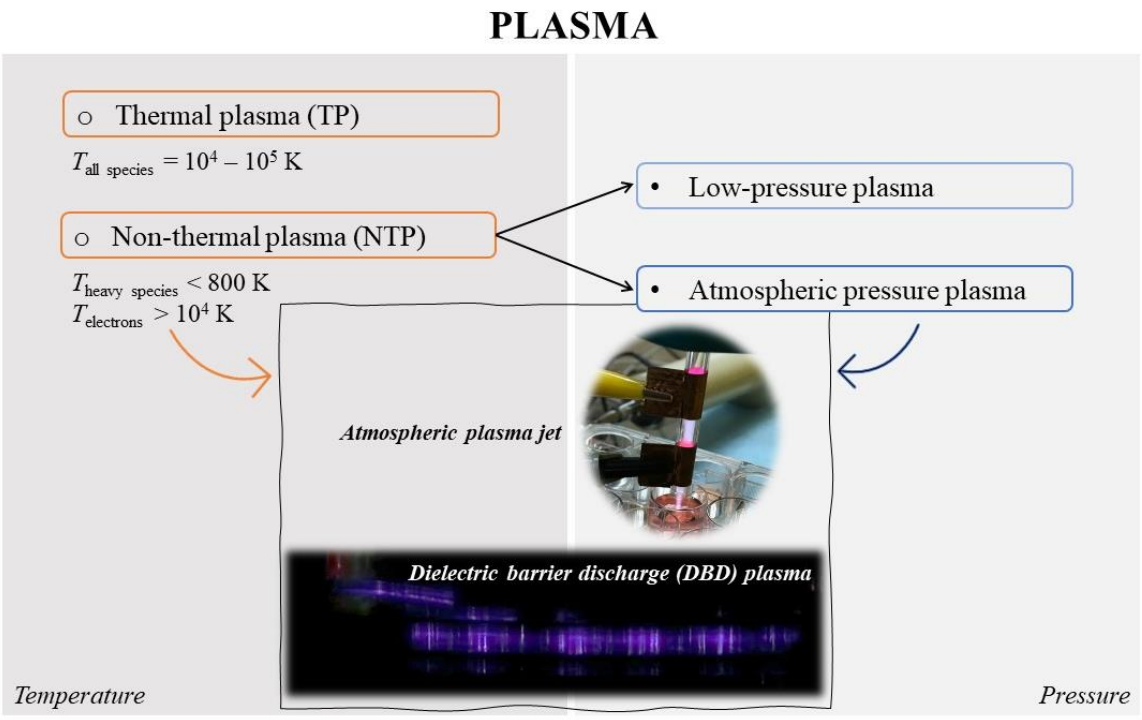

Figure 8. Classification of man-made plasmas.

However, NTPs operating at atmospheric pressure have an inherent drawback of limited active plasma volumes, which constrains both the effective treatment surface and the flux of the reactive species. These limitations pose an issue for large-scale applications.

To address this challenge, different geometrical configurations of electrodes are proposed enabling parallel operation of multiple discharge channels with limiting the current. One solution is to separate flat metallic electrodes with a dielectric creating a plane dielectric barrier discharge (DBD) type of plasma source that is powered by an alternating high-voltage signal. The dielectric layer is typically made of a material such as glass, silica glass or ceramic, and prevents direct electrical contact between the two electrodes, i.e. serves as a charge collector. Once sufficient charge is generated at the surface, it screens the outer electrical field thus extinguishing the discharge. The voltage signal then exchanges polarity of the electrodes again initiating the discharge. Such sources with a specific electrode geometry and dielectric insertion between the electrodes, along with different types of alternating high-voltage signals, enable creation of the discharge mostly close to the dielectric surface. Thus, they are known as surface dielectric barrier discharge (SDBD) (Brandenburg, 2018; Kogelschatz, 2003). Apart from the discharge distributed over the electrode surface in many cases inside a gap between electrodes, a large number of microchannels or filaments can be formed, which are characterized by their small size (up to 100 µm in radius). Both surface discharges and micro-channels generate a high concentration of reactive species, which can interact with the surface of the material being treated. In comparison to other NTP sources that operate at atmospheric pressure, SDBD sources are capable of generating plasma over large surfaces with limited discharge current.

In general, plasma interaction with material's surface can be roughly divided into four general processes including (Figure 9) (Yavuz & Saka, 2013):

- *Surface activation* by bond cleavage to create reactive sites,
- *Grafting* of chemical moieties and functionalities,
- *Etching* – material volatilisation and removal,
- *Cleaning or scouring* – dissociation of surface contaminants or layers and deposition of conformal coatings.

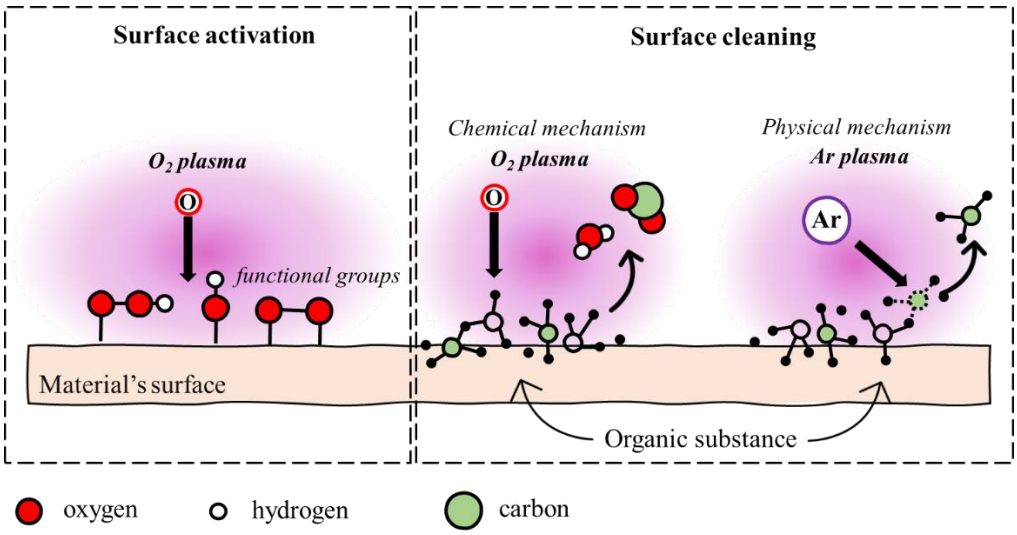

Figure 9. Scheme of possible mechanisms of materials' surface activation and surface cleaning by reactive species formed in plasma.

NTP has been investigated for the surface activation and modification of various adsorbent materials, including carbonaceous materials, clay minerals, zeolites. Namely, oxygen plasma could increase the number of oxygen groups on the surface of carbon-based materials, as well as increase the material hydrophilicity and improve wettability. The created oxygen groups on the surface of carbonaceous materials include carboxylic, phenolic and carbonyl groups. According to the De Velasco Maldonado *et al.*, cold oxygen plasma can selectively oxidize the carbon-based materials, and thus significantly increase the carbon's adsorption capacity for Pb(II) (de Velasco Maldonado *et al*., 2016). Furthermore, the capacity of synthetic zeolite-A for Cd(II) ions removal increased for approximately 10% after the oxygen plasma treatment. Although zeolite surface cannot be significantly chemically modified by oxygen plasma treatment. However, oxygen plasma has the ability to increase the amount of oxygen functionalities on zeolite's surface, as well as clean the zeolite's surface by increasing the pore openings and removing of captured organic species via sputtering (Fahmy *et al*., 2019). NTP treatment was also investigated for the surface modification of clay mineral kaolin in order to improve its adsorption capacity for MB dye. The results showed significant increase in kaolin's capacity for MB (from 19.60 to 51.02 mg g^{-1}) after the NTP modification (Yavuz & Saka, 2013). Apart from plasmas at low pressures, a surface modification of natural zeolite was investigated using the DBD plasma operating at atmospheric pressure. After the DBD plasma modification, the natural zeolite's capacity for toxic Sr(II) ions increased more than 56%. Several new functional groups were observed on the plasma-treated zeolite, and its microporosity increased for 35% in comparison to untreated material (Mirzaei *et al*., 2019).

Reactive species generated in a NTP operating at atmospheric pressure in air include a variety of radicals, ions, excited atoms and molecules, and neutral species that can be divided as reactive oxygen (ROS) and nitrogen (RNS) species (•O, •OH, H_2O_2, O_3, O_2, N_2*, NO, N_2O, etc.). In particular, the presence of short-lived OH radicals is attributed to the dissociation of water molecules in NTP. Generation of long-lived reactive species such as ozone (O_3) and nitrogen (NO_x and HNO_x) is also present in DBD plasma in air. These species play an important role in inducing chemical reactions that result in the

destruction of organic pollutants and intermediate molecules. The species originate from plasma chemistry reactions depend on various operating parameters of the plasma source, such as applied power/voltage, electrode gap, pressure (in the case of low-pressure plasma), and the obtained plasma conditions (electron and ion density, field intensity, etc.). Hence, plasma sources produce a reactive chemical environment, enabling short treatment times of samples without the need for additional chemicals or the production of toxic waste. Additionally, in many cases, plasma systems have a low energy consumption. Such environmentally friendly characteristics represent the primary benefits of plasma treatment relative to conventional methods in different pollutant degradation and in possibility for adsorbents' capacity regeneration.

3. EXPERIMENTAL PART

3.1. Materials

Zeolitic tuff

The clinoptilolite-rich zeolitic tuff (CLI) obtained from the Serbian deposit Slanci (near the capital Belgrade) was used in this study. Prior to the experiments, the sample was sieved to obtain the particle size in the range of 0.063–0.125 mm, since previous experimental work showed the best adsorptive performances for that particle size range (Rajic *et al*., 2010; Stojakovic *et al*., 2012). The sample was then washed with deionized water for several times to remove impurities and dried in an oven at 105 °C until a constant mass.

Chemicals

All chemicals were of analytical grade and were used as received, without purification:

- Ciprofloxacin ($C_{17}H_{18}FN_3O_3$, ≥98%, Sigma Aldrich)
- Iron(III) chloride hexahydrate ($FeCl_3 \cdot 6H_2O$, p.a., Centrohem)
- Iron(II) chloride tetrahydrate ($FeCl_2 \cdot 4H_2O$, p.a., Lachema)
- Iron(II) sulphate heptahydrate ($FeSO_4 \cdot 7H_2O$, p.a., Lachner)
- Ammonium hydroxide (NH_4OH, 25 v/v%, Zorka Pharma)
- Sodium hydroxide (NaOH, p.a., Carlo Erba)
- Graphene oxide water dispersion (4 mg cm^{-3}, Graphenea)
- Ethanol (C_2H_5OH, p.a., Sigma Aldrich)
- Silver nitrate ($AgNO_3$, p.a., Sigma Aldrich)
- Hydrochloric acid (HCl, p.a., Zorka Pharma)

To provide a comprehensive understanding of the experimental work, Figure 10 gives a simplified summary of the subsequent experimental steps, which are detailed in Chapters 3.2.–3.4.

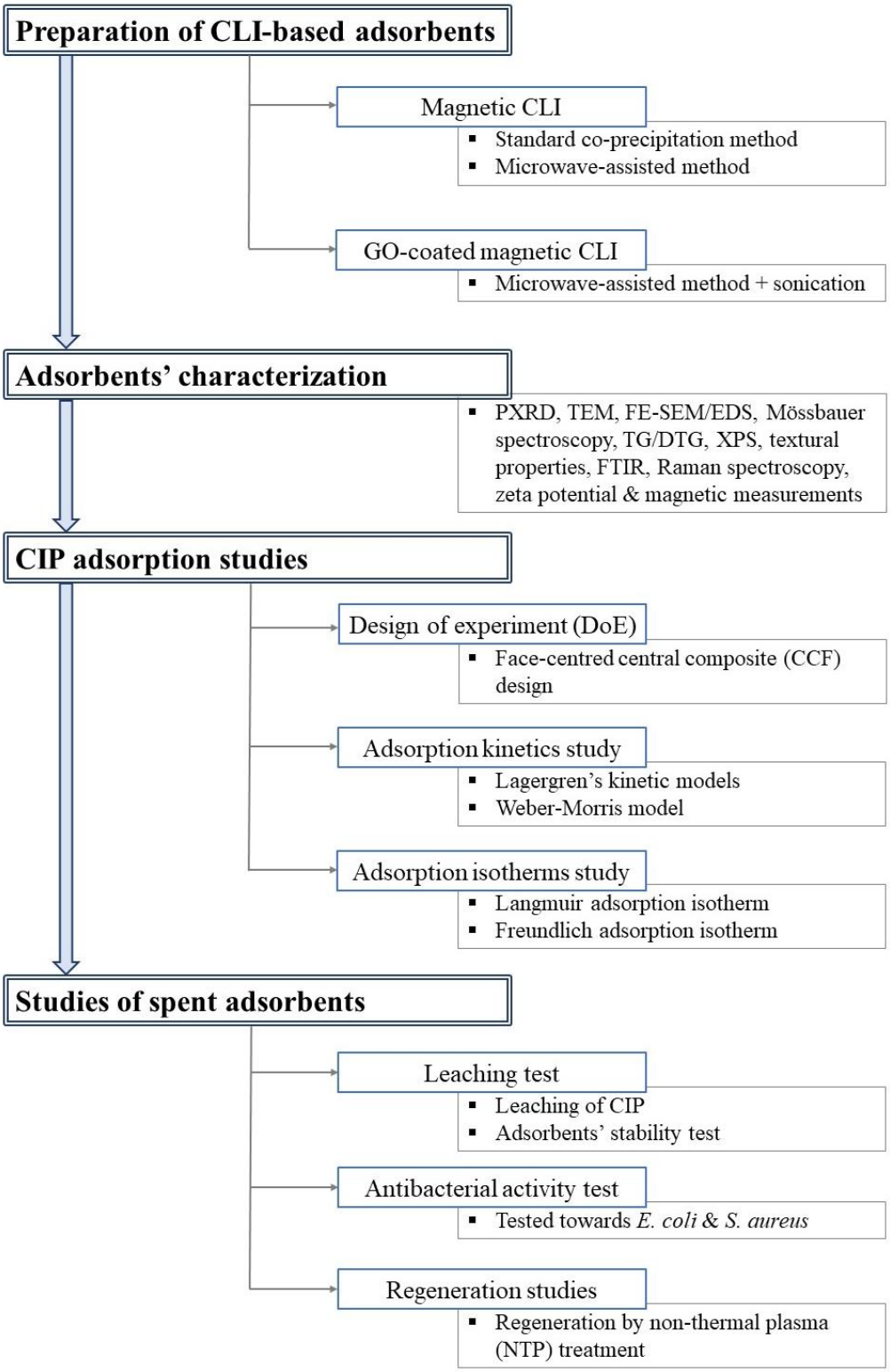

Figure 10. Flow chart of experimental work.

3.2. Modification procedures

Preparation of magnetic nanoparticles (MAG)

Co-precipitation method:

The synthesis combined two reported procedures (Ahribesh *et al*., 2017; Khalil, 2015). $FeCl_3 \cdot 6H_2O$ and $FeCl_2 \cdot 4H_2O$ in a molar ratio of 2:1 were dissolved in degassed distilled water under N_2 atmosphere and NH_3 solution (25 wt.%) was added dropwise until pH reached 10. Black precipitate (MAG_{CP}) was formed and then magnetically separated by applying external magnetic field; it was washed with distilled water until a negative reaction to Cl^- ions. MAG_{CP} was then left to dry at 80 °C overnight to a constant mass.

Microwave-assisted method:

The synthesis was performed by microwave-assisted procedure described by Pati *et al.* (Pati *et al*., 2014). Aqueous solutions of $FeCl_3 \cdot 6H_2O$ (0.4 mol dm^{-3}) and $FeSO_4 \cdot 7H_2O$ (0.2 mol dm^{-3}) applied in a molar ratio of 2:1 were mixed properly. Water solution of NaOH (2.0 mol dm^{-3}) was then added and the solution was microwave (MW) irradiated at 200 °C for 5 minutes (Microwave Reaction System SOLV, Multiwave PRO, Anton-Paar GmbH, Graz, Austria). Inner pressure and temperature were monitored during the synthesis. The obtained black precipitate (MAG_{MW}) was separated from the liquid phase by centrifugation, washed several times with deionised water and dried at 80 °C until a constant mass.

Preparation of magnetic clinoptilolite (MAG-CLI)

Standard co-precipitation method:

Magnetic clinoptilolite with approx. 12 wt.% of MAG_{CP} was prepared following a slightly modified method described by Mohseni-Bandpi *et al.* (Mohseni-Bandpi *et al*., 2016). Firstly, 10 g of CLI was suspended in 120 cm^3 of deionized water and stirred under the N_2 atmosphere at 350 rpm for 10 minutes. Then, a solution of $FeCl_3 \cdot 6H_2O$ and $FeSO_4 \cdot 7H_2O$ in a molar ratio of 2:1 was added to the CLI suspension under stirring. The pH of the suspension was adjusted to ~10 by the dropwise addition of NH_4OH solution (25 wt.%). The suspension was vigorous stirred in a water bath at ~80 °C under N_2 for 1 h. The resulting dark brown precipitate (MAG_{CP}-CLI) was separated from the suspension by centrifugation and washed several times with deionized water until a negative reaction to Cl^- ions. The obtained MAG_{CP}-CLI was left to dry at 80 °C overnight until a constant mass.

Microwave-assisted method:

The procedure was carried out using a slightly modified method described by Iskandar *et al.* (Iskandar *et al*., 2014). The aqueous solutions of $FeCl_3 \cdot 6H_2O$ (0.4 mol dm^{-3}) and $FeSO_4 \cdot 7H_2O$ (0.2 mol dm^{-3}) in molar ration of 2:1 were mixed properly with CLI water suspension at room temperature. Subsequently, the aqueous solution of NaOH (2.0 mol dm^{-3}) was added dropwise to the prepared suspension until the pH reached 10. The formed black suspension was transfer to four Teflon vessels and MW irradiated at 200 °C for 5 minutes under high stirring. Inner pressure and temperature were monitored during the synthesis. The obtained dark brown precipitate (MAG_{MW}-CLI) was separated from

the suspension by centrifugation and washed several times with deionized water until a negative reaction to Cl^- ions. The MAG_{MW}-CLI was then dried in the oven at 100 °C until a constant mass. The sample was stored in a dry atmosphere until its further use.

Preparation of graphene oxide-coated clinoptilolite (GO-CLI)

Graphene oxide (GO) water dispersion was mixed with ethanol and treated in an ultrasound bath (Giorgio Bormac, DU-32) for 30 minutes to ensure the proper exfoliation of GO interlayers (Muhamad *et al*., 2016). Afterwards, the CLI powder was added to the GO dispersion in a mass ratio of GO/CLI= 0.5. The suspension was ultrasonically treated for 30 minutes (40 kHz, 120 W) and then stirred for 30 minutes until the full ethanol evaporation. The obtained black suspension (GO-CLI) was dried at ~80 °C until a constant mass.

Preparation of graphene oxide-coated magnetic clinoptilolite (GO-MAG_{MW}-CLI)

Water dispersion of GO (3.6 cm^3) was added to ethanol (11.4 cm^3), mixed and ultrasonicated (Giorgio Bormac, DU-32) for 30 min to achieve the proper exfoliation of GO interlayer structure (Muhamad *et al.*, 2016). Then, the MAG_{MW}-CLI powder was added to the GO dispersion in a weight ratio of GO/MAG_{MW}-CLI = 0.5. The suspension was alternately treated with ultrasound for 30 minutes (40 kHz, 120 W) and stirred for 30 minutes until all added ethanol evaporated. Thickened suspension (GO-MAG_{MW}-CLI) was placed in an oven at 80 °C and dried overnight to a constant mass.

3.3. Materials characterization: methods and techniques

3.3.1. Methods

Determination of cation exchange capacity (CEC) of the zeolitic tuff

CEC of the used CLI was determined by a standard procedure based on the ion-exchange reaction with 1.0 mol dm^{-3} ammonium acetate solution at room temperature for 24 h (Schollenberger, 1945). The concentration of Na^+, K^+, Ca^{2+} and Mg^{2+} in filtrates was measured, and the CEC value was expressed in mmol M^+ per 100 g of CLI.

Adsorption studies

The CIP adsorption experiments were carried out using a batch method. The adsorption capacity of CLI, MAG_{CP}-CLI, MAG_{MW}-CLI and GO-MAG_{MW}-CLI towards CIP was investigated as a function of different adsorption parameters, such as adsorbent dosage, pH, temperature, initial concentration of CIP solution and time. The stock CIP solution (200 mg dm^{-3}) was prepared by dissolving an appropriate amount of CIP powder in acidified deionized water (pH adjusted to 3 with 0.1 mol dm^{-3} HCl). The mixture was left to stir at a magnetic stirrer and room temperature until completely dissolved. The chosen concentrations of CIP solution used in the further experiments (15–50 mg dm^{-3}) were prepared by diluting the stock solution with deionized water. The influence of abovementioned parameters on the adsorption efficiency was investigated as follows:

- The influence of adsorbent dosage was investigated only for the pristine CLI and MAG_{CP}-CLI at 25 °C by shaking a different amounts of CLI and MAG_{CP}-CLI (0.05, 0.10, 0.15 and 0.20 g) with 50 cm^3 of CIP solution (C_0 = 50 mg dm^{-3}) at pH

of 5 for 60 min in a thermostated water bath (Memmert, WBE 22) to optimize the solid-liquid ratio for CIP adsorption.

- The influence of solution pH was investigated at 25 °C by shaking 4 g dm^{-3} of CLI, MAG_{CP}-CLI, MAG_{MW}-CLI and GO-MAG_{MW}-CLI in CIP solution (C_0 = 50 mg dm^{-3}) of different pH (3, 5, 7 and 9) for 60 min in a thermostated water bath (Memmert, WBE 22).
- The influence of the initial CIP concentration, pH, temperature, contact time and adsorbent type onto adsorption capacity for CIP was studied by shaking the 0.2 g of adsorbent (CLI, MAG_{MW}-CLI or GO-MAG_{MW}-CLI) and 50 cm^3 of CIP solution of known concentration (15–50 mg dm^{-3}) for 20 min in a thermostated laboratory orbital shaker-incubator (ES-20/80, Biosan, Riga, Latvia) at different temperatures (10–20 °C). The obtained experimental data were used for statistical analysis using the response surface methodology (RSM) in order to determine the influence of parameters and their combinations on CIP adsorption efficiency.

Design of experiment (DoE)

A Design Expert software (version 13) was used to optimize the CIP adsorption process onto CLI-based adsorbents through a design of experiment (DoE) approach. The purpose of DoE is to create an empirical mathematical model that can predict the outcome of a dependent variable apropos a group of independent variables. By applying the DoE, the significance of each independent variables and their combination in relation to the outcome can be quantified.

The results of the adsorption experiments were obtained by a face-centred central composite design (CCF) with five independent variables (or factors) varied across three levels (Table 3). The chosen response variable was the adsorbents' adsorption capacity for CIP.

Table 3. Design parameters and response variable selected for the experiment.

Factor	**Unit**	**Range and level**		
		Low (–1)	***Central (0)***	***High (+1)***
X_1: A – Initial CIP concentration	mg dm^{-3}	15	32.5	50
X_2: B – pH		5	7	9
X_3: C – Temperature	ºC	10	17.5	25
X_4: D – Contact time	min	5	12.5	20
		E[1]		E[2]
X_5: E – Adsorbent	Categorical	CLI	MAG_{MW}-CLI	GO-MAG_{MW}-CLI
RESPONSE				
Adsorption capacity (q)	mg g^{-1}			

The number of experiments performed for the full factorial CCF design were calculated according to the equation $N = 2^k + 2k + n_c$, where 2^k represents the number of factorial points, $2k$ is the axial points, with k as the number of factors, and n_c as the number of replicates at the centre point.

A statistical analysis which includes an analysis of variance (ANOVA) and prediction of regression coefficients, response surface and contour plots was applied. The threshold of 5% significance level is commonly used to classify the statistical significance of the evaluated statistical properties of the model.

Adsorption kinetics

The adsorption kinetics were studied by shaking 0.2 g of each adsorbent (CLI, MAG_{CP}-CLI, MAG_{MW}-CLI or GO-MAG_{MW}-CLI) with 50 cm^3 of a CIP aqueous solution (C_0 = 15, 25 and 50 mg dm^{-3}) at pH of 5 and 10, 15, 20 °C in a thermostated water bath (Memmert, WBE 22) for an adsorption contact time from 5 to 60 minutes.

The commonly used kinetic models in adsorption, including Lagergren's pseudo-first-order, Lagergren's pseudo-second-order and Intra-particle diffusion (Weber-Morris) model, were applied to the obtained kinetic data for CIP adsorption to identify the dynamics of the adsorption process. For the aforementioned models, the kinetic rate constants were calculated, and the linear regression correlation coefficient (R^2) values were compared to evaluate the best model fit.

Lagergren's kinetic models

The assumption of the Lagergren's pseudo-first-order model (Lagergren, 1898) is that the change of adsorbate uptake with time is directly proportional to difference in saturation concentration of the adsorbate, which is generally applicable over the initial stage of an adsorption process driven by the diffusion through the interfaces (surface diffusion).

The non-linear form of pseudo-first-order model can be expressed by the equation:

$$\frac{dq_t}{dt} = k_1(q_e - q_t) \tag{1}$$

where q_e (mg g^{-1}) and q_t (mg g^{-1}) are the adsorption capacity at equilibrium and at contact time t, respectively, and k_1 (min^{-1}) is the first-order kinetic rate constant. Further modification of Equation (1) by integration using the boundary conditions t = 0–t, and q_t = 0 (t = 0)–q_e (t = t), lead to the following linear form:

$$\log(q_e - q_t) = logq_e - \frac{k_1}{2.303}t \tag{2}$$

According to the Equation (2), the plot of log (q_e–q_t) versus t is a straight line if the experimental data follow this kinetic model, and the equation provides estimates of q_e and k_1 from the intercept and the slope of the plot, respectively. Moreover, the linear regression coefficient R^2 also indicates the conformity of the model.

The Lagergren's pseudo-second-order model (Lagergren, 1898) assumes that the rate-limiting step in the adsorption is chemisorption. Thus, the rate of the adsorption is dependent on the adsorption capacity, and not on the adsorbate concentration (Sahoo & Prelot, 2020). The advantage of this kinetic model is the possibility of calculating the maximum adsorption capacity from the model, so there is no need for adsorption capacity evaluation from the experiment.

The pseudo-second-order rate equation can be described by following equation:

$$\frac{dq_t}{dt} = k_2(q_e - q_t)^2 \quad (3)$$

where k_2 (g mg^{-1} min^{-1}) is the rate constant of the pseudo-second order adsorption. Integration between the same limits as above gives the following expression:

$$\frac{t}{q_t} = \frac{1}{k_2 q_e^2} + \frac{1}{q_e} t \quad (4)$$

The plot of t/q_t vs. t is a straight line if the experimental data conform to this kinetic model and the values of q_e and k_2 are obtained from the slope and intercept of the plot, respectively.

Intra-particle diffusion model (Weber-Morris)

To identify the influence of diffusion in the CIP adsorption, the intra-particle mass transfer diffusion model proposed by the Weber and Morris (Weber & Morris, 1962) was applied.

The following equation defined this model:

$$q_t = K_{id} t^{1/2} + I \quad (5)$$

where K_{id} (mg g^{-1} min$^{-1/2}$) is the intra-particle diffusion rate constant and I (mg g^{-1}) is the parameter related to the thickness of the boundary layer.

If the intra-particle diffusion is involved in the adsorption process, the plot of q_t versus the square root of time ($t^{1/2}$) represents a straight line. The K_{id} and I are evaluated from the slope and the intercept of the regression line. Furthermore, the intra-particle diffusion is the rate-controlling step in the adsorption process if the line passes through the origin. However, this is not always the case, and the line can contain multiple linear sections suggesting that the intra-particle diffusion in not the only rate-limiting step. The adsorption can also be controlled by the adsorbate diffusion from the bulk of the solution to the liquid film surrounding the solid adsorbent particle, by the surface diffusion (adsorbate moving from the liquid film to the bare adsorbent surface) or by the pore diffusion (adsorbate migration to the pore system of the adsorbent) (Sarma *et al.*, 2019).

Adsorption isotherms

Generally, the adsorption isotherms describe how different adsorbates interact with an adsorbent via the relationship between the equilibrium adsorption capacity (q_e) and adsorbate equilibrium concentration (C_e) at constant temperature. The isotherms provide the information about the adsorbent's capacity, surface properties and adsorption mechanism that are essential when designing the adsorbent-adsorbate system (Sarma et al., 2019).

The obtained adsorption equilibrium data were analysed by two widely applied empirical adsorption isotherm models – Langmuir and Freundlich isotherm models.

Langmuir adsorption isotherm

The Langmuir model (Langmuir, 1918) is represented as:

$$q_e = \frac{q_{max} \cdot b_L \cdot C_e}{1 + b_L \cdot C_e} \quad (6)$$

where C_e is the equilibrium concentration of CIP (mg dm^{-3}), q_e is the amount of adsorbed at equilibrium (mg g^{-1}), while q_{max} (mg g^{-1}) and b_L (dm^3 mg^{-1}) are Langmuir constants for the maximum achievable uptake by the system, and a constant related to the affinity between adsorbate and adsorbent, respectively.

The linear form of Langmuir isotherm is expressed by following:

$$\frac{C_e}{q_e} = \frac{1}{q_{max}} + \frac{1}{q_{max} b_L} \quad (7)$$

The assumptions of the model include energetically identical adsorption sites and no interactions between adjacent adsorbate species on adsorbent's surface which results that adsorption does not proceed beyond a monolayer (Langmuir, 1918).

The Langmuir isotherm can also be expressed by a dimensionless separation factor – R_L (Equation (8)) to predict the favourability of the adsorption process.

$$R_L = \frac{1}{1 + b_L C_0} \quad (8)$$

In Equation (8), the b_L is the Langmuir adsorption equilibrium constant related to the adsorption energy (dm^3 mg^{-1}) and C_0 is the highest investigated initial concentration of the adsorbate (mg dm^{-3}).

According to the R_L value, the adsorption process can be favourable for $0 < R_L < 1$, unfavourable for $R_L > 1$, linear for $R_L = 1$ or irreversible for $R_L = 0$.

Freundlich adsorption isotherm

The Freundlich isotherm model is used to describe the adsorption onto heterogeneous surface with respect to the adsorption sites distribution throughout the adsorbent surface. The model considers the multilayer adsorption with the interactions between adsorbed species (Freundlich, 1906). It is described with the following equation:

$$q_e = K_f \cdot C_e^{1/n} \quad (9)$$

where C_e is the equilibrium concentration of CIP (mg dm^{-3}), q_e is the equilibrium concentration of the adsorbed CIP (mg g^{-1}), K_f is the Freundlich isotherm constant (mg g^{-1}) and n is a parameter related to the adsorption intensity or binding strength.

Equation (9) can be rearranged to a linear form (Equation (10)) which determination of adsorption capacity makes easier.

$$log q_e = log K_f + \frac{1}{n} log C_e \quad (10)$$

The values of K_f and n can be determined from the intercept and slope of the log q_e versus log C_e linear plot, respectively. The nature of the adsorption process is indicated by the Freundlich constant n: $n \leq 1$ refer to chemisorption, while $n > 1$ indicate physisorption.

3.3.1.1. Leaching experiments

The leaching of the adsorbed CIP was performed in a batch system. The 0.2 g of spent CLI or MAG_{CP}-CLI (CLI-CIP or MAG_{CP}-CLI-CIP) which contained around 21 mg CIP per gram of the adsorbent, were suspended in 50 cm^3 of 0.1 mol dm^{-3} NaCl and left for 24 h shaking in a thermostated water bath (Memmert, WBE 22) at 25 °C. The solid adsorbent was separated from the suspension by vacuum filtration. After filtration, the content of CIP in the filtrate was determined by the UV-Vis measurements. The desorbed amount of CIP was calculated as the ratio of the CIP amount in the solution and on the adsorbent.

The concentration of the exchangeable cations (K^+, Mg^{2+} and Ca^{2+}) and iron in filtrates after the CIP adsorption was measured using the atomic adsorption spectroscopy (Varian SpectrAA, 55B).

3.3.1.2. Antibacterial activity test

The antibacterial activity of CIP-containing CLI (CLI-CIP and MAG_{CP}-CLI-CIP) was tested towards the Gram-negative bacterium *Escherichia coli* strain DSM 498 and the Gram-positive bacterium *Staphylococcus aureus* strain ATCC 25923. Bacteria were pre-grown on a nutrient agar (NA, Torlak, Serbia) for 16 h at 37 ± 0.1 °C to obtain cultures in the log phase of growth. Prior to the experiments, the samples were sterilized by UV light for 30 min.

The standard disk diffusion method by the Kirby-Bauer was used for a qualitative assessment of antibacterial activity. The biomass of each bacterial strain was separately suspended in a sterile physiological solution to achieve the bacterial concentration of about 109 CFU cm^{-3} (colony forming units). The inoculum was then swabbed onto the surface of NA. Antibacterial activity was tested as follows: 0.01 cm^3 of suspensions containing 5, 10 or 20 mg of CIP, CLI-CIP, or MAG_{CP}-CLI-CIP per cm^3 in a sterile phosphate buffer solution (pH = 7.02) was dropped onto the bacteria inoculated NA and the plates were incubated for 24 h at 37 °C. The results were reported as the presence or absence of the inhibition zone.

3.3.2. Instrumentation

Atomic adsorption spectroscopy (AAS)

The concentration of exchangeable metal cations in filtrates was measured using an AAS, Varian SpectrAA, 55B (SpectraLab Inc., Markham, ON, Canada). The measurement accuracy was ± 2%. All measurements were taken in accordance with the manual's instructions.

Powder X-ray diffraction (PXRD)

PXRD analysis was performed to determine the mineral phases present in the samples and to investigate the CLI crystallinity after the modifications and regeneration treatment. PXRD patterns of the prepared samples were obtain using a Rigaku SmartLab powder diffractometer (Rigaku, Tokyo, Japan) with CuKα radiation (λ = 1.54178 Å) generated at 40 kV and 30 mA and Bragg-Brentano focusing geometry. The samples were scanned in the 2θ range 5–65° with a step of 0.01° and a scan rate of 5° min^{-1}. The Rietveld

refinement and the Topas-Academic v.4 software package (Coelho, 2007) were used for the semi-quantitative PXRD analysis of zeolitic tuff.

To perform the detailed identification of crystal iron oxide phases in the MAG_{MW} and MAG_{MW}-CLI samples, the diffractogram of MAG_{MW} was subsequently recorded using a D8 Advance (Bruker, Billerica, MA, USA) diffractometer in step-scan mode with a 0.02° 2θ step, in the 2θ range of 5–65°, at 0.6 s $step^{-1}$. The quantitative analysis of the obtained MAG_{MW} and MAG_{MW}-CLI diffractograms was performed using a reference intensity ratio (RIR) method and a Crystal Impact Match! software package.

Transmission electron microscopy (TEM)

TEM analysis of MAG_{CP}, MAG_{MW}, MAG_{CP}-CLI and MAG_{MW}-CLI samples was carried out at 200 kV using a transmission electron microscope (JEM-2100, JEOL Ltd., Tokyo, Japan) equipped with an ultra-high-resolution objective lens pole piece with a point-to-point resolution of 0.19 nm. The samples preparation consisted of crushing a sample in an agate mortar, dispersing in absolute ethanol to form a dilute suspension, and a fine fraction of the suspension was then placed on Cu holey carbon-coated grids. To determine the average size of iron oxide particles, their diameters were measured from the obtained TEM images. Due to the relatively small size of the iron oxide nanoparticles, the selected area electron diffraction (SAED) was performed over multiple nanocrystals to obtain the characteristic diffraction rings with the structure-specific *d*-values.

Field emission scanning electron microscopy (FE-SEM) coupled with energy dispersive X-ray spectroscopy (EDS)

Surface morphology and elemental composition of MAG_{MW}-CLI and GO-MAG_{MW}-CLI samples were investigated by a thermal field-emission scanning electron microscope (FE-SEM) equipped with an energy dispersive (EDS) analyser. FE-SEM images were collected by a Jeol JSM-7000F field-emission electron microscope (FE-SEM), while the EDS detector (Oxford Analysis) with INCA 350 EDS system (Oxford Instruments Ltd., Abingdon, UK) was used for quantification of elements. Prior to the analysis, the samples were carefully prepared in order to make them conductive.

Mössbauer spectroscopy

Room temperature Mössbauer spectra of MAG_{MW} and $MAG_{MW\text{-}CLI}$ samples were recorded in a transmission mode using a standard WissEl spectrometer configuration (Wissenschaftliche Elektronik GmbH, Starnberg, Germany). A ^{57}Co gamma Mössbauer source in Rh-matrix was used. The velocity scale and all recorded data were relatively calibrated according to the reference α-Fe absorber. The obtained spectra were fitted using a MossWinn 4.0 program package.

Thermal analysis (TG/DTG)

To study the thermal behaviour of the samples, the simultaneous thermogravimetric (TGA) and differential thermal analysis (DTA) were employed. The measurements were performed using a SDT Q-600 instrument (TA Instruments, New Castle, DE, USA). The samples were heated in opened standard alumina cups (90 µl) from room temperature to 800 °C at a heating rate of 10 °C min^{-1} under synthetic air with a flow rate of 100 cm^3 min^{-1}. The obtained results were evaluated with TA-Universal Analysis software.

X-ray photoelectron spectroscopy (XPS)

To analyse the surface chemistry of the CLI-modified samples, the XPS measurements were carried out on a PHI-TFA XPS spectrometer produced by Physical Electronics Inc and equipped with Al-monochromatic source. The analysed area was 0.4 mm in diameter and the analysed depth was about 3–5 nm. During data processing, the spectra were aligned by setting the C 1 s peak at 284.8 eV, characteristic for C–C/C–H bonds. Quantification of surface composition was performed from XPS peak intensities considering relative sensitivity factors provided by instrument manufacturer (Moulder et al., 1992). The sensitivity of the method is about 0.5 at.%. To analyse the obtained XPS spectra, the MultiPak software was used.

In order to analyse the in-depth distribution of elements in the sub-surface region up to 40 nm deep after the spent CLI regeneration, the XPS depth profiling was performed in combination with ion sputtering. The Ar ions with energy of 3 keV were used. The velocity of the ion sputtering was estimated to be 2.0 nm min^{-1} calibrated on the Ni/Cr multilayer structure of the known thickness. The high-resolution spectra of elements were obtained using the SPECS system under the UHV conditions with a chamber pressure in the range of 10–7 Pa. The instrument was equipped with the Phoibos MCD 100 electron analyser and the monochromatized X-ray source of 1486.74 eV (Al *Kα* line). High-resolution spectra were fitted with Gauss-Lorentz function and Shirley function was used to remove background.

N_2 adsorption/desorption analysis

The specific surface area and porosity characteristics were determined by the N_2 adsorption at –196 °C using a Micromeritics ASAP 2020 apparatus (Micromeritics Corporation, Norcross, GA, USA). Prior to the measurements, the samples were degassed at 150 °C for 10 h under a high vacuum. The specific surface area (S_{BET}) of samples was calculated using the Brunauer-Emmett-Teller (BET) method (Brunauer *et al*., 2002) from the linear part of the N_2 adsorption isotherm. The total pore volume (V_{tot}) was determined from the desorption isotherm at p/p_0= 0.998. The pore size distribution (PSD) was calculated by Barrett-Joyner-Halenda (BJH) method (Baugh *et al*., 1951), and the data was extrapolated from desorption isotherm branch. The average maximum pore diameter (D) was also determined from the BJH desorption analysis.

Fourier transform infrared spectroscopy (FTIR)

FTIR analysis was employed to study the structural features of the prepared composites. The FTIR measurements of CLI, MAG_{CP} and MAG_{CP}-CLI were performed at room temperature using a Digilab FTS-80 interferometer (Bio-Red, Cambridge, MA, USA) by applying the KBr pellets method, while the MAG_{MW}, MAG_{MW}-CLI and GO-MAG_{MW}-CLI samples were analysed on a Shimadzu IRSpirit (Shimadzu, Kyoto, Japan) instrument. The spectra were recorded in the range of 400 to 4000 cm^{-1}, at a resolution of 4 cm^{-1} and 100 scans.

Raman spectroscopy

Raman spectroscopy was used to detect the GO coated on CLI surface. Raman spectra was obtained by a confocal micro-Raman spectroscopy using a Horiba Jobin Yvone T64000 (Kyoto, Japan) equipped with a solid-state laser with the wavelength of 532.5 nm

and a 50x magnification large working distance objective in the range of 300–3500 cm^{-1}.

Zeta potential measurements

The zeta potentials of the samples were measured using a Zetasizer Nano ZS90 (Malvern Instruments Ltd., Malvern, UK) according to the method reported by Gulicovski *et al*. (Gulicovski *et al*., 2008). Briefly, 0.1 g of each sample was suspended in 50 cm^3 of deionized water and left at room temperature overnight. Then, the pH value of the suspension was adjusted in the range of 2 to 12 using a 0.1 mol dm^{-3} HCl or NaOH. Before each measurement, the suspensions were ultrasonically treated with an ultrasound probe for 30 s. The suspensions' pH values were adjusted using a Mettler Toledo (Columbus, OH, USA) digital pH meter.

Magnetic measurements

Magnetic properties of the magnetic samples were measured using a vibrating sample magnetometer Lake Shore 8607 Series VSM (LakeShore cryotronics, Westerville, OH, USA) at room temperature and with an applied magnetic field strength of 2.0 T.

UV-Visible spectroscopy (UV-Vis)

The concentration of CIP in the solution was determined by UV-Vis spectrophotometer, Perkin Elmer Lambda 365 (Perkin Elmer Inc., Waltham, MA, USA) at 278 nm using a standard pharmacological procedure (Naveed & Waheed, 2014). Before analysis, solutions were filtered through 0.22 μm nylon filter. All measurements were done in accordance with the Perkin Elmer manual recommendations.

The amount of the adsorbed CIP per unit of the adsorbent after time t (q_t) was calculated using the following formula:

$$q_t = \frac{(C_0 - C_e) \cdot V}{m} \tag{11}$$

where C_0 and C_e (mg dm^{-3}) are the initial CIP concentration and CIP concentration at equilibrium, respectively, V (dm^3) is the CIP solution volume, and m (g) is the adsorbent mass.

Optical emission spectroscopy (OES)

The optical emission spectroscopy (OES) of the surface dielectric barrier discharge in ambient air was performed to identify the excited species present in the plasma during treatment. The OES measurements were attained using Maya 2000 Pro spectrometer (Ocean Optics Inc, FL, USA). Emission from the plasma region was collected and directed towards an entrance slit of the spectrometer by using a collimating lens in the UV and Vis range (Ocean Optics UV74) and an optical fibre (Thorlabs, Newton, NJ, USA) with Ø200 μm core.

3.4. Regeneration studies

The regeneration experiments were performed by NTP treatment using a surface dielectric barrier discharge (SDBD) source operating in air. The procedure of spent adsorbents' regeneration test is schematically represented in Figure 11. The saturated adsorbent after the CIP adsorption (CLI-CIP, GO-CIP, GO-CLI-CIP, or GO-MAG_{MW}-CLI-CIP) was exposed to the NTP treatment and then used in repeated adsorption cycle under the same conditions as before to evaluate the efficiency of regeneration process.

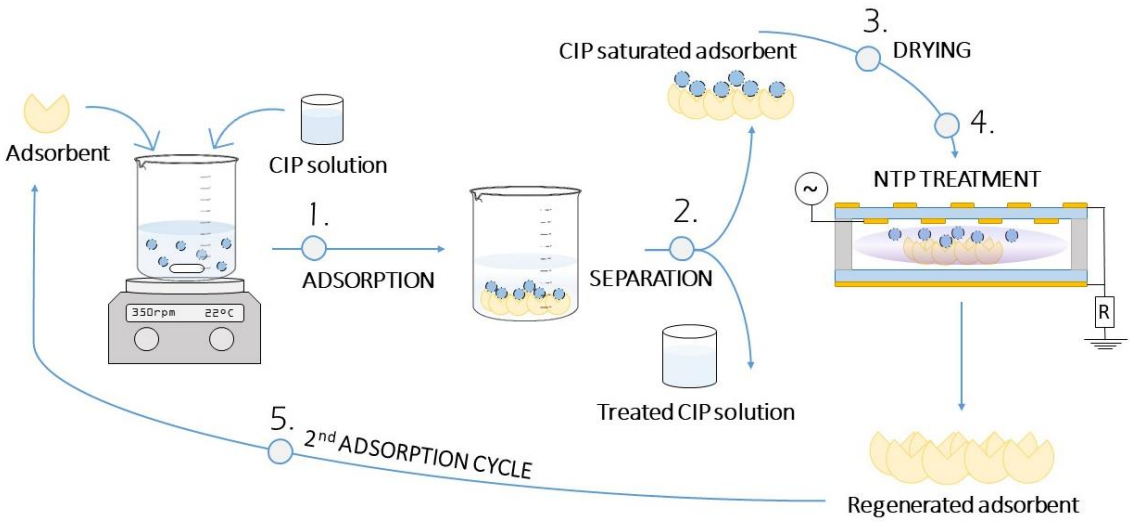

Figure 11. Schematic diagram of the CLI regeneration procedure.

SDBD source description

Plasma source was composed of two parallel dielectric barriers with electrodes – powered electrode facing the dielectric glass surface covering the grounded electrode. The copper tape strips were glued to both sides of a round-shaped upper glass plate of 2 mm thickness forming a square. Grid shaped electrodes from the lower side were powered while comb-shape electrodes from the upper side were grounded. The grounded stripe electrodes were positioned between powered electrode segments. The sample was put in a lower circular glass holder with side walls, which was standing on the grounded metal plate that served as a lower grounded electrode. Sine high-voltage (HV) signal of 50 Hz was supplied to the powered electrode. Amplitude of the high-voltage signal was regulated by a voltage regulator at input of the AC signal to the primary coil of the HV transformer. In the grounded line, a resistor of R = 15 kΩ was used to monitor the plasma current by measuring voltage drop on the resistor. Scheme of the electrical circuit and vertical cross section of the plasma source, as well as a photograph of the plasma source with a sample are shown in Figure 12.

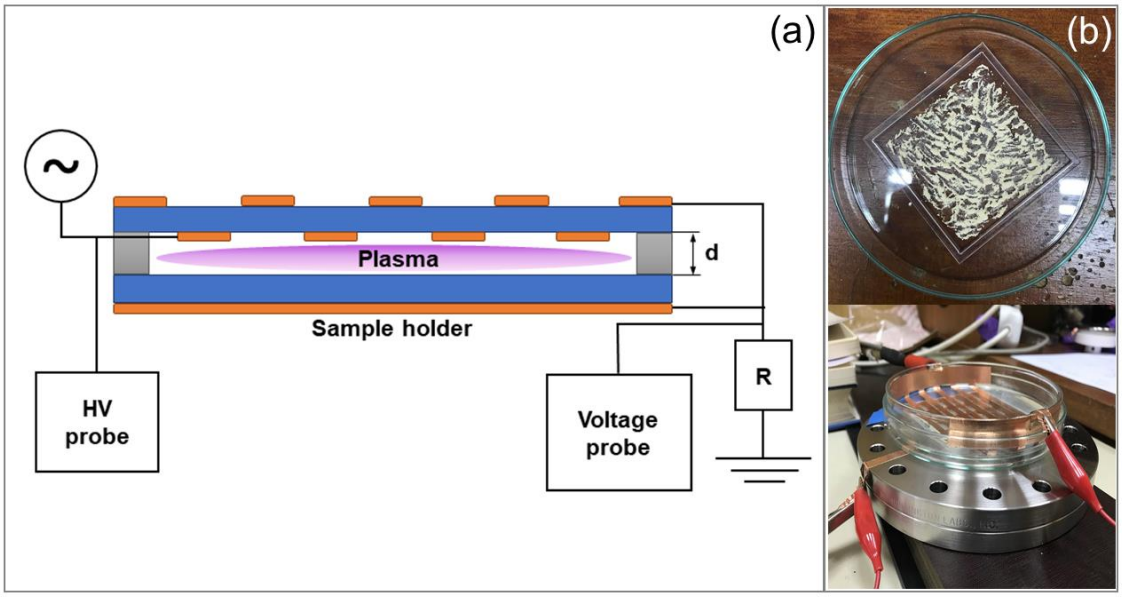

Figure 12. (a) Scheme of the plasma SDBD source, and (b) image of the sample layer on the glass barrier and the used SDBD plasma source with the CLI-CIP sample.

The application of NTP in this study includes the following:

- A preliminary optimization of the plasma treatment process,
- The regeneration treatments of spent adsorbents.

Two different concentrations of CIP solution were used in the adsorption experiments related to the adsorbents' regeneration studies. For preliminary optimization of the plasma treatment process, a solution of 200 mg dm^{-3} (*adsorbent*-CIP^{200}) was used. For the reusability tests, together with a solution of 200 mg dm^{-3}, a CIP solution of 25 mg dm^{-3} was used for the reusability test of spent CLI (CLI-CIP^{25}) only, since it is more of a realistic concentration that could be found in natural waters and wastewaters.

Optimization of the SDBD key operating parameters

Before the regeneration experiments, a range of operational parameters was investigated in order to determine the optimal ones for the efficient adsorbents' regeneration after the antibiotic adsorption. For this purpose, only the samples CLI-CIP^{200} with 14.7 mg of CIP per g was used. CLI- CIP^{200} was treated with the SDBD source of 18.1 cm^2 electrode surface (*S*). The treated sample mass (*m*) and distance between electrodes (*d*) were varied. Three investigated combinations of the parameters together with the associated plasma system powers are given in Table 4. Plasma treatment time was 20 min with maximum available voltage at the power supply. The treatment duration was selected as the longest possible considering the type of treatment as well as prior experience. The efficiency of the regeneration treatment was measured in loss of the adsorption efficiency (LAE) which was calculated as a difference in CIP removal efficiency in the first and second adsorption cycle, after NTP treatment.

Table 4. Parameters of the plasma treatment system for the regeneration process optimization.

Parameters/Configuration	Sample	Plasma			
	m^a (g)	d^b (mm)	$V_{RMS}{}^c$ (kV)	$I_{RMS}{}^d$ (mA)	$P_{mean}{}^e$ (W)
1	0.25	4	8.33	0.24	1.14
2	0.10	4	8.33	0.24	1.14
3	0.10	2	8.33	0.30	1.30

Treatment time: 20 min.
[a]CLI-CIP^{200}sample mass; [b]plasma discharge gap; [c]plasma discharger voltage; [d]plasma discharge current; [e]applied system power.

After determination of the optimal conditions, the experiments were repeated using the source with the larger electrode surface of 37.2 cm^2 to investigate the possibility of system scale-up. Zero point two gram of CLI-CIP^{200} was exposed to the plasma for 20 min. The applied voltage was V_p = 23 kV (peak-to-peak), i.e. V_{RMS} = 8 kV and I_{RMS} = 0.30 mA, and the distance between electrodes was 2 mm. The mean power was calculated at several instances during each treatment and the value of 2.50 ± 0.06 W was obtained. The efficiency of the enlarged plasma source was also evaluated by calculating the LAE parameter.

Regeneration tests of spent adsorbents

For the plasma regeneration experiments, the CLI-CIP^{25} or CLI-CIP^{200}, GO-CIP^{200}, GO-CLI-CIP^{200} and GO-MAG$_{MW}$-CLI-CIP^{200} samples with 2.3 or 14.7, 40.5, 17.9 and 20.0 mg CIP per g of adsorbent, respectively, were exposed to NTP using SDBD source with the electrode surface of 37.2 cm^2 for 20 min. The distance between the electrodes was 2 mm, and the treated sample mass was 0.20 g.

Before each treatment, mass of each sample was determined on a precise scale and then homogeneously spread on the glass holder in a very thin layer (less than 1 mm of thickness) to cover entire square formed by the upper electrode. After plasma ignition, due to charging of the powder, it was drifting in electric field and conglomerating at certain points under the electrode grid. The square-shaped electrode spacer was surrounding the active plasma zone. Limiting the sample from drifting outside. After each treatment, very small amount of the sample was lost in manipulation so weighting at a precise scale was performed again before the adsorption step.

In order to determine the gas temperature inside the active plasma volume during the sample treatment, and optical temperature sensor (opSense, OTG series) placed inside the investigated volume was used.

Power measurement

Electric parameters were measured and recorded by a digital oscilloscope KEYSIGHT (InfiniiVision DSOX 1024A, USA), a high-voltage (HV) probe (P6015A, Tektronix Inc., Beaverton, OR, USA) and a voltage probe (N2863B, Agilent, Santa Clara, CA, USA). The voltage probe measured the voltage drop, allowing calculation of the current passing through the discharge and to the ground. The instantaneous power $P(t)$ was calculated from the obtained waveforms of voltage and current, considering correction of the current signal for the displacement current. The mean power was then calculated by averaging $P(t)$ function for several signal periods. This setup allowed to monitor the stability of

plasma during the treatment, the changes in the plasma with changing the treatment parameters and consequently to perform the optimization of the parameters.

Regeneration experiments

To evaluate the efficiency of regeneration process, the five successive adsorption-regeneration cycles were performed for the CLI, GO, GO-CLI and GO-MAG_{MW}-CLI adsorbents. The CIP adsorption experiments were performed by batch method.

For the first adsorption cycle, an adsorbent was suspended in the CIP solution (C_0 = 200 mg dm^{-3}, pH = 5) in a glass beaker with a solid to liquid ratio of 1:100. Therefore, the adsorbent mass for the first adsorption cycle was 1.5 g for 150 ml of CIP solution. The mass loss per regeneration cycle was considered when calculating subsequent masses so that the abovementioned ratio of 1:100 was maintained. The suspension was put to stir on a magnetic stirrer at 23 ± 1 °C for 60 min. Regenerated adsorbent was used in the next adsorption cycle under the same experimental conditions as before.

To investigate the reusability of adsorbent with lower CIP loading, the CIP solution of 25 mg dm^{-3} was also used for the reusability test of CLI-CIP^{25} (2.3 mg CIP g^{-1}) through five adsorption-regeneration cycles. The adsorption experiments were performed under mostly the same conditions as before, but for shorter adsorption time of 5 min.

After the adsorption experiments, adsorbent was separated from the liquid phase by vacuum filtration and then air-dried for around 2h at room temperature. The CIP concentration in filtrate was determined by the UV-Vis method and the CIP uptake (q_t) by the system was calculated using the same Equation (11) mentioned above.

4. RESULTS AND DISCUSSION

4.1. Characterization

Zeolitic tuff

Mineral composition of the zeolitic tuff was determined by PXRD analysis. The obtained PXRD diffraction pattern is presented in Figure 13, and it shows that clinoptilolite is the major mineral phase in zeolitic tuff. The diffraction peaks at 2θ = 9.79°, 11.16°, 13.06°, 16.89°, 19.00°, 22.31°, 25.01°, 25.98°, 29.90°, 31.84° and 32.68° correspond to the clinoptilolite (Hawash *et al.*, 2018). The PXRD pattern also shows that tuff contains a slight amount of quartz (2θ = 26.6°) and feldspar (2θ = 27.1°) (Hawash *et al.*, 2018; Rajic *et al.*, 2011).

The quantitative analysis performed using Rietveld refinements (Coelho, 2007) showed that tuff had high content of clinoptilolite (>80 wt.%), with quartz (<7.5 wt.%) and feldspar (<13 wt.%) as major satellite phases.

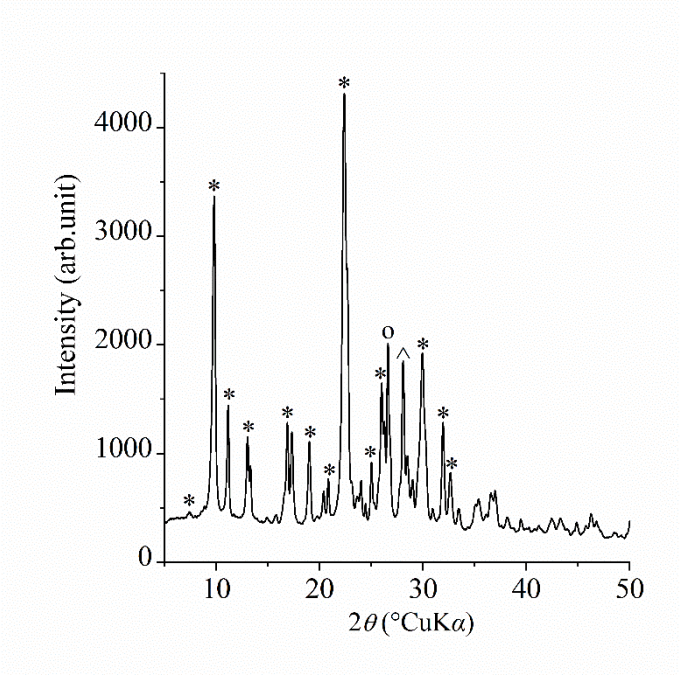

Figure 13. PXRD pattern of the zeolitic tuff (*clinoptilolite; °quartz and ^feldspar).

The concentration of exchangeable cation and CEC value are given in Table 5. It is evident that concentration of Na is lowest in comparison to other present cations.

Table 5. Cation exchange capacity (CEC) of the used zeolitic tuff.

Sample/Cation	**Na^+**	**K^+**	**Ca^{2+}**	**Mg^{2+}**	**∑**
	Concentration (mmol M^+/100 g)				
CLI	3.6	10.4	57.5	16.6	162.2

Modified CLI samples

PXRD patterns of MAG_{CP}-CLI, MAG_{MW}-CLI, and GO-MAG_{MW}-CLI are shown in Figure 14. The results showed that the crystallinity of the CLI lattice remained preserved after the modifications. All diffractions characteristic for the clinoptilolite lattice can be seen in all patterns.

A new diffraction peaks which appeared in the patterns of MAG_{CP}-CLI, MAG_{MW}-CLI and GO-MAG_{MW}-CLI at 2θ = 35.58°, 43.27°, 57.34° and 62.97° suggest the presence of new phase corresponds to iron oxide with a cubic crystal cell unit (Kouli *et al.*, 2018; Rajput *et al.*, 2016). According to the literature data, the peaks can be assigned to either magnetite (Fe_3O_4) or maghemite (γ-Fe_2O_3) particles.

Since Fe_3O_4 and γ-Fe_2O_3 have similar cubic spinel crystal structures and almost identical lattice parameters, it is difficult to distinguish them from one another based only on the diffraction positions (Kim *et al.*, 2012). Thus, the quantitative analysis of the obtained XRD peaks of pure MAG_{MW} and MAG_{MW}-CLI was performed by the reference intensity ratio (RIR) method (Figure 15). Table 6 provides the obtained RIR results, which indicate that novel phase consists of different crystalline phases. In pure MAG_{MW}, dominant phase is γ-Fe_2O_3 whereas Fe_3O_4 is present at only 10 wt.%. Additionally, in the MW-assisted synthesis of Fe_3O_4, goethite formed as a satellite phase. Goethite is weakly magnetic, so its presence in the MAG_{MW} sample could affect the MAG_{MW} magnetic properties (Awwad *et al.*, 2022). On the other hand, in the MW-assisted synthesis of MAG_{MW}-CLI, γ-Fe_2O_3 was the only phase formed on the CLI surface. This should be explained by the fact that Fe_3O_4 crystallized firstly and then was gradually converted to γ-Fe_2O_3 after exposure to air (Salem Attia *et al.*, 2014).

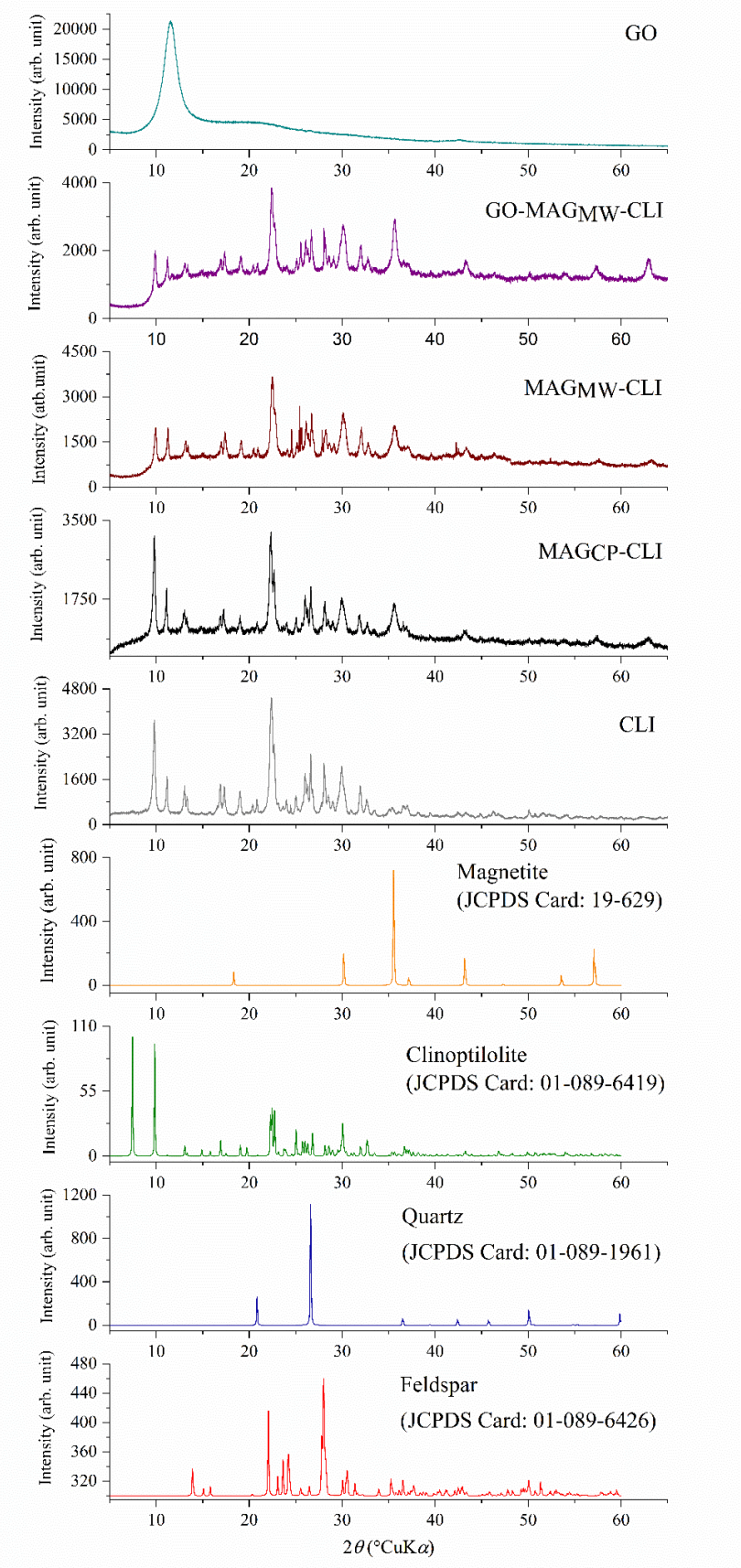

Figure 14. PXRD patterns of CLI, CLI-modified samples and GO.

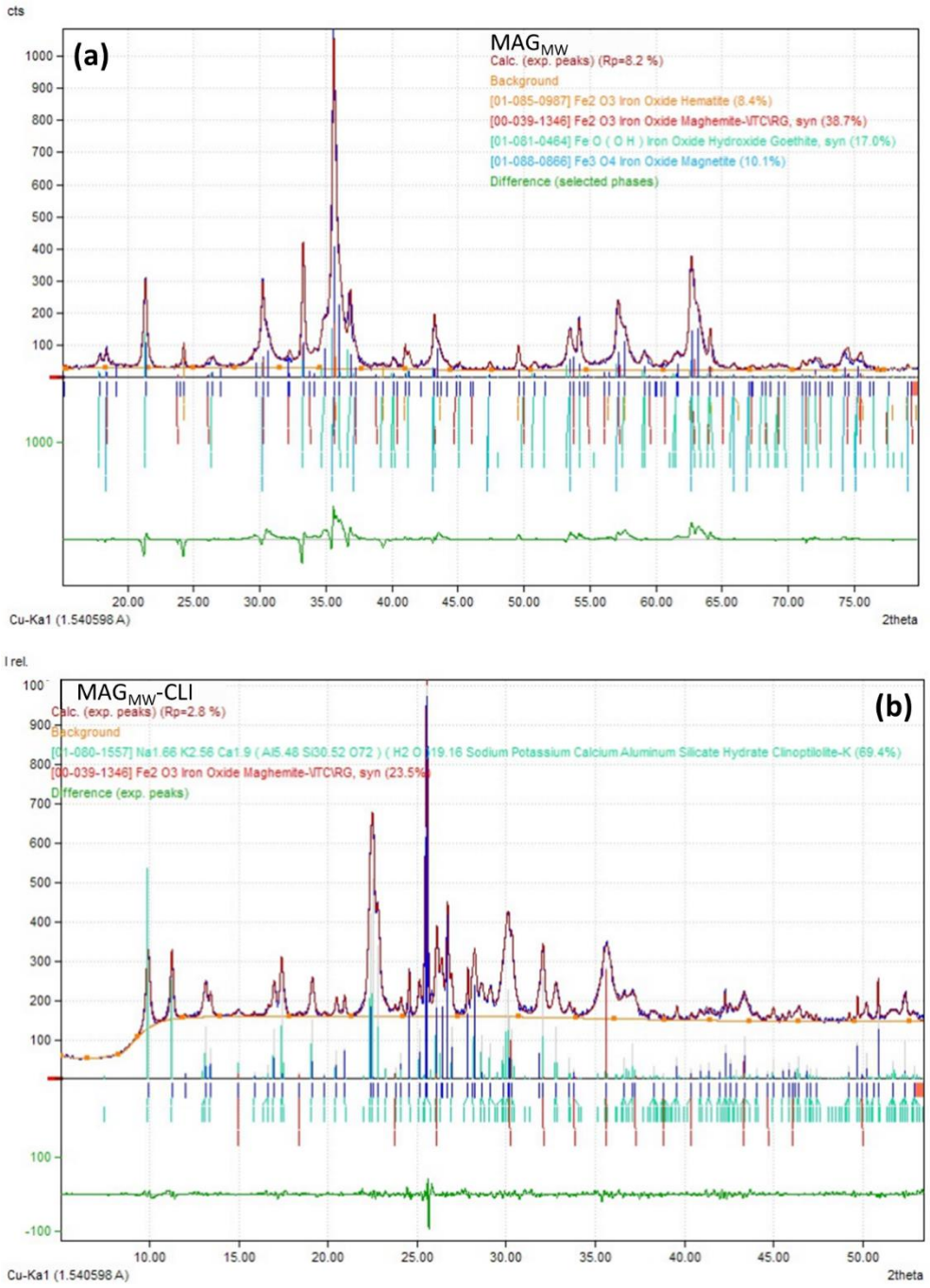

Figure 15. PXRD diffractograms of (a) MAG_{MW} (b) and MAG_{MW}-CLI used for the RIR analysis.

The diffraction peak at 2θ = 11.50° in GO diffraction pattern is attributed to the GO layered structure (Figure 14) (Krishnamoorthy *et al.*, 2013). This peak cannot be seen in the pattern of GO-MAG_{MW}-CLI due to the overlapping with the CLI diffractions, as well as due to a low amount of GO.

Table 6. The phase analysis of MAG_{MW} and MAG_{MW}-CLI samples obtained by quantitative XRD analysis using the RIR method.

Phase	Amount (wt.%)
MAG_{MW}	
Maghemite (γ-Fe_2O_3)	38.7
Goethite (FeO(OH))	17.0
Magnetite (Fe_3O_4)	10.1
Hematite (α-Fe_2O_3)	8.4
MAG_{MW}-CLI	
Clinoptilolite (CLI)	69.4
Maghemite (γ-Fe_2O_3)	23.5

Influence of different particle size, preferred orientation, line overlapping, crystal symmetry etc. explained that about 26% of diffractions in the pattern of MAG_{MW} (Figure 15a) was unidentified.

The surface morphology of the prepared samples was analysed by TEM. According to the TEM images (Figure 16), the MAG_{CP} sample is composed of fine dispersed nanosized magnetite (Fe_3O_4) particles. The Fe_3O_4 particles sizes range between 5–30 nm, with few exceeding 100 nm at the top of the cluster (Figure 16a). Ring diffraction patterns obtained by selected area electron diffraction (SAED) pattern are typical of spinel structure with most intense ring of {311} reflections in randomly oriented nanocrystals. Fe_3O_4 nanoparticles shows characteristic octahedral morphology with many crystals connected by {111} spinel-twin that forms through self-assembly as shown by Rečnik *et al.* (Rečnik *et al*., 2013). SAED pattern of the cluster is shown as inset in the bottom-left corner of Figure 16a. Furthermore, the synthesis of Fe_3O_4 nanoparticles by MW-assisted method was accompanied by the goethite (α-FeO(OH)) formation which is in accordance with the results obtained by the PXRD. MAG_{MW} contains clusters of several hundred nanometres long goethite needles covered by a fine fraction of magnetite crystals (Figure 16b).

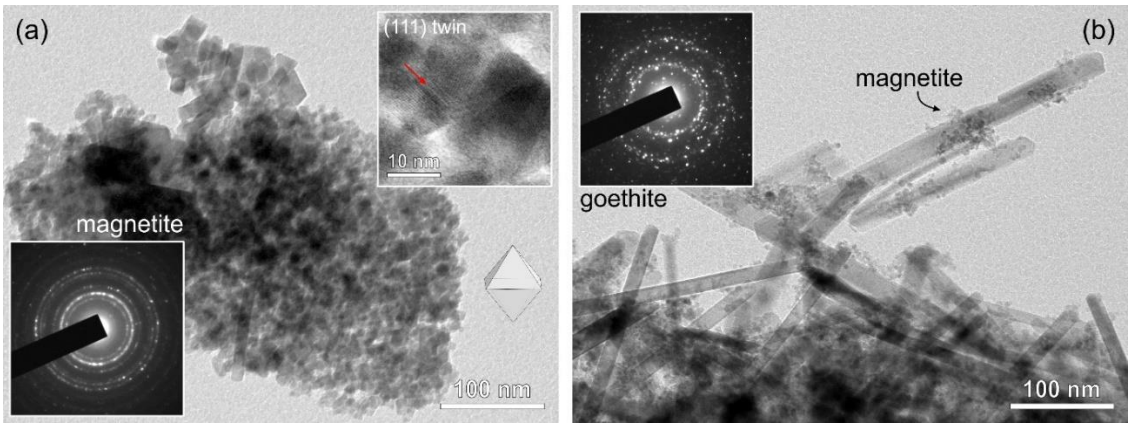

Figure 16. TEM images of (a) the MAG_{CP}, and (b) MAG_{MW} samples.

CLI treated by standard co-precipitation method (MAG_{CP}-CLI) shows abundant coverage with magnetite nanocrystals (Figure 17a). The extensive morphological degradation of CLI sheet densely covered by rounded Fe_3O_4 nanocrystals was observed. The formed

Fe_3O_4 crystals have globular morphology. On the other hand, Figure 17b shows euhedral CLI sheets covered by fine grained Fe_3O_4 crystals. CLI crystals in MAG_{MW}-CLI are less degraded whereas Fe_3O_4 crystal retains their octahedral shape. SAED shows interrupted ring patterns that are indicative of nanocrystal ordering. Intensity peaks with six-fold symmetry can be seen for {111} and {311} Fe_3O_4 reflections.

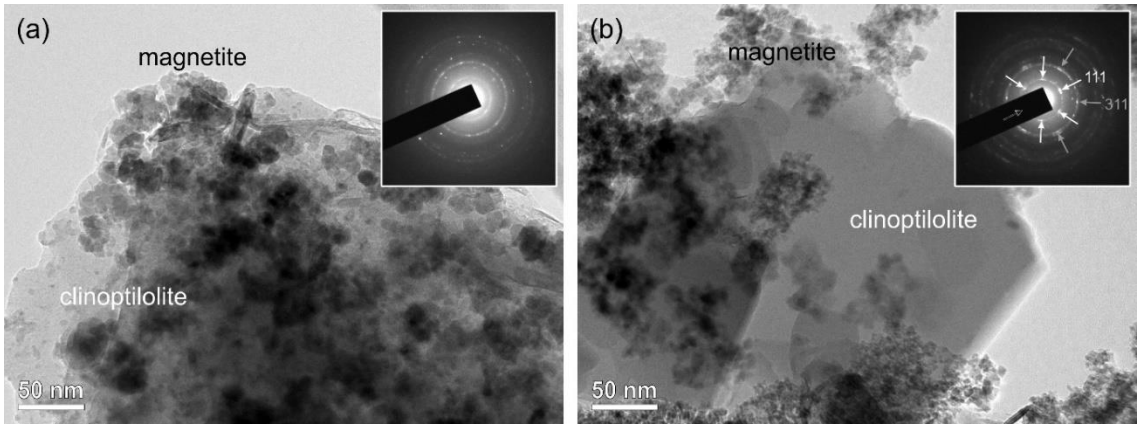

Figure 17. TEM images of (a) MAG_{CP}-CLI, and (b) MAG_{MW}-CLI samples.

Furthermore, the surface morphology of pristine CLI, MAG_{MW}-CLI and GO-MAG_{MW}-CLI samples was studied by FE-SEM, and the results are shown in Figure 18. As can be observed in Figure 18b, the formation of MAG_{MW} particles (with estimated particle sizes ranging from 20 to 40 nm) on the CLI surface did not alter the CLI's structure. Additionally, the co-precipitation of spherical magnetic nanoparticles on the CLI surface caused particle agglomeration, which can be attributed to the high surface energy of smaller particles attracting other particles (Wang *et al*., 2016). This phenomenon has also been reported for the synthesis of Fe_3O_4-coated CLI using the standard co-precipitation method (Javanbakht *et al*., 2016). The coating of GO (Figure 18c) did not significantly impact the surface morphology of CLI. However, the GO sheets in GO-MAG_{MW}-CLI were not visible which was ascribed to the broken GO layers and/or low GO content.

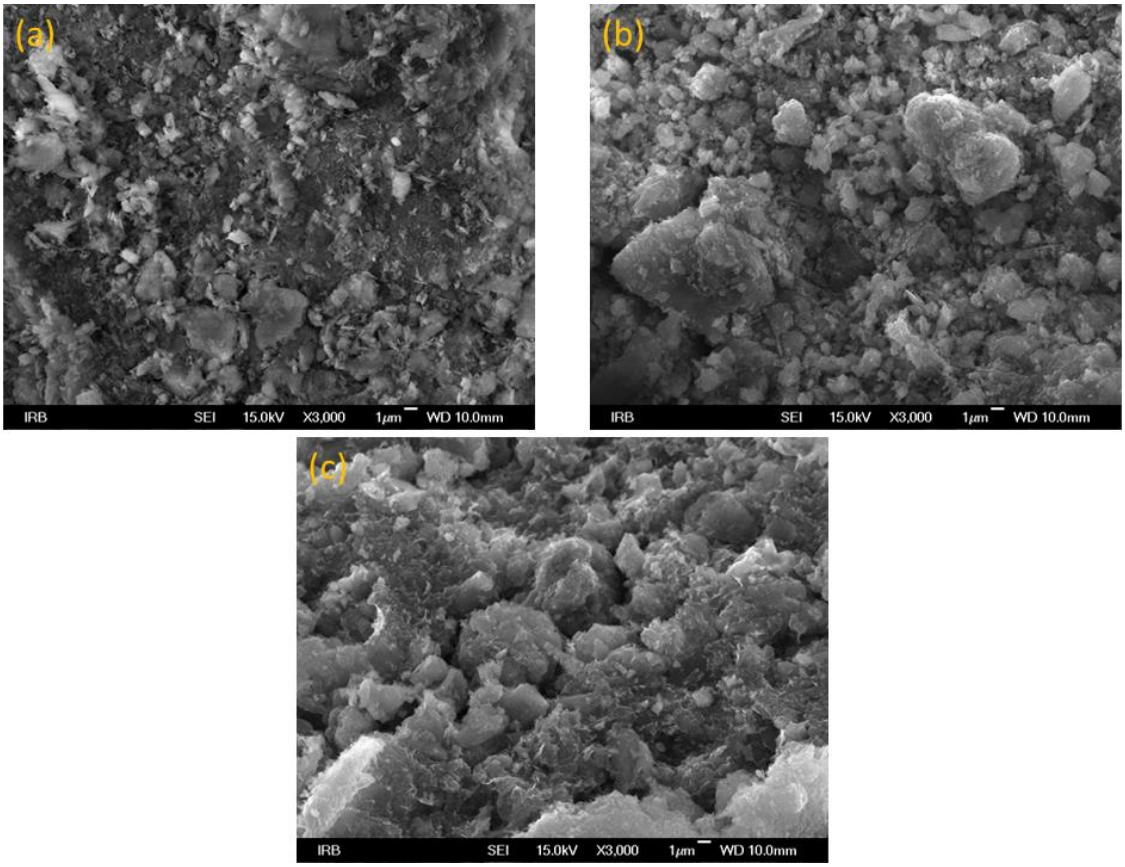

Figure 18. FE-SEM images of (a) CLI, (b) MAG_{MW}-CLI and (c) GO-MAG_{MW}-CLI.

The average chemical composition of CLI and CLI-based composites determined by the EDS analysis are summarized in Table 7. The results indicate that the zeolite phase composed of the Ca-rich clinoptilolite with Si/Al molar ratio of 5.03. The molar ratio changed by modification and the most notable increase of 6.12 was observed for MAG_{CP}-CLI. This indicates a partial dealumination of CLI during the modification.

The content of exchangeable cations (Ca and K) decreased in MAG_{CP}-CLI, MAG_{MW}-CLI, and GO-MAG_{MW}-CLI samples, while the content of Fe increased. Since the Fe content increase is significantly higher than the decrease in content of exchangeable cations, it can be concluded that the modification of CLI by Fe(III) proceeds through an ion-exchange and precipitation of the Fe species on the CLI surface. This phenomenon is similar to that reported for loading of different metal oxide species onto CLI (Jevtić *et al.*, 2014; Kragović *et al.*, 2013). Moreover, EDS shows that the content of magnetite in MAG_{CP}-CLI and MAG_{MW}-CLI is approximately 12 wt.%, while carbon content (9.94 wt.%) can be assigned to GO coating.

Table 7. The average chemical composition of the CLI phase of CLI, MAG_{CP}-CLI, MAG_{MW}-CLI and GO-MAG_{MW}-CLI obtained by EDS analysis.

Sample/Element	Si	Al	O	K	Ca	Fe	C	Si/Al
	at.%							
CLI	18.35	3.65	75.97	0.44	1.20	0.40	–	5.03
MAG_{CP}-CLI	18.39	3.01	72.15	0.27	0.18	5.63	–	6.12
MAG_{MW}-CLI	20.19	3.98	68.15	0.33	0.51	6.84	–	5.07
GO-MAG_{MW}-CLI	12.65	2.45	62.53	0.35	0.83	4.54	16.65	5.16

To determine the magnetic iron oxide phases in MAG_{MW} and MAG_{MW}-CLI the Mössbauer spectroscopy was used since this analysis enables different Fe valence states to be distinguished. The ^{57}Fe Mössbauer spectra of pure MAG_{MW} and MAG_{MW}-CLI samples recorded at room temperature are shown in Figure 19, and the calculated Mössbauer parameters and phase identification are given in Tables 8 and 9.

Table 8. Mössbauer parameters for the MAG_{MW} nanoparticles.

MAG_{MW}					
Component	**δ^a (mm s^{-1})**	**$\Delta E_Q{}^b$ (mm s^{-1})**	**$B_{hf}{}^c$ (T)**	**Area (%)**	**Phase**
Sextet	0.37	−0.20	51.53	9.5	α-Fe_2O_3
Sextet	0.37	−0.26	38.01	14.6	α-FeOOH
Sextet	0.69	0.06	46.19	6.6	Fe_3O_4 octahedral
	0.25	–0.04	48.69	5.2	Fe_3O_4 tetrahedral
Sextet	0.33	0.00	29.71*	64.0	γ-Fe_2O_3

[a]Isomer shift relative to α–Fe; [b]quadrupole splitting; [c]hyperfine magnetic field.

Table 9. Mössbauer parameters for the MAG_{MW}-CLI sample.

MAG_{MW}-CLI					
Component	**δ^a (mm s^{-1})**	**$\Delta E_Q{}^b$ (mm s^{-1})**	**$B_{hf}{}^c$ (T)**	**Area (%)**	**Assignation**
Sextet	0.36	−0.03	36.99*	68.6	γ-Fe_2O_3
Doublet	0.34	0.66	–	31.4	γ-Fe_2O_3 superparamagnetic

[a]Isomer shift relative to α−Fe; [b]quadrupole splitting; [c]hyperfine magnetic field.

The Mössbauer spectrum of magnetic iron oxide nanoparticles depends on the structural properties and the particle size influenced by synthesis procedure (Marciuš *et al.*, 2021). Dominant iron oxide phase in both MAG_{MW} and MAG_{MW}-CLI is γ-Fe_2O_3 which is in accordance with PXRD analysis. The spectrum of MAG_{MW} (Figure 19a) was fitted as a superposition of four sextets. The prominent central doublet observed in the MAG_{MW} spectrum is a result of fast superparamagnetic relaxation of smaller crystal domains of γ-Fe_2O_3 phase present in the sample. A wide sextet pattern characterized by distribution of the hyperfine field (B_{hf}) could be attributed to a broad range of crystal domains size of the γ-Fe_2O_3, which are above the superparamagnetic relaxation threshold (Joos *et al.*, 2016). The rest of the spectrum originates from the larger particles and shows insufficient hyperfine splitting to accurately identify the mixed-valence Fe sextet.

The formation of γ-Fe_2O_3 is usually accompanied with Fe_3O_4 crystallization due to the slow magnetite oxidation by air oxygen (Schwaminger *et al.*, 2017). This results in presence of the γ-Fe_2O_3 layer on the surface. The significance of this effect is magnified in nanoscale materials due to their increased surface area, allowing it to be observed even in individual crystals. Moreover, the starting reaction mixture and the mechanism of the MW-assisted synthesis enables the formation of multiple iron oxide phases (Kozakova *et al.*, 2015). The reaction probably starts with the formation of iron hydroxide according to the reactions (3) and (4) (Kozakova *et al.*, 2015). The presence of both Fe(II) and Fe(III) enables the magnetite formation (reaction (5)), while the γ-Fe_2O_3 can be formed according to the reaction (6). The presence of goethite as minor phase can be explained by partial dehydration of $Fe(OH)_3$ (reaction (7)). This sequence of several reaction steps can be explained by the fast nucleation in aqueous system, quick formation of particles in the reaction mixture as well as the very short crystallization time (Kozakova *et al.*, 2015).

$$Fe^{3+} + 3OH^- \leftrightarrow Fe(OH)_3 \quad (3)$$

$$Fe^{2+} + 2OH^- \leftrightarrow Fe(OH)_2 \quad (4)$$

$$2Fe(OH)_3 + Fe(OH)_2 \leftrightarrow Fe_3O_4 + 4H_2O \quad (5)$$

$$2Fe(OH)_3 \leftrightarrow Fe_2O_3 + 3H_2O \quad (6)$$

$$Fe(OH)_3 \leftrightarrow FeO(OH) + H_2O \quad (7)$$

However, the coating of iron oxide nanoparticles on CLI resulted in the formation of only γ-Fe_2O_3 in two magnetic states. The primary component of the MAG_{MW}-CLI spectrum corresponds to a sextet, indicating that these particles are larger than 20 nm and magnetic, while smaller particles in the superparamagnetic state below 10 nm corresponds to a spectral doublet. When the CLI is present in the reaction mixture, the pH value is influenced not only by the quantity of added base, but also by the interactions of the CLI surface functional groups with H^+ (at pH< pH_{PZC}[6]) or by OH^- (at pH> pH_{PZC}) ions from the solution. This can change the OH concentration in the suspension and affects the reaction pathways (Ahribesh *et al.*, 2017).

Taking into consideration reported studies on the influence of ultrasound irradiation on the physico-chemical properties of iron oxide particles (Gahrouei *et al.*, 2020; Saber Braim *et al.*, 2022), the sonication conditions applied in GO-MAG_{MW}-CLI synthesis should not affect the magnetic properties of iron oxide particles. Therefore, it is assumed that the iron oxide phases present in MAG_{MW}-CLI remained unchanged after the GO coating.

[6] PZC – point of zero charge; pH_{PZC} – pH value when the adsorbent's surface charge is zero.

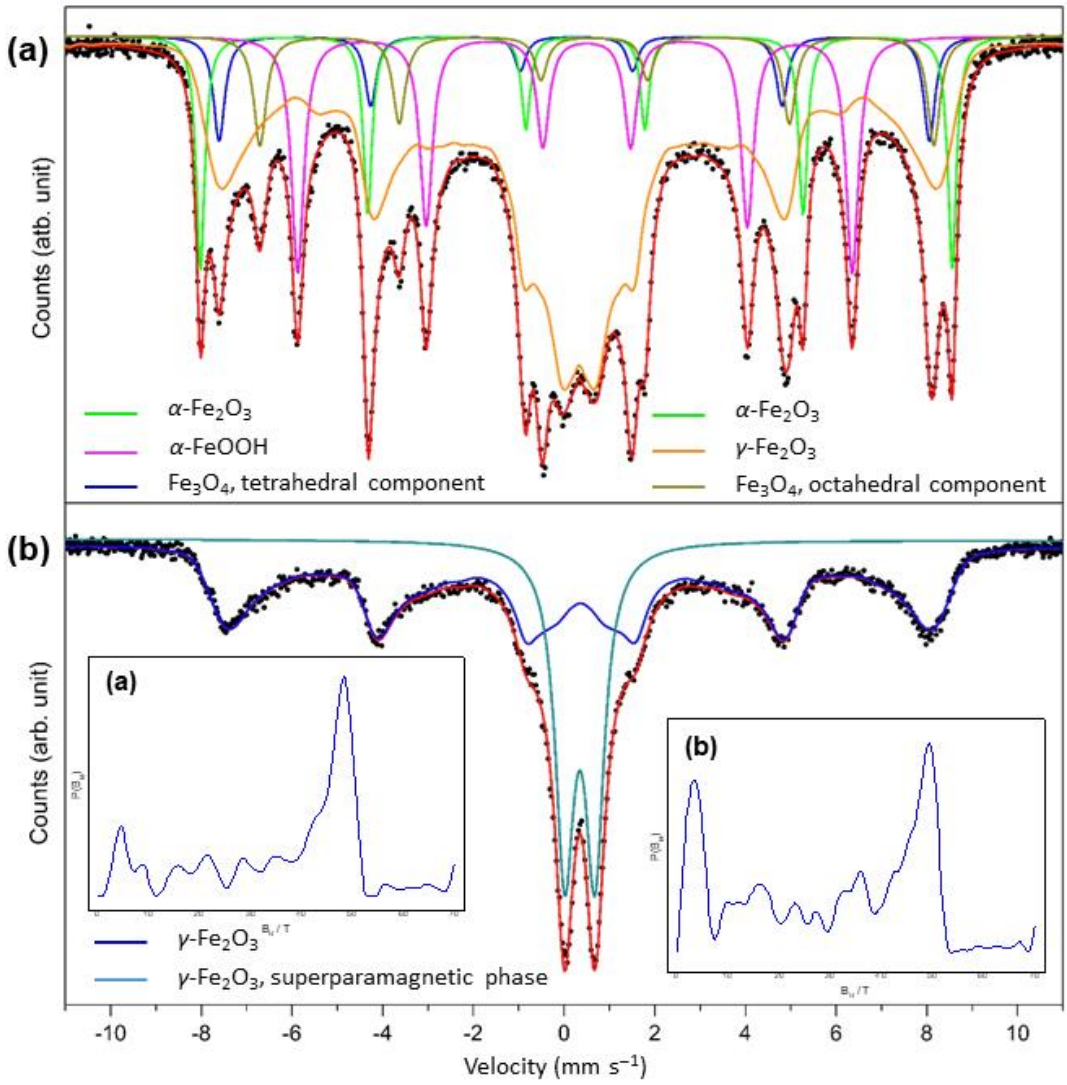

Figure 19. ^{57}Fe Mössbauer spectra of (a) MAG_{MW} and (b) MAG_{MW}-CLI samples recorded at room temperature (• stands for experimentally obtained data). The insets show the B_{hf} distribution.

Generally, formation of pure Fe_3O_4 by co-precipitation requires prevention of favorable Fe(II) oxidation and enough OH^- for co-precipitation reaction. In the case of two studied synthesis procedures, inert atmosphere could affect the formation of different iron oxide phases. Namely, during the synthesis of MAG_{CP} and MAG_{CP}-CLI, a constant N_2 bubbling provided prevents oxidation, which was omitted in MW-assisted procedure due to the technical feasibility. In both methods, pH was adjusted (Ahribesh *et al.*, 2017) enabling similar concentration of OH^- ions.

MAG_{MW}-CLI and GO-MAG_{MW}-CLI were further characterized by XPS analysis in order to get a better insight into their surface properties. The peaks of elements Si, Al, O, Ca, and K originating from the CLI matrix are present in all three spectra. Additionally, C 1s peak visible in the spectra of CLI and MAG_{MW}-CLI (Figure 12a,c) was the result of contamination layer due to sample handling in air. The binding energy of C 1s found in all three spectra is 285.1 eV, which can be assigned to C–C and C–H bonds (Tam *et al.*,

2019), indicating that the carbon does not originate from carbonate species often present in the zeolitic tuff.

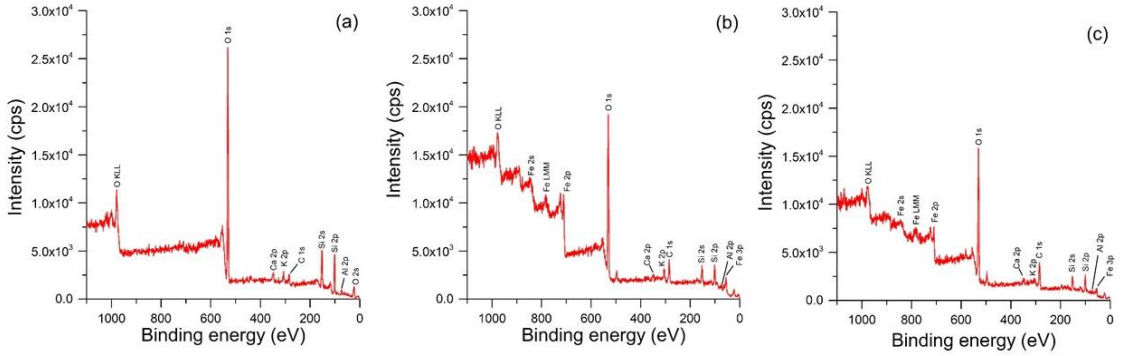

Figure 20. XPS survey spectra from the surface of (a) CLI, (b) MAG_{MW}-CLI, and (c) GO-MAG_{MW}-CLI.

In Figure 21, the high-resolution spectra of Fe 2p and C 1s regions obtained by XPS measurements for MAG_{MW}-CLI and GO-MAG_{MW}-CLI, respectively, are shown. The results in Figure 21a indicate that the iron is present in the Fe^{3+} oxidative state (Lu *et al.*, 2015; F. Wang *et al.*, 2016). This is in accordance with the obtained results for the Mössbauer spectroscopy. The deconvoluted C 1s peaks in Figure 21b show peak binding energies of 284.8, 286.2, 288.2, and 290.1 eV, which correspond to C–C, carbonyl (C–O), carboxyl (C=O), and O–C=O bonds, respectively, which indicate the presence of oxidized graphene sheets (Johra *et al.*, 2014).

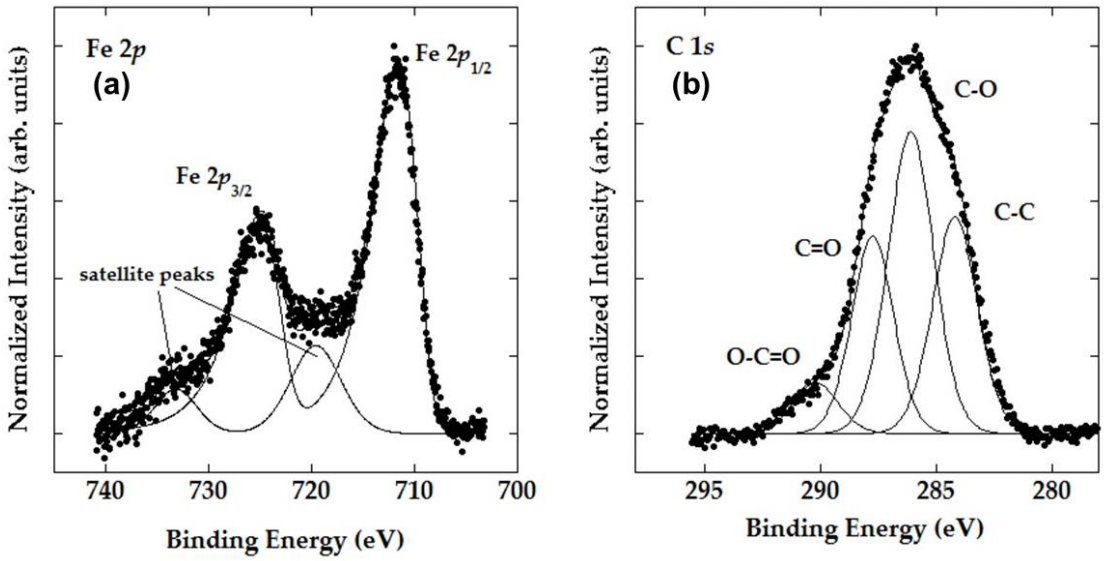

Figure 21. High-resolution XPS spectra of (a) Fe 2p region of MAG_{MW}-CLI, and (b) of C 1s region of GO-MAG_{MW}-CLI.

Table 10 gives the relative elemental composition of CLI and the synthetized composites, which was determined based on the studied elements' XPS peak intensities. The results are consistent with those obtained by the EDS, suggesting the combined mechanism of

ion-exchange and Fe species precipitation on the CLI's surface during CLI transformation to MAG_{MW}-CLI.

Table 10. The relative content of elements (at.%) in CLI, MAG_{MW}-CLI and GO-MAG_{MW}-CLI determined by the XPS analysis.

Element	CLI	MAG_{MW}-CLI	GO-MAG_{MW}-CLI
		at.%	
O	60.6	60.0	48.8
C	4.7	18.5	27.2
Fe	–	5.7	4.2
Si	26.8	18.5	16.3
Al	5.4	3.9	2.2
Ca	1.6	1.8	0.9
K	0.9	0.6	0.4

Thermal analysis (TA) was performed to study the formation of Fe oxide phases during heating. The obtained TG curves of CLI, MAG_{CP}-CLI, MAG_{MW}-CLI and GO-MAG_{MW}-CLI are given in Figure 22. All curves display similar continual weight loss of 5–10 wt.% up to 300 °C, which is attributed to the loss of the water located mostly in the CLI cavities (Alver *et al.*, 2010). At higher temperatures, the weight loss of synthetized composites differs from that of pristine CLI.

CLI lost weight continuously up to 800 °C, whereas the weight loss of MAG_{CP}-CLI and MAG_{MW}-CLI took place in two stages – from 300 to 500 °C and from 500 to 800 °C. The total weight losses were rather similar (wt.%: 14.2–CLI, 13.1–MAG_{CP}-CLI, 11.3–MAG_{MW}-CLI and 12.0–GO-MAG_{MW}-CLI). The weight losses on the DTG curve of CLI are accompanied by the weak DTG maxima at 58 (wt. loss of about 5.5%), 160 (wt. loss of about 4.7%) and 600 °C (wt. loss of about 4.0%), suggesting a release of water molecules from different crystallographic sites. DTG curves of MAG_{CP}-CLI and MAG_{MW}-CLI exhibit a strong maximum at 470 °C (wt. loss of about 7.1%), indicating a possible conversion of magnetite to maghemite (γ-Fe_2O_3) (Salem Attia *et al.*, 2014).

In the sample with GO, decomposition of unstable oxygen groups occurs at lower temperatures – below 200 °C, which is overlapping with the water loss from the CLI surface. At around 200 °C a small exothermic peak is observed. The weight loss in this region corresponds to the decomposition caused by elimination of more stable oxygen functional groups present in GO structure. Third step of a weight loss in the DTG curve of GO-MAG_{MW}-CLI occurs in a temperature range from 400 to 500 °C, which can be attributed to the combustion of the GO carbon skeleton (Hidayat *et al.*, 2020; Morais *et al.*, 2015).

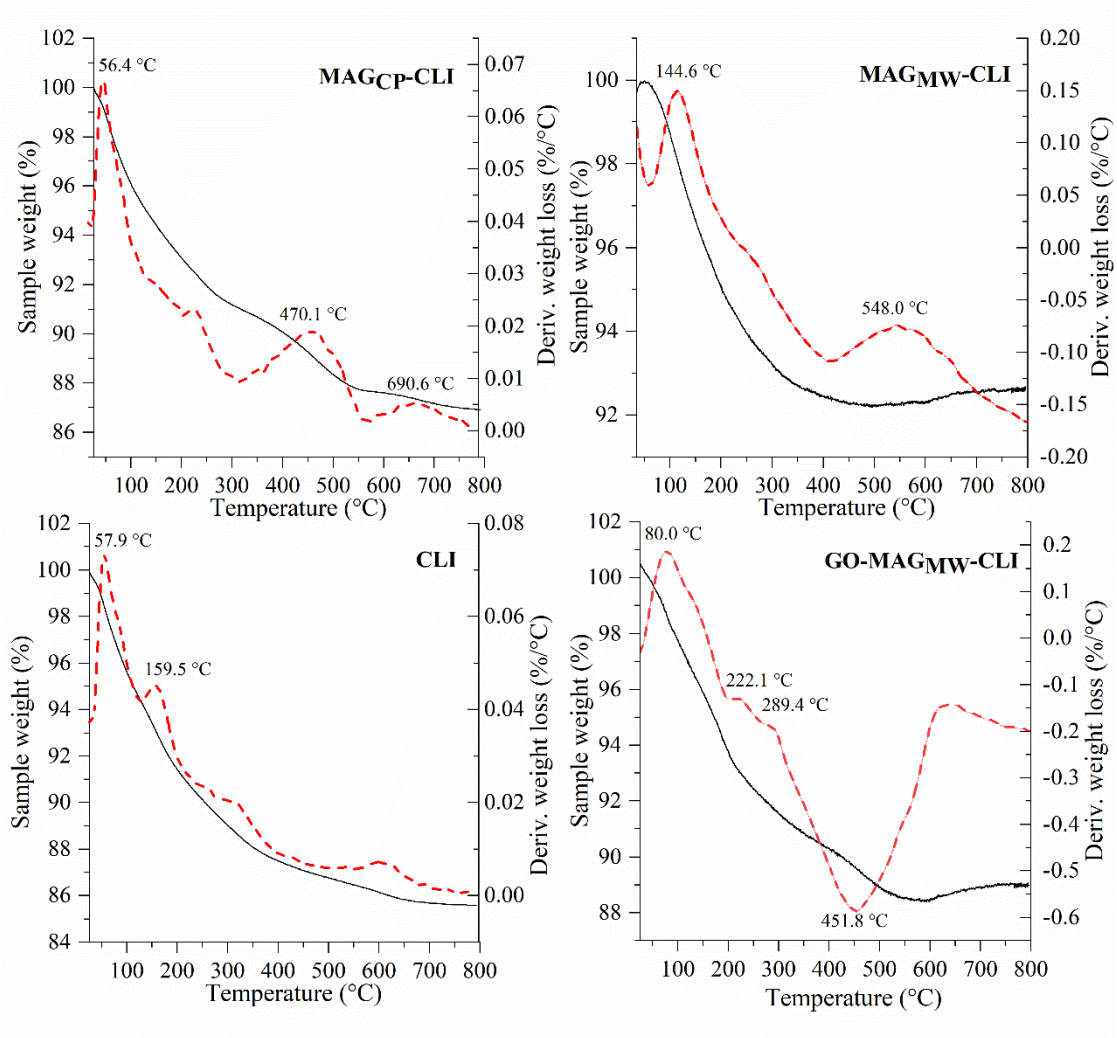

Figure 22. TG (solid line) and DTG (dash line) curves of CLI and CLI-based samples.

Textural properties were studied by N_2 adsorption/desorption isotherms, and the obtained textural parameters are summarized in Table 11. The measured specific surface area of pristine CLI was 23.6 m^2 g^{-1} which is in accordance with the literature data (Garcia-Basabe *et al.*, 2010). Porosity of CLI changes during the modification processes. The specific surface areas (S_{BET}) of MAG$_{CP}$-CLI and MAG$_{MW}$-CLI are approx. two times larger than that of CLI as well as the total pore volume (V_{tot}). Similar results were already reported for the natural zeolite coating with magnetite nanoparticles (Javanbakht *et al.*, 2016; Salem Attia *et al.*, 2014). The pore size diameter (D) of CLI-modified samples is smaller than of CLI, especially of MAG$_{CP}$-CLI. This phenomenon could be explained by the formation of a second layer of magnetite nanoparticles at the CLI surface, and by a partial blockage of the pore system of CLI caused by the formation of the oxide particles (Ahribesh *et al.*, 2017; Javanbakht *et al.*, 2016). The slightly higher S_{BET} of MAG$_{MW}$-CLI compared to MAG$_{CP}$-CLI can be attributed to the lower degree of morphological degradation observed in MAG$_{MW}$-CLI, due to the lesser coverage of magnetite nanoparticles, which was suggested by TEM.

Furthermore, the synergetic effect of both, iron oxide nanoparticles and GO, led to the increase of CLI surface area three times. The increase could be ascribed to the large

surface area of the coated samples (S_{BET}(GO) ~ 400 m^2 g^{-1}) (Wojciechowska & Lendzion-Bielun, 2020; Yu *et al.*, 2013).

Table 11. Textural properties of CLI and CLI-modified samples.

Sample	S_{BET}[a] (m^2 g^{-1})	V_{tot}[b] (cm^3 g^{-1})	D[c] (nm)
CLI	23.6	0.0988	16.3
MAG_{CP}	104.7	0.3001	6.5
MAG_{CP}-CLI	45.2	0.1531	3.5
MAG_{MW}-CLI	52.1	0.1796	12.4
GO-CLI	37.4	0.1202	11.3
GO-MAG_{MW}-CLI	64.8	0.2194	11.8

[a]Specific surface area determined by BET method in p/p_0 range corresponding to the increasing trend of Rouquerol plot; [b]total pore volume based on BJH adsorption analysis; [c]average maximum pore diameter based on BJH desorption analysis.

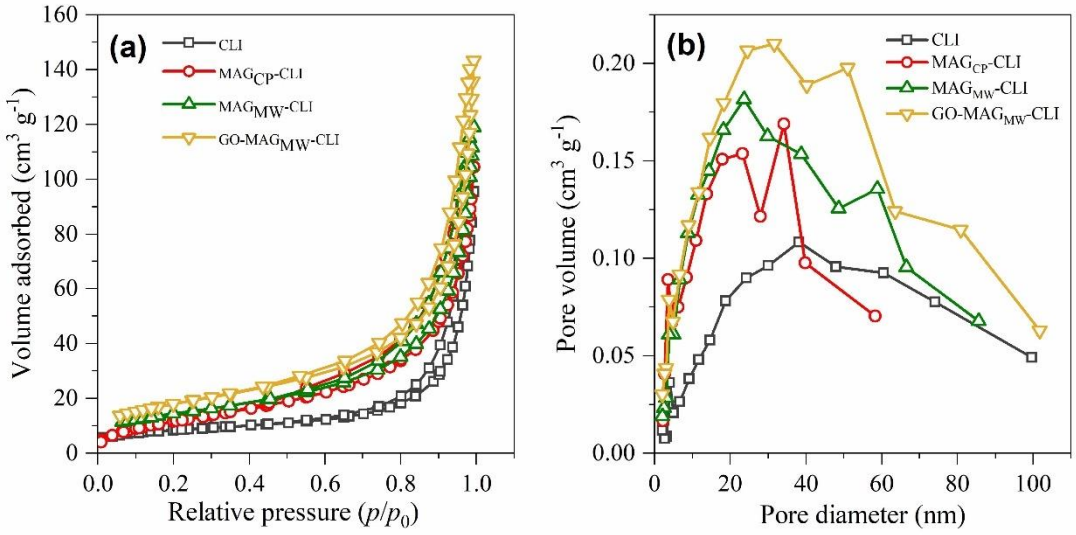

Figure 23. (a) N_2 adsorption/desorption isotherms, and (b) pore size distribution.

According to the IUPAC classification, all samples show type IV of the adsorption/desorption isotherms (Figure 23). This type of isotherm is characteristic for the CLI structure with both micropores (as a result of the lattice structural features) and mesopores formed by the CLI modification (Sing, 1982). The initial part of the type IV isotherm is almost a linear section, which indicates the surface monolayer coverage and beginning of multilayer adsorption. Furthermore, at the higher relative pressures (p/p_0 = 0.5–1), the adsorption isotherms exhibit a type H3 hysteresis loop. For CLI, this can be associated with the multilayer adsorption and capillary condensation in mesopores of impurities (feldspar, quartz, etc.) or in the space between CLI crystals. Moreover, the PSD of the samples differ mutually. The differences can be explained by the creation of an extra pore structure during the synthesis of iron oxide nanoparticles and the GO coating on the surface of CLI (Jevtić *et al.*, 2014).

The FTIR analysis was carried out to analyse the functional groups of synthesized samples and interactions of both iron oxide nanoparticles and GO with CLI surface. The

FTIR spectra of pure iron oxide nanoparticles, CLI and CLI-samples are given in Figure 24. All the spectra obtained for the modified samples exhibit vibrations that are characteristic for the zeolite lattice and suggests that the aluminosilicate lattice left preserved after the modifications.

Vibration bands around 463 and 1042 cm^{-1} in CLI spectrum corresponds to asymmetric bending and stretching modes of Si–O or Al–O bonds, within the internal tetrahedra of CLI structure, respectively. A vibration band visible around 606 cm^{-1} belongs to the stretching bonds between tetrahedral units (Aeenjan & Javanbakht, 2018; Zendelska *et al*., 2018). Two broad bands in the region between 3400 and 3700 cm^{-1} are assigned to the stretching vibrations of the hydroxyl groups present in surface water molecules, while the band appears at around 1640 cm^{-1} belongs to free water molecules in the CLI structure (Zendelska *et al*., 2018).

In the spectra of MAG_{CP}-CLI and MAG_{MW}-CLI, strong vibrations of the hydroxyl groups in the range of 1590–1670 and 3400–3700 cm^{-1} are evident. Moreover, vibration of the $(Al, Si)O_4$ tetrahedral units at 1050–1250 cm^{-1} indicate that the modifications by magnetic iron oxide nanoparticles did not influence significantly the CLI aluminosilicate lattice (Savić *et al*., 2016). The MAG_{CP} and MAG_{MW} spectra display a strong characteristic band of the Fe–O stretching at around 570 cm^{-1}, which is assigned to the vibration of the Fe(II)–O functional group. The splitting-up peak at around 650 cm^{-1} may correspond to the symmetry degeneration of octahedral B sites (Khalil, 2015). In the spectra of MAG_{CP}-CLI and MAG_{MW}-CLI characteristic band of iron oxide is not visible due to overlapping with the strong vibration bands of the aluminosilicate lattice (Ahribesh et al., 2017; Lin et al., 2015).

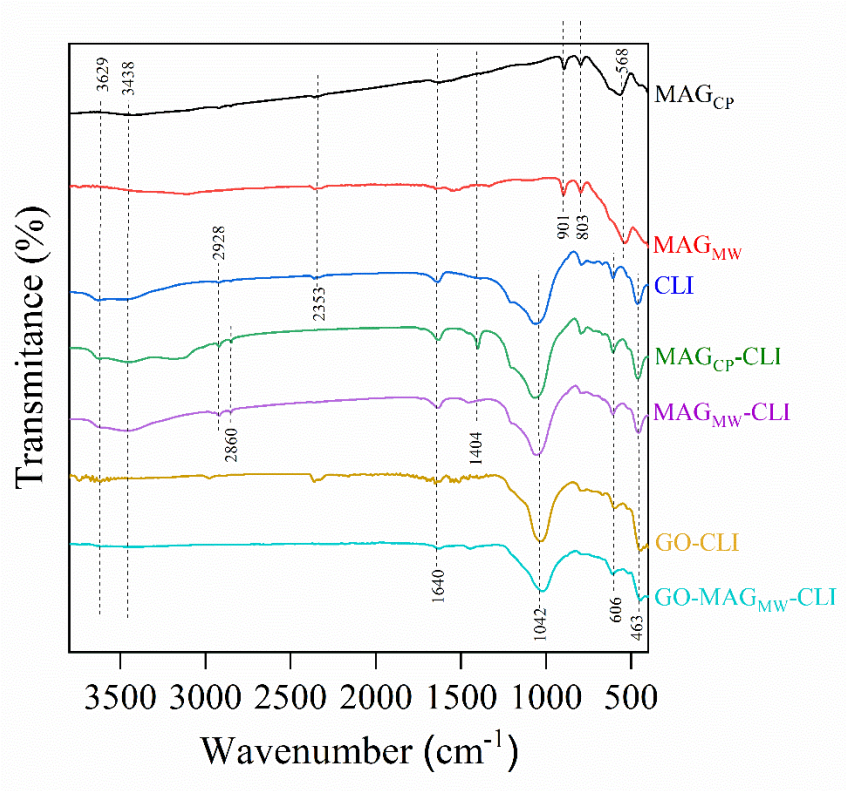

Figure 24. FTIR spectra of synthetized magnetic nanoparticles, CLI, and CLI-based samples.

The FTIR spectrum of pure GO (not shown) consists of various vibration bands, containing functionalities on the surface and on the edges of the GO sheet. In the spectrum of GO-CLI, a weak band observed at 3600 cm^{-1} belongs the bonded hydroxyl of phenol group, while low intensity band at 2979 cm^{-1} can be assigned to C–H stretching. Moreover, the band observed at around 1509 cm^{-1} is associated with the O stretching of carboxylic group present in GO structure, while the band appearing at 1446 cm^{-1} is caused by deformations of the C–OH groups. In the spectra of GO-CLI and GO-MAG_{MW}-CLI, the more distinct vibration bands of GO at around 1640 cm^{-1}, and in the range 800–1083 cm^{-1} correspond to aromatic C=C groups and C–O stretching vibration, respectively, are overlapping with the more prominent bands of CLI lattice (Chen et al., 2015; Wang et al., 2016). It is worth noticing that the ultrasound treatment of the GO water dispersion may lead to the reduction of carbon-oxygen functional groups. The OH radicals produced by ultrasonic cavitation can interact with the readily oxygenated groups of GO (epoxide, hydroxyl, and carboxyl), resulting in their partial elimination (Le *et al*., 2019). The low intensity band at around 2353 cm^{-1} evident in MAG_{MW}, CLI and GO-CLI spectra can be assigned to adsorbed atmospheric CO_2 (Al-Gaashani *et al.*, 2019; Pendyala *et al*., 2019).

Raman spectroscopy based on band intensity and band surface measurements was applied to detect GO in the CLI-modified sample. The Raman spectra of the commercial GO and GO-CLI are shown in Figure 25. The bands at approximately 1350 cm^{-1} (band D) and 1600 cm^{-1} (band G) in the GO spectrum correspond to sp^3 C atoms as well as of vibrations of sp^2 C atoms in the hexagonal graphite structure, respectively (Sohrabi *et al*., 2021). These peaks are also visible in the GO-CLI spectrum confirming the presence of GO in the GO-CLI.

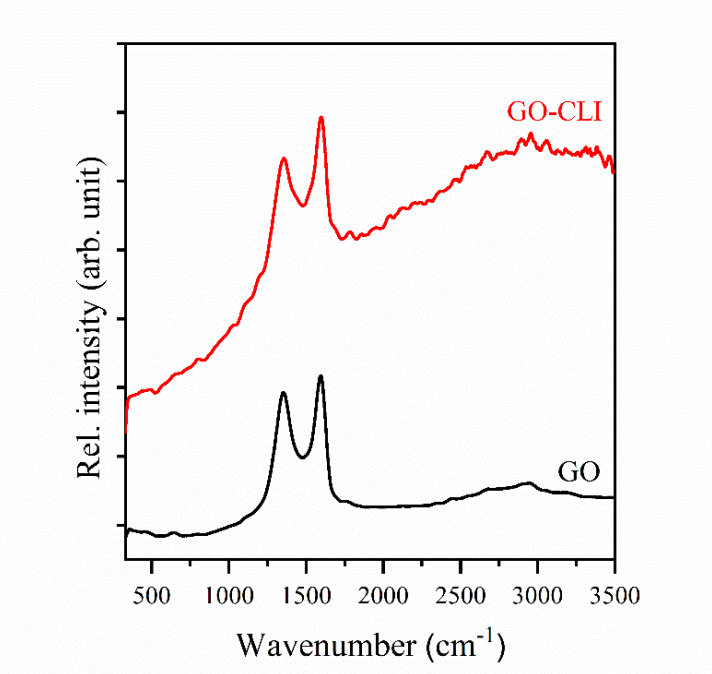

Figure 25. Raman spectra of GO and GO-CLI samples.

Due to the zwitterionic nature of CIP structure, its adsorption is strongly pH dependent. The zeta potential of the samples as a function of pH are shown in Figure 26. Pristine CLI has a negatively charged surface over the entire range of investigated pH values. The zeta

potential of CLI slightly changed with the modifications, although all three modified samples still have a negatively charged surface in a wide pH range (3–12). The PZC of MAG_{CP}-CLI was at a pH ~ 2, while for MAG_{MW}-CLI and GO-MAG_{MW}-CLI PZC is negligibly higher (around pH of 2.4). The obtained PZC values are in accordance with the literature data (Cotton, 2008). In the case of MAG_{MW}-CLI and GO-MAG_{MW}-CLI samples, the surface is positively charged at pH below PZC with the –OH and –COOH groups of GO in a form of $–OH_2^+$ and $–COOH_2^+$. At the pH values higher than PZC, these groups were ionized and GO-MAG_{MW}-CLI surface is negatively charged.

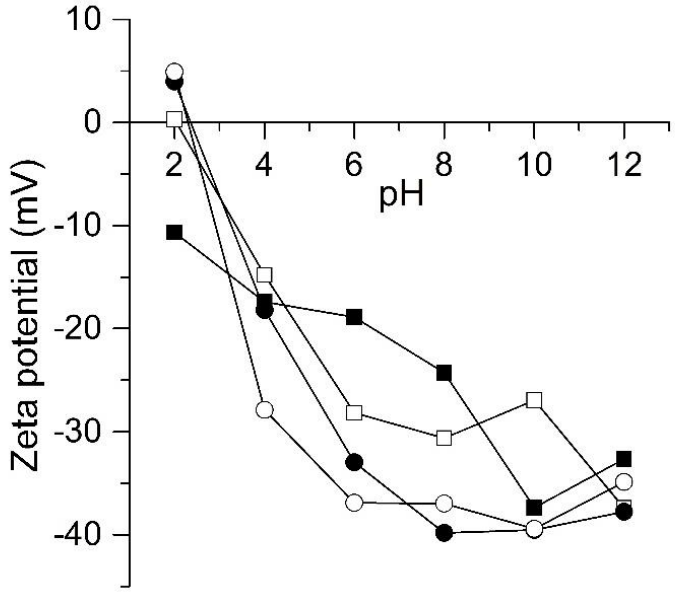

Figure 26. Zeta potential measurements as a function of pH for CLI (solid square), MAG_{CP}-CLI (open square), MAG_{MW}-CLI (solid circle) and GO-MAG_{MW}-CLI (open circle).

The magnetic properties of MAG_{CP}-CLI, MAG_{MW}-CLI and GO-MAG_{MW}-CLI were also studied and compared with those of MAG_{CP} and MAG_{MW}. The magnetization curves are present in Figure 27a. All studied samples showed similar magnetic behaviour within a magnetic field lower than 2 T, with the saturation magnetization values given in Table 12. The lower saturation magnetization value of MAG_{CP}-CLI and MAG_{MW}-CLI in comparison to pure magnetic particles is the result of iron oxides precipitation on the CLI surface. The results confirm that the magnetic nanoparticles covering of CLI induces magnetic properties since the CLI itself does not exhibit magnetism. Furthermore, the magnetization loops showed an absence of hysteresis, which is a characteristic of the superparamagnetic nature of some nanoparticles (Kouli *et al*., 2018). It is worth noticing that MAG_{CP}-CLI, MAG_{MW}-CLI and GO-MAG_{MW}-CLI retain magnetic properties after the CIP adsorption (Figure 27b), suggesting that the magnetic separation of the spent magnetic adsorbents from water media is possible.

Table 12. Saturation magnetization parameter of synthetized magnetic particles and magnetic CLI-based adsorbents.

Sample	Saturation magnetization (emu g^{-1})
CLI	–
MAG_{CP}	49.57
MAG_{MW}	43.29
MAG_{CP}-CLI	8.93
MAG_{MW}-CLI	11.58
GO-MAG_{MW}-CLI	12.04

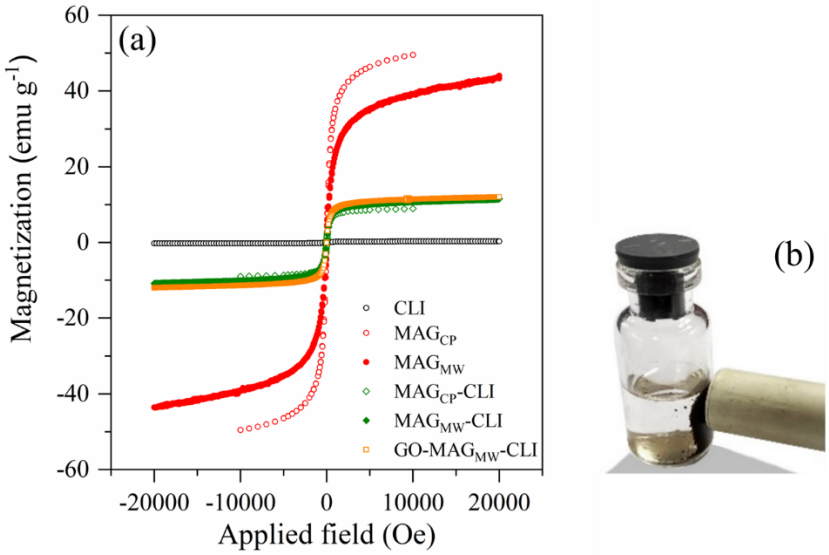

Figure 27. The (a) magnetization curves of synthetized magnetite nanoparticles, CLI and CLI-based samples, and (b) magnetic separation of the spent MAG_{CP}-CLI from the suspension.

Optimization of the CIP adsorption using statistical analysis

Evaluation of optimal adsorption parameters for adsorption of CIP onto CLI, MAG_{MW}-CLI, and GO-MAG_{MW}-CLI was carried out using the RMS-CCF design. For the model application 90 experiments were performed, including 12 axial points, 48 factorial or cube points and 30 replicates at the centre point.

Firstly, the data were examined to verify the normality of the residuals via the normal probability plot of residuals, as shown in Figure 28a. The residuals are on the straight line, indicating the normality and the adequacy of the predicted model. The plot of internally studentized residuals versus predicted response values (Figure 28b) shows an even distribution of points above and below the x-axis. The model was deemed appropriate and reliable, with a high coefficient of determination (R^2 = 0.9989).

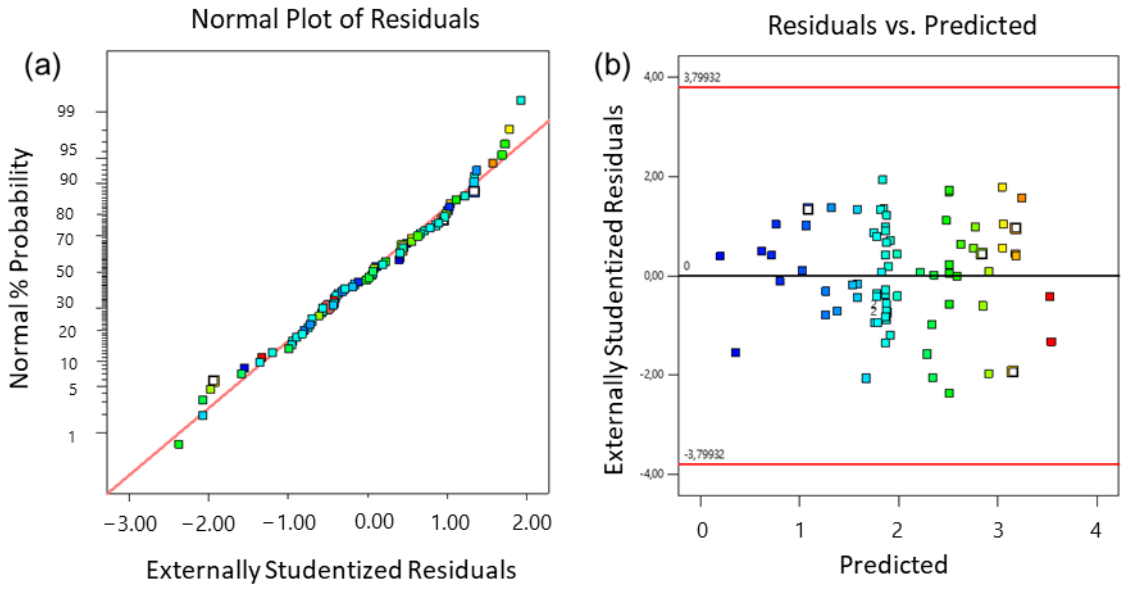

Figure 28. A (a) normal probability plot of residuals, and (b) studentized residuals versus predicted values plot.

To assess the adequacy and validity of the model and to determine the significant effects and possible interactions between variables, ANOVA[7] was used for which the tests hypotheses based on the model parameters were used (Najafpoor *et al*., 2019; Shafeeyan *et al*., 2012). The ANOVA results for the polynomial model are presented in Table 13. It is evident that the *F*- and *p*-values of the developed model are equal to 596.73 and <0.0001, respectively. Thus, the developed polynomial model is highly significant for the removal of CIP by CLI-based adsorbents. The variables that have the most significant impact on the CIP adsorption are the linear parameters of initial CIP concentration (A); pH value (B); type of adsorbent (E); and interaction terms BE, CE, and BCE. Controlling these variables leads to the optimization of the CIP adsorption process and improves the efficiency of the CLI-based adsorbents in removal of CIP.

To describe the CIP adsorption onto the CLI samples, the adsorption results, i.e., the adsorption capacities were introduced into the higher-order polynomial models. To achieve the best statistical properties of the model, a square root transformation had to be applied to transform the response. The relative impact of the factors on the CIP removal can be identified by analysing the values of the coefficients of the final equation, which is expressed in coded factors using Equation (12).

[7] Analysis of variance.

Table 13. ANOVA analysis for the model.

Source	Sum of squares	df	Mean square	*F*-value	*p*-value	Importance
Model	43.95	53	0.8293	596.73	< 0.0001	significant
A-Initial concentration	18.56	1	18.56	13351.50	< 0.0001	
B-pH	10.89	1	10.89	7836.64	< 0.0001	
C-Temperature	0.0007	1	0.0007	0.5325	0.4703	
D-Contact time	0.2781	1	0.2781	200.10	< 0.0001	
E-Adsorbent	6.97	2	3.48	2506.08	< 0.0001	
AB	0.1302	1	0.1302	93.72	< 0.0001	
AD	0.0165	1	0.0165	11.84	0.0015	
AE	0.2206	2	0.1103	79.37	< 0.0001	
BC	0.0553	1	0.0553	39.78	< 0.0001	
BE	1.71	2	0.8528	613.63	< 0.0001	
CE	2.11	2	1.05	758.14	< 0.0001	
DE	0.0698	2	0.0349	25.10	< 0.0001	
B^2	0.0107	1	0.0107	7.67	0.0088	
C^2	0.0097	1	0.0097	7.00	0.0120	
D^2	0.0078	1	0.0078	5.62	0.0233	
ABC	0.0108	1	0.0108	7.74	0.0085	
ABE	0.1039	2	0.0519	37.38	< 0.0001	
ACE	0.3642	2	0.1821	131.04	< 0.0001	
ADE	0.0137	2	0.0068	4.92	0.0129	
BCD	0.0094	1	0.0094	6.80	0.0132	
BCE	1.28	2	0.6383	459.31	< 0.0001	
CDE	0.0091	2	0.0045	3.27	0.0494	
A^2B	0.0347	1	0.0347	24.97	< 0.0001	
A^2C	0.0787	1	0.0787	56.60	< 0.0001	
A^2E	0.0765	2	0.0382	27.51	< 0.0001	
B^2E	0.0603	2	0.0302	21.70	< 0.0001	
C^2E	0.0532	2	0.0266	19.14	< 0.0001	
ABCE	0.0567	2	0.0283	20.39	< 0.0001	
A^2B^2	0.0390	1	0.0390	28.06	< 0.0001	
A^2BE	0.0325	2	0.0162	11.68	0.0001	
A^2CE	0.0921	2	0.0461	33.15	< 0.0001	
AB^2E	0.0680	2	0.0340	24.48	< 0.0001	
ABCDE	0.0141	2	0.0071	5.09	0.0113	
A^2B^2E	0.3640	2	0.1820	130.97	< 0.0001	
Residual	0.0500	36	0.0014			
Lack of Fit	0.0297	21	0.0014	1.04	0.4770	not significant
Pure Error	0.0203	15	0.0014			
Cor Total	44.00	89				

The final equations in terms of actual factors for CLI, MAG_{MW}-CLI and GO-MAG_{MW}-CLI and the adsorption capacity for CIP were expressed by equations (13), (14) and (15), respectively. Factors variables are denoted as follows: A = X_1, B = X_2, C = X_3 and D = X_4.

$$\begin{aligned}\text{Sqrt}(q)= {} & 2.08 +0.5862\cdot A -0.3774\cdot B +0.1117\cdot C +0.0718\cdot D -0.2097E[1] -0.2156E[2] \\ & -0.0521\cdot AB +0.0185\cdot AD +0.044\cdot AE[1] -0.1374\cdot AE[2] -0.0339\cdot BC -0.1154\cdot BE[1] \\ & -0.1207\cdot BE[2] -0.3838\cdot CE[1] +0.3332\cdot CE[2] -0.0228\cdot DE[1] -0.0279\cdot DE[2] \\ & +0.0949\cdot B^2 +0.045\cdot C^2 -0.0403\cdot D^2 +0.015\cdot ABC +0.0396\cdot ABE[1] +0.0256\cdot ABE[2] \\ & -0.0683\cdot ACE[1] +0.1229\cdot ACE[2] +0.0031\cdot ADE[1] -0.022\cdot ADE[2] +0.014\cdot BCD \\ & -0.1472\cdot BCE[1] +0.2274\cdot BCE[2] +0.0034\cdot CDE[1] -0.0183\cdot CDE[2] -0.0807\cdot A^2B \\ & -0.1214\cdot A^2C +0.3386\cdot A^2E[1] -0.3314\cdot A^2E[2] +0.2901\cdot B^2E[1] -0.1964\cdot B^2E[2] \\ & +0.0682\cdot C^2E[1] -0.1487\cdot C^2E[2] -0.0383\cdot ABCE[1] +0.0451\cdot ABCE[2] -0.1637\cdot A^2B^2 \\ & +0.0987\cdot A^2BE[1] -0.0921\cdot A^2BE[2] +0.1855\cdot A^2CE[1] -0.0826\cdot A^2CE[2] \\ & -0.1318\cdot AB^2E[1] +0.144\cdot AB^2E[2] -0.007\cdot ABCDE[1] +0.0236\cdot ABCDE[2] \\ & -0.5789\cdot A^2B^2E[1] +0.6417\cdot A^2B^2E[2]\end{aligned} \quad (12)$$

$$\begin{aligned}Y^{1/2}= {} & -16.01+1.51X_1+4.84X_2+0.07X_3+0.04X_4-0.41X_1X_2-0.005X_1X_3+0.0002X_1X_4- \\ & 0.01X_2X_3+0.0001X_3X_4-0.02X_1^2-0.34X_2^2+0.001X_3^2-0.002X_4^2- \\ & 0.0001X_1X_2X_3+0.00001X_2X_3X_4+0.01X_1^2X_2+0.03X_1X_2^2+0.01X_1^2X_2+0.03X_1X_2^2- \\ & 0.0005X_1^2X_2^2\end{aligned} \quad (13)$$

$$\begin{aligned}Y^{1/2}= {} & 25.38-1.59X_1- \\ & 6.98X_2+0.03X_3+0.05X_4+0.46X_1X_2+0.002X_1X_3+0.00005X_1X_4+0.005X_2X_3- \\ & 0.0002X_3X_4+0.03X_1^2+0.46X_2^2+0.003X_3^2-0.002X_4^2+0.0003X_1X_2X_3+0.00001X_2X_3X_4- \\ & 0.01X_1^2X_2-0.00005X_1^2X_3-0.03X_1X_2^2-0.000001X_1X_2X_4+0.0005X_1^2X_2^2\end{aligned} \quad (14)$$

$$\begin{aligned}Y^{1/2}= {} & 0.15X_1+0.81X_2-0.02X_3+0.04X_4-0.04X_1X_2+0.003X_1X_3+0.0002X_1X_4- \\ & 0.01X_2X_3+0.0001X_3X_4-0.002X_1^2-0.05X_2^2+0.001X_3^2- \\ & 0.002X_4^2+0.00005X_1X_2X_3+0.000004X_2X_3X_4+0.001X_1^2X_2- \\ & 0.0001X_2^2X_3+0.003X_1X_2^2+0.000001X_1X_2X_3X_4-0.0001X_1^2X_2^2\end{aligned} \quad (15)$$

Variables effects on the CIP adsorption

Contour diagrams (Figure 29) and three-dimensional diagrams (Figures 30–32) could help in clarification of the effects of independent variables on the responses at different points (Sabbagh *et al*., 2021). The optimal conditions that provide the maximum CIP adsorption are acquired using the multicriteria optimisation process and are presented via contour diagrams shown in Figure 29 and in Table 14.

Table 14. Optimal conditions for the CIP adsorption onto CLI-based adsorbents.

Adsorbent	Optimal solution
CLI	C_0 (CIP) = 50 mg dm^{-3} pH = 6.41 T = 9.85 °C t = 18.95 min
MAG_{MW}-CLI	C_0 (CIP) = 50 mg dm^{-3} pH = 5 T = 20.98 °C t = 13.70 min
GO-MAG_{MW}-CLI	C_0 (CIP) = 48.47 mg dm^{-3} pH = 5.10 T = 24.78 °C t = 19.20 min

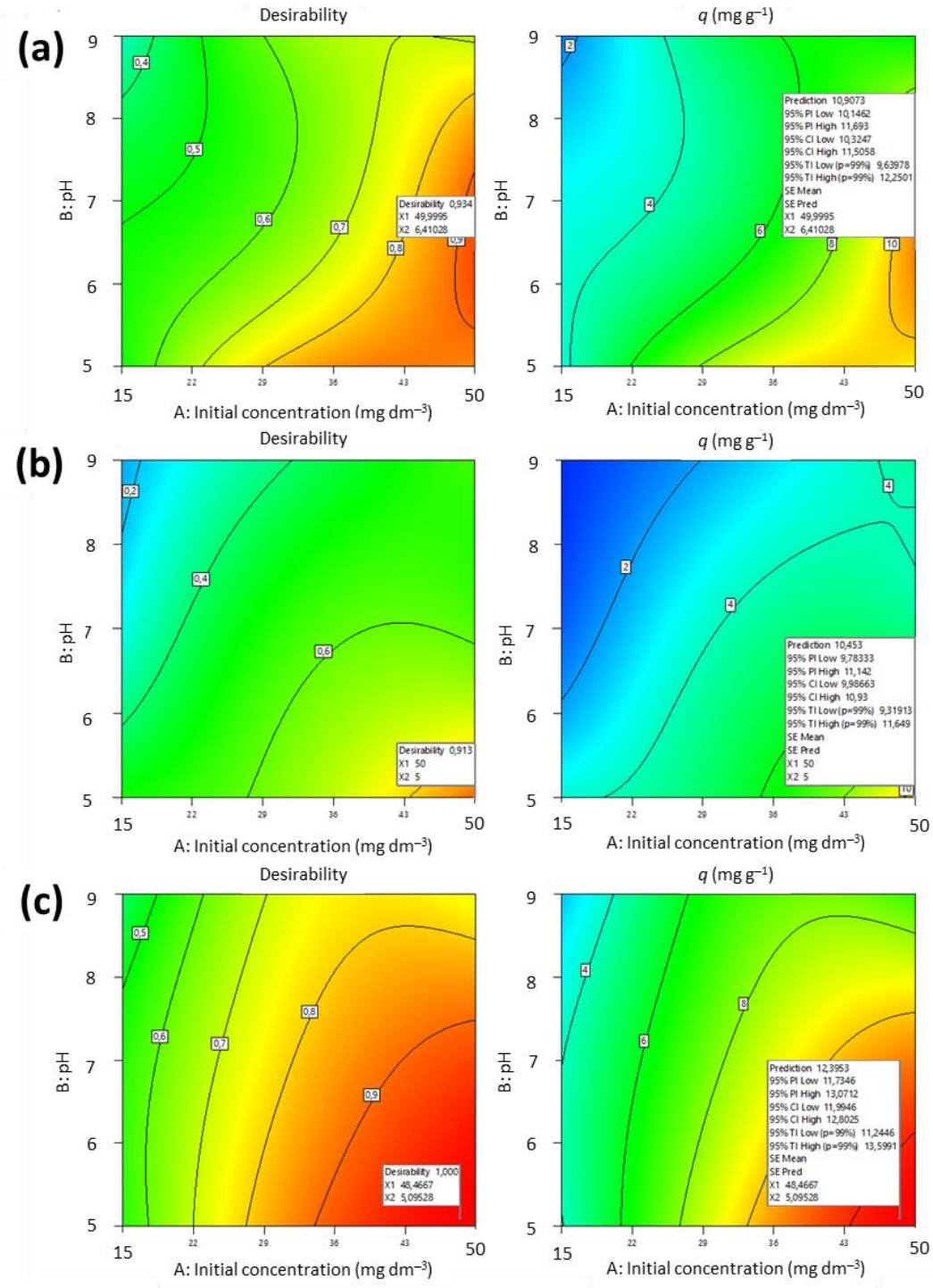

Figure 29. Contour diagrams optimization of adsorption capacity for (a) CLI, (b) MAG_{MW}-CLI, and (c) GO-MAG_{MW}-CLI.

The impact of different operating parameters, such as initial CIP concentration, pH, temperature, and contact time, on the adsorption of CIP onto CLI, MAG_{MW}-CLI and GO-MAG_{MW}-CLI adsorbents was studied. Three-dimensional surface plots (Figures 30–32) were developed to depict the interactive effects of the initial CIP concentration and pH at three different temperatures and for all three adsorbents at fixed contact time of 20

minutes. The contact time is one of the most significant parameters in determination of wastewater treatment cost-effectiveness, as the removal efficiency of contaminants typically increases until the equilibrium is reached (Thy *et al*., 2021; Zhang *et al*., 2021). Thus, the adsorption capacity of all three studied adsorbents increases with increasing contact time, and the results obtained for the maximum studied time are shown.

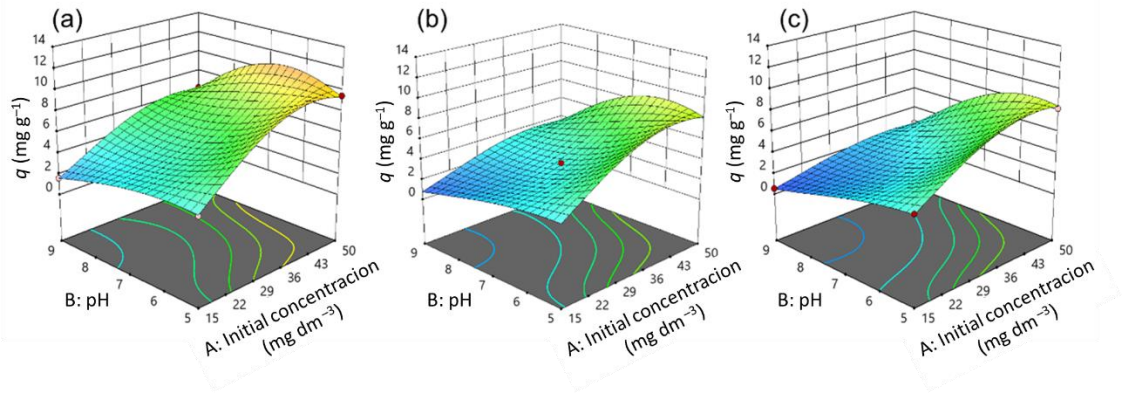

Figure 30. 3D representation of response surface plots for CLI adsorbent at constant time of 20 min for (a) 10 °C, (b) 17.5 °C, and (c) 25 °C.

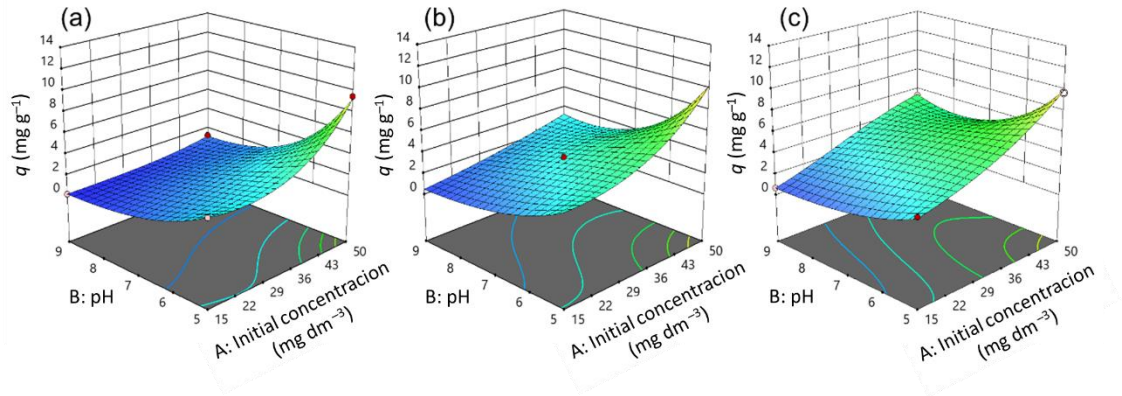

Figure 31. 3D representation of response surface plots for MAG_{MW}-CLI adsorbent at constant time of 20 min for (a) 10 °C, (b) 17.5 °C, and (c) 25 °C.

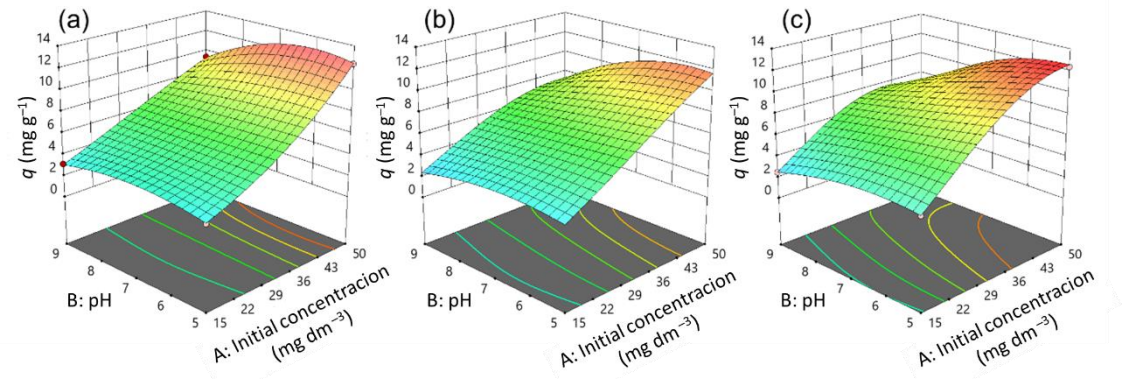

Figure 32. 3D representation of response surface plots for GO-MAG_{MW}-CLI adsorbent at constant time of 20 min for (a) 10 °C, (b) 17.5 °C, and (c) 25 °C.

The adsorption capacity of CIP was found to be strongly influenced by its initial concentration, and in general, the higher initial antibiotic concentration resulting in increased adsorption capacity. The improvement of the adsorption capacity for CIP by increasing the CIP concentration in the solution could be attributed to an increase in the concentration gradient, which serves as the driving force for adsorption, as well as the availability of more uncovered adsorbent's surface area at the beginning of the process (Javanbakht *et al*., 2016; Mohseni-Bandpi *et al*., 2016). This result is comparable with the ones obtained for the CIP removal using activated carbon (Zhang *et al*., 2021).

The pH value provides to be the second most significant factor that affects the CIP adsorption onto CLI, MAG_{MW}-CLI and GO-MAG_{MW}-CLI. The reason for this is the influence of pH on the surface properties (i.e., surface charge) of the adsorbent and the adsorbate molecules, which determine their integration pathway (Genç & Dogan, 2015). As Figures 30–32 point out, the adsorption capacity of the adsorbents for CIP slightly increased as pH decreased from 9 to 5, with an optimum pH for CIP adsorption onto CLI-based adsorbents of around 5. Due to the zwitterionic character of CIP molecule, it exists as a cation at pH below 5.90, while pH values above 8.89 favour its anionic form (Carabineiro *et al*., 2012; Genç & Dogan, 2015). Therefore, at a pH of 5, the CLI-based adsorbents and CIP molecules were attracted to each other, resulting in increased adsorption efficiency. Conversely, at a pH above 8.89, the adsorption efficiency decreased due to the electrostatic repulsion between the anionic form of CIP and the negatively charged surface of the adsorbents. This result is consistent with the findings already reported by Najafpoor *et al*. (Najafpoor *et al*., 2019) for the removal of CIP from synthetic wastewater using γ-Al_2O_3 nanoparticles.

The interaction between the initial CIP concentration and pH at different temperatures showed that GO-MAG_{MW}-CLI had a maximum adsorption capacity for CIP at the highest temperature applied (Figure 32c), the CLI had a maximum adsorption capacity at the lowest investigated temperature (Figure 30a), while the adsorption capacity of MAG_{MW}-CLI did not change significantly with the temperature (Figure 31). The decrease in CLI adsorption ability with the temperature increase can be explained by the Le Chatelier's principle, since the adsorption process mainly occurs as an exothermic process. A degree of decrease in adsorption ability depends on the heat of adsorption; the higher the adsorption heat, the higher the temperature needed to decrease the adsorption ability to some extent (Tian *et al*., 2016). The improvement of the CIP molecules' mobility with an increase in the solution temperature can, consequently, lead to the equilibrium shift towards desorption. A similar trend was reported for the antibiotic cephalexin adsorption by Fe_3O_4 nanoparticles (Mohseni-Bandpi *et al*., 2016). The lower adsorption ability of MAG_{MW}-CLI for CIP in comparison to the ability of pristine CLI could be ascribed to the slightly degraded CLI surface after the magnetic nanoparticles' precipitation, resulting in a decrease in the number of active sites on the surface available for the adsorption of CIP.

As expected, for all studied temperatures, the GO-MAG_{MW}-CLI showed the highest adsorption capacity for CIP. It was found that GO itself had an excellent adsorption ability for CIP, which can only contribute CIP adsorption on GO-modified CLI (Chen *et al*., 2015). GO could improve the CLI adsorption efficacy by enlarging its active surface area and subsequently the amount of surface sites available for the antibiotic adsorption (Kim *et al*., 2018a; Silva *et al*., 2020).

4.2. Adsorption experiments

Effect of adsorbent dosage on CIP removal efficiency

The effect was studied by varying the amount of CLI and MAG_{CP}-CLI from 0.01 to 0.20 g at an initial CIP concentration of 50 mg dm^{-3}, pH = 5, and contact time of 60 min at 25 °C. As shown in Figure 33, the CIP adsorption efficiency increased with increasing adsorbent amount. The removal efficiency gradually increased for all the adsorbents investigated, with a 10% increase in CIP removal efficiency when the adsorbent mass was doubled. Based on these results, a solid-to-liquid ratio of 0.20 g of adsorbent per 50 cm^3 of CIP solution was chosen as the optimal ratio for further experiments.

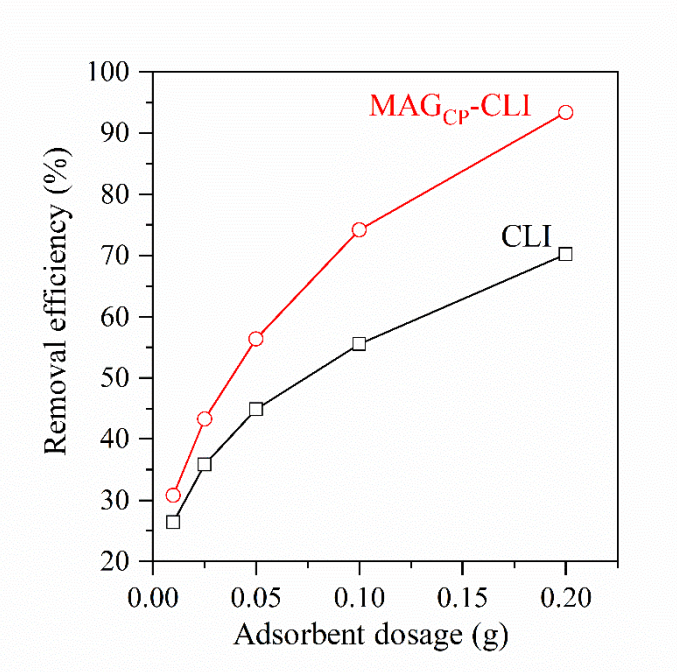

Figure 33. Effect of the adsorbent dosage on CIP adsorption.

Effect of pH on CIP removal efficiency

Figure 34 shows influence of pH on CIP removal. The removal efficiency decreased in alkaline medium, which is in accordance with the fact that both CIP molecules and adsorbents surface are negatively charged. In an acidic medium, CIP is positively charged (CIP^+), and the attractive forces between CIP^+ and adsorbents favour the adsorption. The highest removal efficiency was achieved at pH = 5. Similar results were reported for metal oxides, clays, and GO composite (Duan *et al.*, 2017; Najafpoor *et al.*, 2019; Rakshit *et al.*, 2013; F. Wang *et al.*, 2016).

The adsorption of CIP onto CLI and the CLI-modified samples depends on pH with a bell-shaped adsorption envelope. The adsorption increased with pH reaching a maximum at pH = 5 and then decreased sharply with increasing pH. The observed bell-shaped adsorption envelope could be explained by both pH dependence of CIP speciation and CIP surface charge (Trivedi & Vasudevan, 2007). At highly acidic conditions, both CIP and CLI surfaces have similar charge which disables the CIP interactions with CLI surface due to electrostatic repulsions. Is worth noticing that the CIP adsorption onto CLI

can be compared with the adsorption onto nano-Fe_3O_4 at a similar pH range. This suggests that the CIP adsorption on magnetic CLI occurs via similar mechanism in which the CIP uses its keto (–C=O) and carboxyl (–COOH) groups (Rakshit *et al.*, 2013; Trivedi & Vasudevan, 2007).

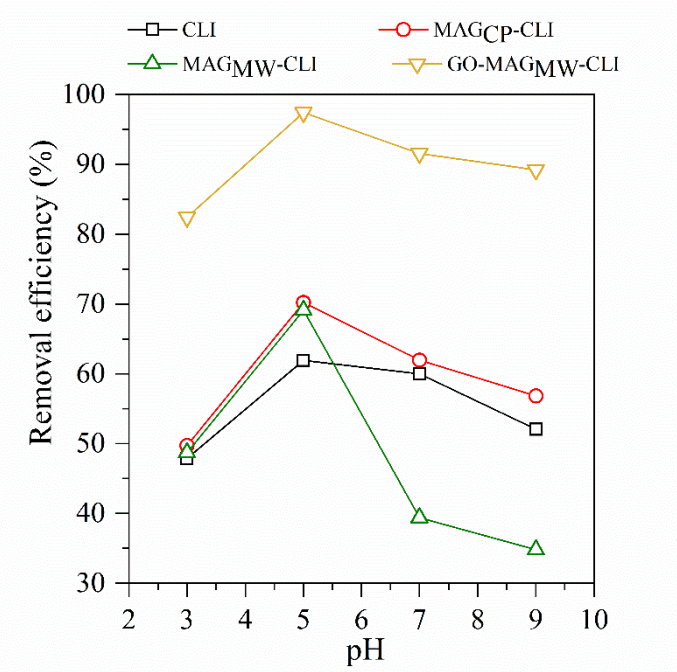

Figure 34. The influence of pH in the CIP adsorption (C_0 = 50 mg dm^{-3}, t = 60 min, adsorbent dose = 4 g dm^{-3} and T = 25 °C).

Effect of initial concentration

The effect of the initial CIP concentration was studied in the concentration range of 15–75 mg dm^{-3}. Figure 35 shows the change in the amount of adsorbed CIP (q_t) on pristine CLI and CLI-modified samples at 10 °C showing that q_t increases with the initial concentration for all investigated samples. However, efficiency differs for the different samples. The most significant adsorption effect was observed for GO-MAG$_{MW}$-CLI, with the q_t changing from 3.73 (C_0 = 15 mg dm^{-3}) to 17.84 mg g^{-1} (C_0 = 75 mg dm^{-3}).

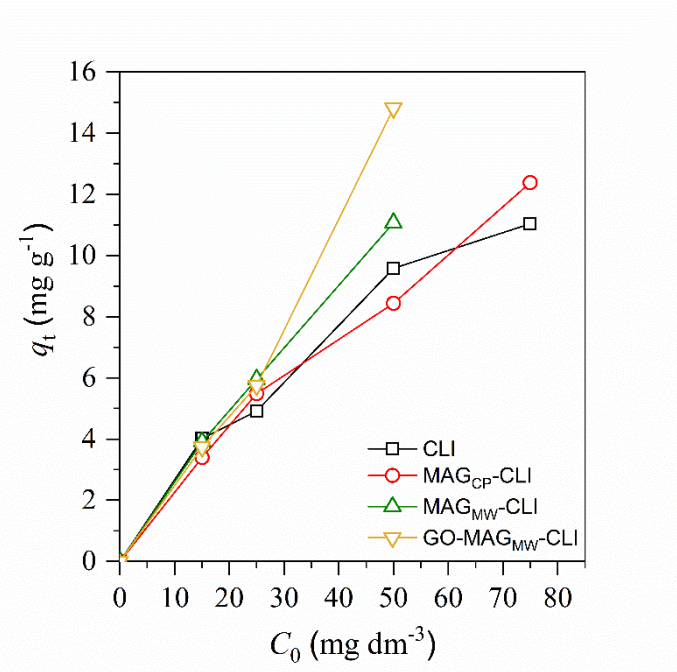

Figure 35. Effect of the initial concentration on the CIP adsorption efficiency.

Adsorption kinetics

The adsorption kinetics was studied at 10, 15 and 20 °C for different initial concentrations: C_0 = 15, 25 and 50 mg CIP dm^{-3}. The CIP uptakes by CLI, MAG$_{CP}$-CLI, MAG$_{MW}$-CLI and GO-MAG$_{MW}$-CLI are shown in Figure 36. It is evident that the q_t increases with contact time for all studied samples. The CIP adsorption rather sharply increases in the first 10 min of contact time for all studied temperatures and initial concentrations. Then, the adsorption occurs more slowly due to the adsorbent saturation. Within the first 10 min, more than 85% of the maximum adsorption capacity was achieved, indicating fast adsorption kinetics.

Furthermore, the kinetic results were analysed by two kinetic models (Lagergren pseudo-first order, Lagergren pseudo-second-order models) and one diffusion-based model (Weber-Morris model) that are the most applied models for the studying the adsorption of different species from aqueous media onto zeolites. The obtained kinetic parameters for all studied CLI-based adsorbents are summarized in Tables 15 and 16.

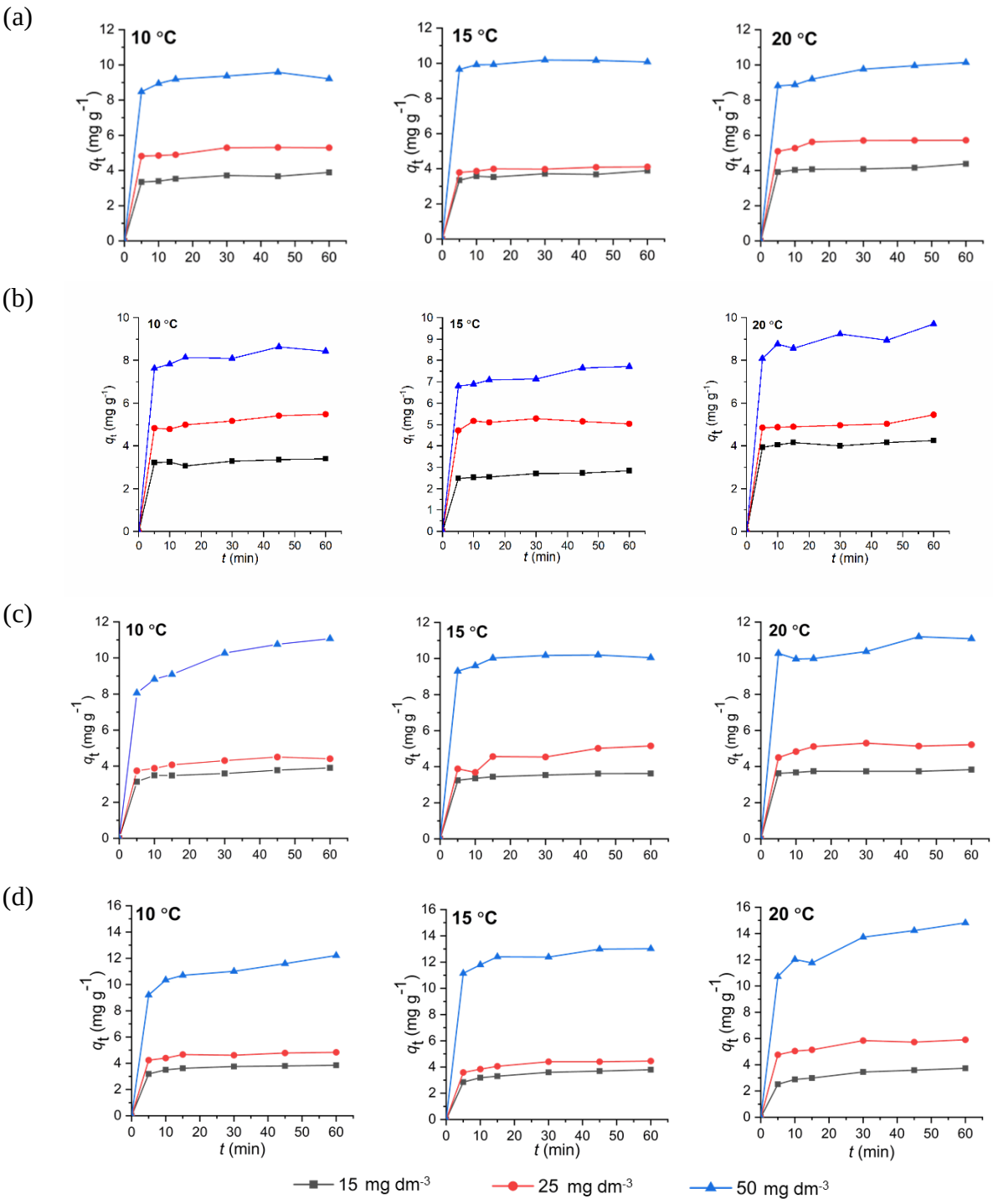

Figure 36. CIP adsorption kinetics on (a) CLI, (b) MAG_{CP}-CLI, (c) MAG_{MW}-CLI, and (d) GO-MAG_{MW}-CLI for different temperatures; q_t is the amount of the adsorbed CIP (mg per 1 g of adsorbent) after time *t*.

Table 15. Rate constants for the three studied kinetic models for the adsorption of CIP on CLI and MAG_{CP}-CLI.

CLI										
C_0 (mg dm^{-3})	T (°C)	LPFO[a]			LPSO[b]			Weber-Morris		
		k_1 (h^{-1})	q_e (mg g^{-1})	R^2	k_2 (g mg^{-1} min^{-1})	q_e (mg g^{-1})	R^2	K_{id} (mg g^{-1} min$^{-1/2}$)	I (mg g^{-1})	R^2
15	10	0.1429	1.77	0.8831	0.3393	4.09	0.9999	0.0729	3.54	0.9301
	15	0.0682	1.35	0.7379	0.2490	4.28	0.9998	0.0768	3.66	0.9638
	20	0.0936	0.91	0.4654	0.2275	4.82	0.9996	0.0599	4.29	0.9221
25	10	0.0358	1.23	0.3556	0.1896	4.90	0.9988	0.0592	4.35	0.7707
	15	0.0872	1.21	0.7371	0.2900	5.13	0.9999	0.0820	4.50	0.8933
	20	0.2133	2.87	0.8107	0.4011	5.24	0.9995	0.0377	4.99	0.5450
50	10	0.0609	4.16	0.7856	0.0436	9.78	0.9983	0.3033	7.15	0.9436
	15	0.0545	2.92	0.6773	0.0703	8.63	0.9991	0.1946	6.93	0.9386
	20	0.0395	2.89	0.5081	0.0714	8.94	0.9989	0.1632	7.44	0.8792
MAG_{CP}-CLI										
C_0 (mg dm^{-3})	T (°C)	LPFO			LPSO			Weber-Morris		
		k_1 (h^{-1})	q_e (mg g^{-1})	R^2	k_2 (g mg^{-1} min^{-1})	q_e (mg g^{-1})	R^2	K_{id} (mg g^{-1} min$^{-1/2}$)	I (mg g^{-1})	R^2
15	10	0.0639	0.73	0.5660	0.3133	3.43	0.9997	0.0390	3.07	0.7268
	15	0.0550	0.86	0.6474	0.1361	3.03	0.9964	0.0877	2.24	0.9268
	20	0.0518	0.76	0.4098	0.3242	4.26	0.9995	0.0434	3.88	0.7702
25	10	0.0775	2.06	0.8158	0.1159	5.59	0.9996	0.1337	4.46	0.9771
	15	0.0775	2.06	0.8158	0.1185	5.08	0.9996	0.0399	4.88	0.4335
	20	0.0355	1.42	0.3839	0.1257	5.41	0.9980	0.0885	4.59	0.8507
50	10	0.0726	2.72	0.5092	0.1359	8.60	0.9995	0.1972	7.29	0.9393
	15	0.0726	2.72	0.5092	0.0861	7.84	0.9993	0.1708	6.38	0.9613
	20	0.0430	2.90	0.4903	0.0673	8.85	0.9994	0.1060	8.21	0.5944

[a]Lagergren pseudo-first-order; [b]Lagergren pseudo-second-order; C_0 – CIP initial concentration; T – temperature; q_e – the CIP amount adsorbed at equilibrium; k_1 – the rate constant of the first-order kinetic model; k_2 – the rate constant of the second-order kinetic model; K_{id} – intra-particle diffusion rate constant; I – parameter related to the thickness of the boundary layer; R^2 – correlation coefficient of the linear regression.

Table 16. Rate constant for the three studied kinetic models for the adsorption of CIP on MAG_{MW}-CLI and GO-MAG_{MW}-CLI.

MAG_{MW}-CLI										
C_0 (mg dm^{-3})	**T (°C)**	**LPFO**			**LPSO**			**Weber-Morris**		
		k_1 (h^{-1})	**q_e (mg g^{-1})**	**R^2**	**k_2 (g mg^{-1} min^{-1})**	**q_e (mg g^{-1})**	**R^2**	**K_{id} (mg g^{-1} min$^{-1/2}$)**	**I (mg g^{-1})**	**R^2**
15	10	0.0639	0.73	0.5732	0.3133	3.43	0.9995	0.1195	2.98	0.9544
	15	0.0541	0.86	0.6547	0.2445	2.86	0.9998	0.1368	2.89	0.9570
	20	0.0518	0.76	0.4097	0.3243	4.26	0.9999	0.0281	3.59	0.8711
25	10	0.0775	2.18	0.7801	0.1159	5.59	0.9999	0.2434	4.13	0.9877
	15	0.0775	1.04	0.8026	0.1310	5.08	0.9991	0.2342	4.22	0.9854
	20	0.0355	1.42	0.3478	0.1258	5.41	0.9969	0.2570	4.18	0.9693
50	10	0.0656	2.54	0.5107	0.1359	8.60	0.9999	0.5532	6.99	0.9899
	15	0.0726	2.01	0.5087	0.0861	7.84	0.9998	0.4761	7.61	0.9505
	20	0.0430	2.90	0.4803	0.0673	9.70	0.9979	0.2412	9.20	0.7534
GO-MAG_{MW}-CLI										
C_0 (mg dm^{-3})	**T (°C)**	**LPFO**			**LPSO**			**Weber-Morris**		
		k_1 (h^{-1})	**q_e (mg g^{-1})**	**R^2**	**k_2 (g mg^{-1} min^{-1})**	**q_e (mg g^{-1})**	**R^2**	**K_{id} (mg g^{-1} min$^{-1/2}$)**	**I (mg g^{-1})**	**R^2**
15	10	0.4360	0.80	0.5695	0.0678	3.92	0.9994	0.2158	2.14	0.9666
	15	0.0213	0.82	05285	0.1091	3.91	0.9998	0.2158	2.14	0.9832
	20	0.0198	0.79	0.4108	0.2102	3.91	0.9999	0.0464	3.59	0.6846
25	10	0.0113	3.06	0.7159	0.0875	6.06	0.9996	0.2812	3.68	0.9897
	15	0.0256	1.59	0.7050	0.1317	4.58	0.9999	0.4457	3.47	0.9840
	20	0.0298	1.96	0.4739	0.1977	4.89	0.9998	0.3114	5.53	0.9366
50	10	0.0658	7.27	0.5001	0.0196	15.43	0.9991	0.7355	9.30	0.9787
	15	0.6250	7.04	0.5904	0.0620	13.25	0.9998	0.6013	7.88	0.9691
	20	0.0398	6.98	0.3998	0.0329	12.45	0.9989	0.5731	9.47	0.9522

LPFO – Lagergren pseudo-first-order; LPSO – Lagergren pseudo-second-order; C_0 – CIP initial concentration; T – temperature; q_e – the CIP amount adsorbed at equilibrium; k_1 – the rate constant of the first-order kinetic model; k_2 – the rate constant of the second-order kinetic model; K_{id} – intra-particle diffusion rate constant; I – parameter related to the thickness of the boundary layer; R^2 – correlation coefficient of the linear regression.

The pseudo-second order model gives the best fit as judged by the R^2 values (Tables 15 and 16). This suggests that chemisorption occurs during the CIP adsorption. Additionally, the maximum calculated capacities obtained for the highest studied concentration: 9.78 mg CIP g^{-1} (at 10 °C), 8.85 mg CIP g^{-1} (at 20 °C), 9.70 mg CIP g^{-1} (at 20 °C), and 15.43 mg CIP g^{-1} (at 10 °C) for CLI, MAG_{CP}-CLI, MAG_{MW}-CLI, and GO-MAG_{MW}-CLI, respectively, correspond to the experimentally obtained values. The Lagergren's pseudo-second order rate constants (k_2) were in the range from 0.0196 to 0.4011 g mg^{-1} min^{-1} for all studied adsorbents. The k_2 values changed rather irregularly with temperature for all initial CIP concentrations. A similar phenomenon was reported for the CIP adsorption on clay minerals and γ-Al_2O_3 (Cheng *et al.*, 2018; Najafpoor *et al.*, 2019), which indicates the complexity of CIP adsorption mechanism.

Moreover, Tables 15 and 16 also showed that the analysis of the adsorption data by Weber-Morris's mass transfer model gave I parameter value higher than one, which suggests that the intra-particle diffusion is not the rate-limiting step in the CIP adsorption onto all studied adsorbents (Rajic *et al.*, 2010; Weber & Morris, 1962).

Adsorption isotherms

The adsorption isotherms are given in Figure 37. The maximum adsorption capacity of CLI, MAG_{CP}-CLI and GO-MAG_{MW}-CLI slightly increased with the temperature increase, while the capacity of MAG_{MW}-CLI is unchanged. At 20 °C the adsorption onto CLI increased from 4.39 mg CIP g^{-1} (for C_0 = 15 mg CIP dm^{-3}) to 12.52 mg CIP g^{-1} (for C_0 = 75 mg CIP dm^{-3}). Similar increases were observed for MAG_{CP}-CLI and MAG_{MW}-CLI: 4.26 and 3.86 mg CIP g^{-1} (for C_0 = 15 mg CIP dm^{-3}) to 12.59 and 11.08 mg CIP g^{-1} (for C_0 = 75 mg CIP dm^{-3}), respectively, suggesting that magnetic nanoparticles cover did not influence the CIP adsorption. On the other hand, the adsorption capacity of GO-MAG_{MW}-CLI increased from 3.68 mg CIP g^{-1} (for C_0 = 15 mg CIP dm^{-3}) to 13.01 mg CIP g^{-1} (for C_0 = 75 mg CIP dm^{-3}), indicating that the GO coverage increased the capacity of MAG_{MW}-CLI.

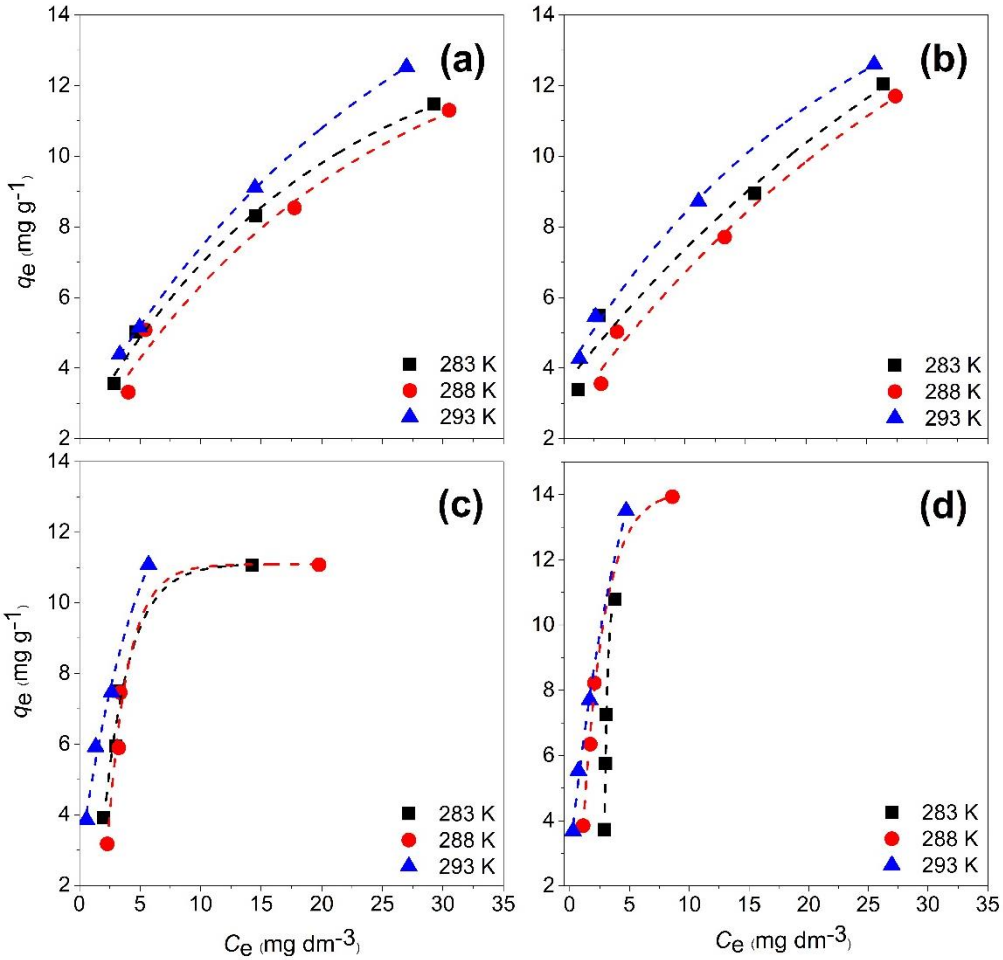

Figure 37. The adsorption isotherms for CIP on (a) CLI, (b) MAG_{CP}-CLI, (c) MAG_{MW}-CLI, and (d) GO-MAG_{MW}-CLI; q_e is the amount of the adsorbed CIP (mg per 1 g of adsorbent) and C_e is the CIP solution concentration at equilibrium.

The obtained equilibrium adsorption data were analysed using Langmuir and Freundlich isotherm models. The obtained results are summarized in Table 18. According to the obtained values of the linear regression correlation coefficients (R^2) (Table 17), the experimentally obtained equilibrium data can be described by both applied isotherm models. Generally, the Langmuir model gave a slightly better fit for the CIP adsorption on all studied samples. The results indicate that the adsorption mechanism includes the formation of monolayer on the energetically homogeneous CLI surface, with no interactions between the adjacent adsorbed CIP species (Langmuir, 1918). However, the adsorption at the highest studied temperature for pristine CLI and MAG_{CP}-CLI is better described by Freundlich than by Langmuir model. In contrast to Langmuir, the Freundlich model implies the adsorption on energetically heterogeneous sites, whereby the formation of multilayer and the interaction between the adsorbed CIP species are not excluded. According to the maximum capacities calculated by Langmuir model, the highest value was obtained for GO-MAG_{MW}-CLI (47.91 mg CIP g^{-1} at 15 °C) and the lowest for MAG_{CP}-CLI (13.27 mg CIP g^{-1} at 10 °C). Moreover, the maximum capacities obtained for the MAG_{CP}-CLI and MAG_{MW}-CLI at 15 °C are 15.86 and 21.25 mg CIP g^{-1}, respectively, indicating a slightly higher adsorption capacity for CIP on magnetic clinoptilolite synthetized by MW-assisted method. This could be assigned to the difference in

binding patterns of CIP on the Fe_3O_4 and γ-Fe_2O_3 caused by the heterogeneity of adsorption sites on their surface (e.g., the site energy distribution) (Lin & Lee, 2020).

The Langmuir equilibrium constant (b_L) can be used as an indicator for the strength of interaction between the CIP species and CLI surface. The larger b_L value indicates stronger CIP-CLI interactions (Langmuir, 1918). The obtained b_L values for all studied samples (Table 18) indicate that the CIP has the highest affinity towards CLI samples at 15 °C, as well as that the CIP interactions are strongest with MAG_{CP}-CLI. On the other side, the Freundlich constant K_f is in linear correlation with the adsorption capacity of adsorbent, which suggests higher adsorption capacity with higher K_f.

The favourability of the adsorption process under specific experimental conditions can be expressed in terms of dimensionless equilibrium parameter – R_L or separation factor:

$$R_L = \frac{1}{1 + b_L C_0} \tag{23}$$

The isotherm classification based on the value of R_L is given in Table 17 (Veloso *et al*., 2020) and the calculated R_L values at studied initial CIP concentrations are shown in Figure 38. The obtained results indicate that the CIP adsorption of CIP on the surface of the CLI samples is favourable. The lower values of R_L at higher initial CIP concentrations show that the CIP adsorption is also favourable at higher concentrations. Moreover, the Freundlich constant *n* can also indicate the type of the adsorption process and classify its favourability. Since the obtained values of this parameter are in range 1.30–2.81, the CIP are bound to the CLI surface with low free energies and the adsorption is classified as a highly favourable (Veloso *et al*., 2020). Due to the CLI lattice porosity and different features of coating materials (i.e. non-stoichiometric maghemite structure, GO framework), the surfaces of CLI-based adsorbents can be characterized as heterogeneous rather than homogeneous. Based on these facts, it can be assumed that several different types of adsorbent-adsorbate interactions are responsible for the CIP adsorption onto CLI-based adsorbents.

Table 17. R_L-values isotherm classification.

R_L value	Isotherm
$R_L = 0$	Irreversible
$0 < R_L < 1$	Favourable
$R_L = 1$	Linear
$R_L > 1$	Unfavourable

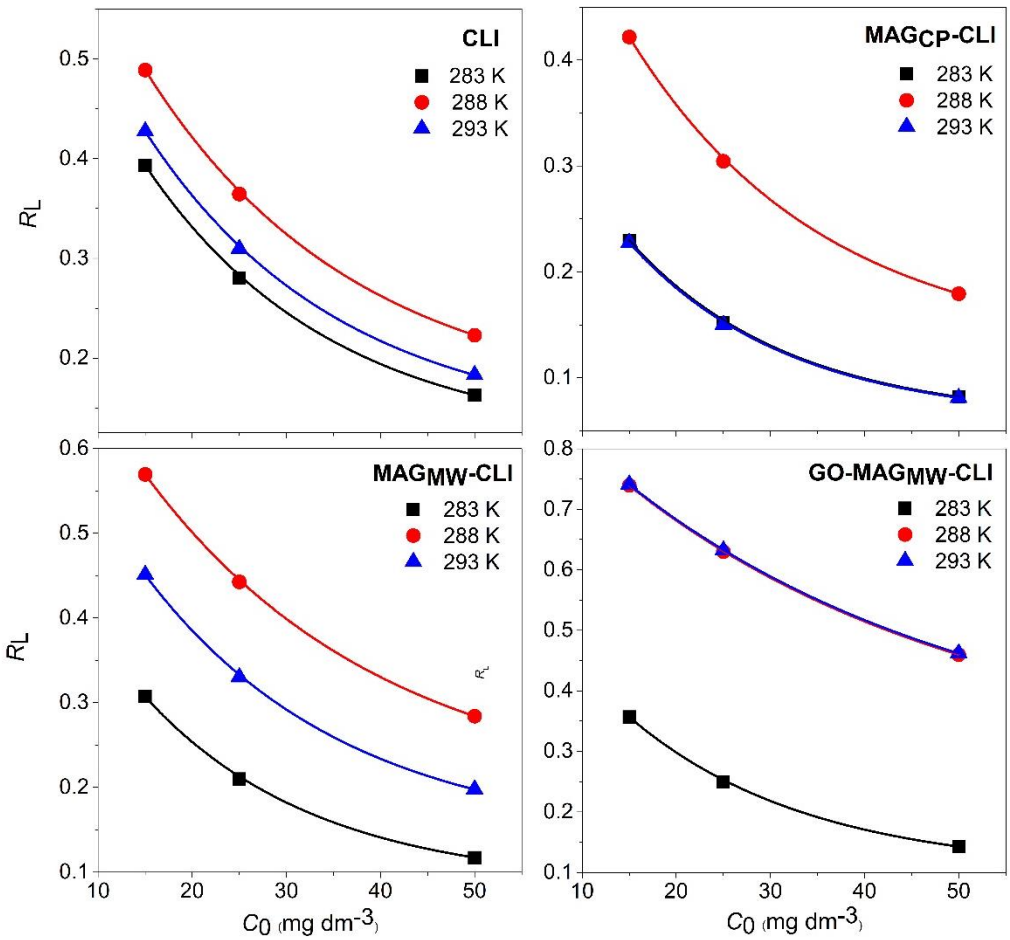

Figure 38. Separation factor (R_L) obtained from the Langmuir isotherm model as a function of initial CIP concentration for different temperatures.

Table 18. The isotherm parameters obtained for the adsorption of CIP on CLI-based adsorbents.

		Langmuir isotherm parameters			Freundlich isotherm parameters		
Adsorbent	***T*, °C**	**q_{max}, mg g^{-1}**	**b_L, dm^3 mg^{-1}**	**R^{2*}**	**K_f, mg g^{-1} (dm^3 mg^{-1})$^{1/n}$**	***n***	**R^{2*}**
CLI	10	14.96	0.1028	0.9944	2.24	2.05	0.9924
	15	16.31	0.0697	0.9877	1.73	1.80	0.9804
	20	17.30	0.0893	0.9909	2.34	1.97	0.9993
MAG_{CP}-CLI	10	13.27	0.2235	0.9834	3.34	2.62	0.9831
	15	15.86	0.0914	0.9827	2.16	1.97	0.9809
	20	14.25	0.2263	0.9870	3.85	2.81	0.9981
MAG_{MW}-CLI	10	14.91	0.1505	0.9764	2.52	1.86	0.9679
	15	21.25	0.0504	0.9999	1.44	1.51	0.9792
	20	21.00	0.0812	0.9990	2.05	1.58	0.9967
GO-MAG_{MW}-CLI	10	17.43	0.1201	0.9779	2.28	1.61	0.9148
	15	47.91	0.0235	0.9781	1.47	1.30	0.9707
	20	41.78	0.0233	0.9420	1.32	1.36	0.9192

q_{max} – maximum amount of the CIP adsorbed; b_L – Langmuir adsorption equilibrium constant related to the adsorption energy; K_f, n – Freundlich constants related to the maximum adsorption capacity and adsorption intensity (heterogeneity factor), respectively.
*R^2 was obtained by linear fitting using Origin 9 software.

4.3. CIP leaching experiments

Leaching of the adsorbed CIP from saturated CLI and MAG_{CP}-CLI was investigated by treating them with NaCl for 24 hours. Results showed that 20.6% of CIP was released from CLI, which contained 20.2 mg CIP g^{-1}, while only 4.4% was released from MAG_{CP}-CLI, with 22.1 mg CIP g^{-1}. These results indicate that: (i) magnetite coverage prevents the CIP leaching, and that (ii) the CIP adsorption process is mostly irreversible. The protection of the magnetite coverage may be due to an interaction between the carboxylic groups of the CIP and magnetite particles, forming an inner-sphere complex (Rakshit *et al*., 2013). Moreover, the fact that only 20% of the adsorbed CIP can be replaced by Na^+ from CLI suggests a strong interaction between CIP and the CLI surface.

4.4. Study of antibacterial activity of CIP-containing CLI

To ensure that managing the spent adsorbents is cost-effective, the antibacterial activity of the CIP-containing CLI and MAG_{CP}-CLI was also tested.

Previous studies have shown that CLI by itself does not exhibit antibacterial activity against the tested bacterial strains (Hrenovic *et al*., 2012). As shown in Figure 39, CIP has a potent antibacterial effect towards both *E. coli* and *S. aureus*, which is consistent with the existing literature data (Chalkley & Koornhof, 1985; Simões *et al*., 2008). In addition, based on the inhibition zone, both CLI-CIP and MAG_{CP}-CLI-CIP exhibit strong antibacterial activity. The antibacterial effect of the CIP and the spent adsorbents is more pronounced towards *E. coli* than to *S. aureus*. This can be attributed to differences in the cell wall structure and composition of Gram-negative and Gram-positive bacteria (Berlanga *et al*., 2004; Mohsen *et al*., 2020). It is worth noticing that the concentration of CIP used in this assessment was 100 times higher than that present in CLI-CIP and MAG_{CP}-CLI-CIP. These results indicate a significant finding: possibility of use of CIP-containing CLI in tertiary stage of water treatment – disinfection.

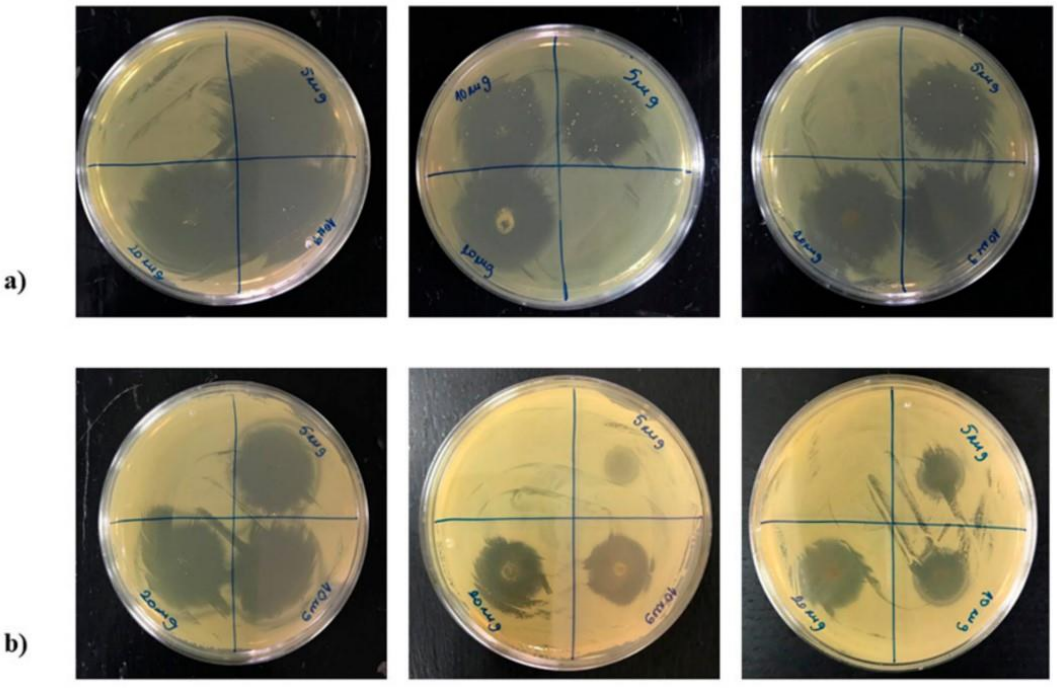

Figure 39. The antibacterial activity of CIP, CLI-CIP and MAG_{CP}-CLI towards (a) *E. coli*, and (b) *S. aureus*. Initial number of bacteria (t_0): *E. coli*= 1.4 ×10^9; *S. aureus*= 1.2 ×10^9 CFU cm^{-3}.

4.5. Regeneration by plasma treatment

4.5.1. Optimization of plasma process parameters

To determine the optimal conditions for efficient regeneration of CLI and CLI-based adsorbents after CIP adsorption, a range of operational parameters was investigated. Table 19 presents the results of CLI-CIP^{200} regeneration for three different combinations of plasma treatment parameters. The results showed that reducing the treated sample mass improved the recovery of CLI capacity for CIP, decreasing the LAE parameter for around 2%. This can be attributed to a higher effective area of particles in the sample exposed to plasma. Moreover, decreasing the electrode gap (*d*) from 4 to 2 mm (configuration 2a) also enhanced the CLI recovery process to the same extent as reducing the treated sample mass. Reduction in the electrode distance decreased the active plasma volume, which increased the total plasma current and reactive species density, leading to a slight increase in plasma power. Since the smallest reduction in adsorption efficiency was obtained with d = 2 mm, this electrode gap was used to further study the potential of atmospheric NTP treatment for the CLI-based adsorbent regeneration.

Table 19. Parameters of the plasma treatment systems together with the percentage of restored adsorption capacity.

Configuration	Plasma parameters			Sample	LAE[e] (%)
	S^a (cm^2)	d^b (mm)	$P_{mean}{}^c$ (W)	m^d (g)	
1a		4	1.1	0.25	14.2
1b	18.1	4	1.1	0.10	12.3
2a		2	1.3	0.10	10.0
2b	37.2	2	2.5	0.20	18.2

Treatment time: 20 min.
[a]Electrode surface; [b]plasma discharge gap; [c]applied system power; [d]sample mass; [e]loss of adsorption efficiency.

Furthermore, to enable the treatment of a larger mass in one iteration, the electrode surface was expanded to approximately double its size (S_2 = 37.2 cm^2), which also doubled the system's mean power. Consequently, the sample mass was also increased two-fold.

The results obtained by treating 0.20 g of CLI-CIP^{200} using the source configuration with S_2 electrode surface (configuration 2b) showed a difference in LAE of around 8% compared to the most optimal configuration 2a (Table 19). A slightly higher value of LAE after increasing the plasma source surface could be a consequence of random experimental errors related to the environment. Despite this difference, the result proved to be satisfactory and support the fact that, for the range of investigated parameters, the plasma process is scalable with respect to the active plasma area and treated sample mass. This is significant for potentially scaling up of the regeneration process.

In addition, monitoring the voltage and current during each plasma treatment provided additional insight into the amount of remaining water in the samples. Particularly, a significant change in the humidity level in the active plasma volume is accompanied by a drop in discharge current and power (Abdelaziz *et al*., 2018; Kim *et al*., 2018b; Zhou *et al*., 2021). These results remained unchanged in the case of CLI treatments, indicating that the amount of residual water in the samples remained constant. Thus, all treatments were consistent and reproducible.

4.5.2. Plasma characterization

Electrical measurements of the plasma source

Figure 40 displays the time-varying plasma current and voltage signals at the powered electrode recorded under treatment conditions (*V*p = 23 kV, peak-to-peak). The plasma current signal is corrected to the displacement current. The displacement current is estimated assuming its capacitive nature and then calculated by taking the derivative of the applied voltage signal using the capacitance of the source that is realistically measured.

The voltage signal has a sinusoidal shape, while the current signal is periodic with distortions in both the positive and negative parts of the period and narrow, spiked shape at maximum and minimum values. In the positive part of the signal, structures with peaks appear in the current signal, possibly due to the occasional occurrence of filaments – micro-discharges among established diffuse surface discharge (Brandenburg, 2018; Shahbazi Rad & Abbasi Davani, 2020).

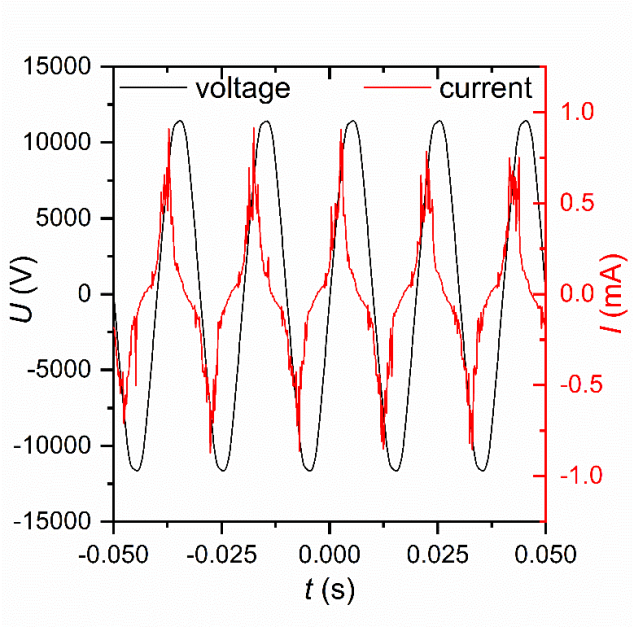

Figure 40. Waveforms of electrode voltage (left axis) and plasma current (right axis) of the SDBD source in air at atmospheric pressure recorded at 1.3 W. The current signal is shown without the displacement current.

Optical emission spectroscopy

Figure 41 illustrates the emission spectrum of air SDBD plasma obtained without a sample in the near ultraviolet-visible region (200–900 nm). The spectrum provides a qualitative information about the existence of excited chemical species present in the discharge. As expected for air plasma, the most intense lines recorded corresponded to the N_2 Second Positive System (SPS) band. The obtained peak intensities for the First Negative System (FNS) of N_2 and OH radicals are also visible and are present due to the certain humidity in the ambient air, where the plasma operates. In addition, a weak band of the First Positive System (FPS) of N_2 was observed in the visible part of the spectrum (Lofthus & Krupenie, 1977). According to the literature data, the main active species present in such SDBD air plasma discharge responsible for the degradation of organic molecules were found to be atomic oxygen (O), ozone (O_3) (Sakiyama *et al.*, 2012; Shang *et al.*, 2020), hydrogen peroxide (H_2O_2), hydroxyl radicals (•OH), as well as peroxynitrites and nitrogen oxides (Sarangapani *et al.*, 2019). However, apart

from the •OH, other species do not have emission in the range of the obtained OES spectrum, and thus they cannot be identified from the recorded data.

To detect any possible emission from CIP decomposition products that were dispersed into the gas phase and excited in the plasma, the comparison was performed between the spectra obtained without CLI and with CLI and CIP-CLI samples. However, both spectra showed the same lines as in Figure 41, indicating that no additional emission from the decomposition products of CIP (or eventually from CLI) could be detected in the investigated spectral range.

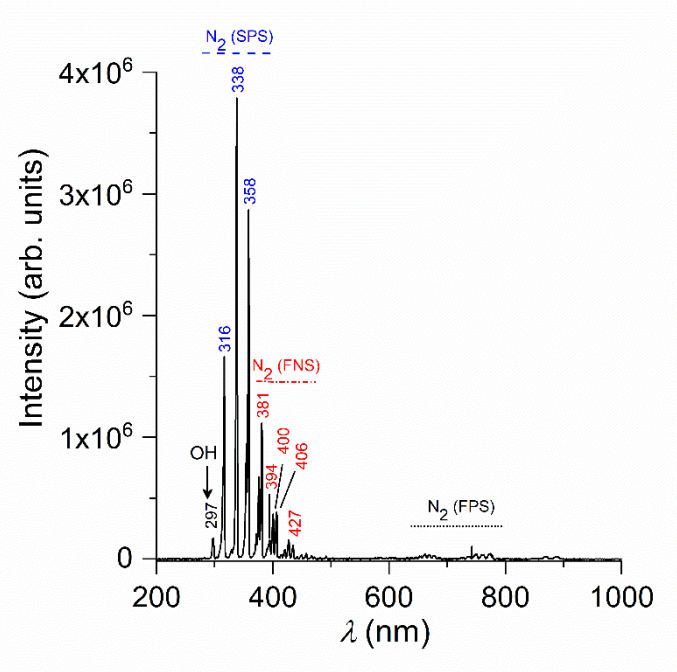

Figure 41. The optical emission spectrum from the air SDBD source at atmospheric pressure, recorded at treatment conditions (P = 1.3 W, Vp = 23 kVp-p). Line intensities are corrected for the spectral efficiency of the detector.

4.5.3. Plasma regeneration of spent adsorbents

Regeneration of adsorbents with high CIP loading (adsorbent-CIP^{200})

The effectiveness of the NTP treatment in the regeneration of the CLI-based adsorbents is expressed by the recovery of adsorption properties. Figure 42 shows the removal efficiency and adsorption capacity of pristine CLI and GO, GO-CLI and GO-MAG$_{MW}$-CLI for CIP through five adsorption/NTP regeneration cycles.

The results of NTP regeneration treatments of GO-CIP^{200} (Figure 42b) shows a stable removal efficiency for CIP of around 96.11% through five adsorption cycles. An abrupt decrease in the adsorption capacity of pristine GO for around 20 mg g^{-1} was observed after the second adsorption cycle and remained constant in the subsequent cycles. However, the decrease in adsorption capacity did not significantly affect the CIP removal efficiency, indicating the possible reduction of GO (Neustroev, 2018) sheets or change in its functional groups (addition of new) after exposure to air plasma. A treatment of GO in hydrogen plasma led to oxygen transfer accompanied by formation of new C–O and CO= bonds. The tested GO showed better efficiency in catalytic tests of 1-octene hydroisomerization and hydrogenation of α-methyl-styrene (Magureanu *et al*., 2021).

On the other hand, the reusability test showed significant decrease in removal efficiency of CLI, GO-CLI and GO-MAG_{MW}-CLI after fifth adsorption cycle (Figure 42a, c, d). The CIP removal efficiency decrease rather gradually during the cycles with a reduction in adsorption efficiency to almost 50% of its initial value. The same trend was observed for the adsorption capacity. The low reusability of CLI, GO-CLI and GO-MAG_{MW}-CLI may be related to a high CIP loading and partial blocking of adsorbent's pore by CIP plasma by-products, as well as to lower access of plasma species to a part of adsorbed molecules due to modification layers.

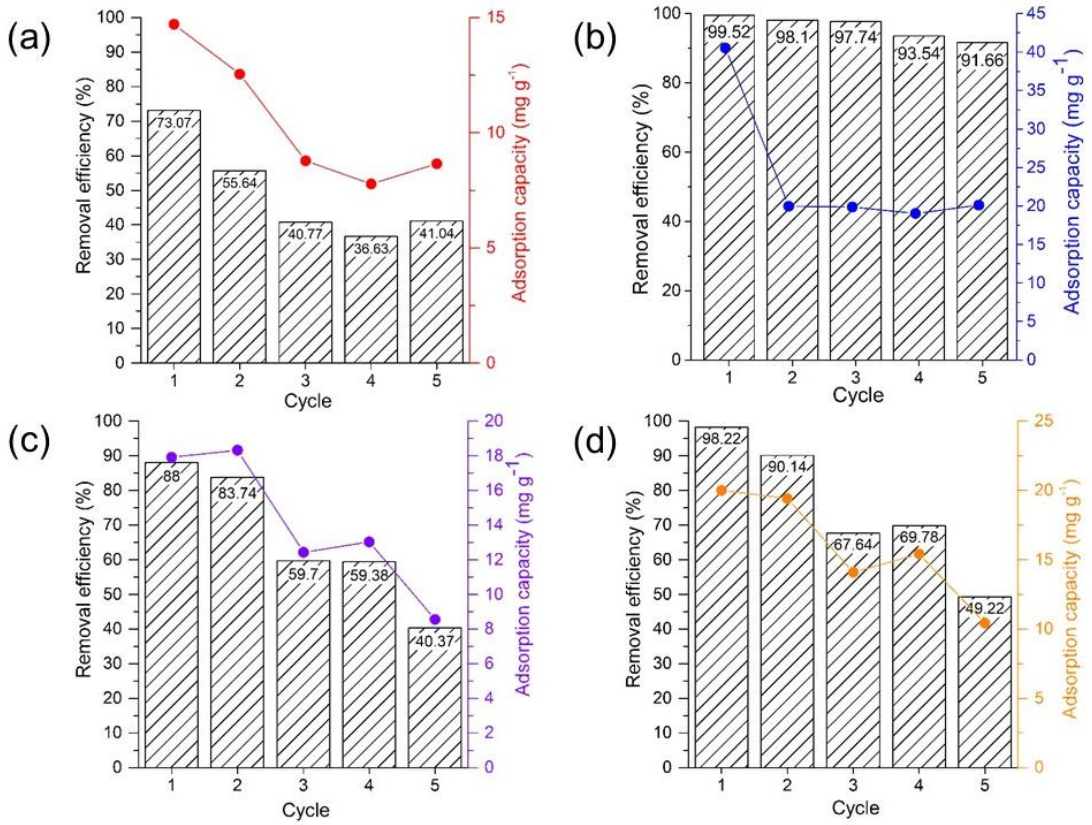

Figure 42. Reusability tests of (a) CLI-CIP^{200}, (b) GO-CIP^{200}, (c) GO-CLI-CIP^{200}, and (d) GO-MAG_{MW}-CLI-CIP^{200} through five cycles.

Regeneration of clinoptilolite with lower CIP loading (CLI-CIP^{25})

The high initial CIP concentration of 200 mg dm^{-3} used in the adsorption/regeneration tests could affect the efficiency of the regeneration process. In order to optimize the regeneration process for lower CIP concentrations, and to potentially increase the reusability, the NTP regeneration test of CLI with 2.3 mg CIP g^{-1}. The initial concentration of 25 mg dm^{-3} used in for the CLI loading with CIP is also more or realistic concentration that could be find in wastewater.

The results of the CLI-CIP^{25} reusability tests during the adsorption cycles are shown in Figure 43. The removal efficiency of CIP did not change significantly during the five adsorption cycles. The first adsorption cycle with the CIP removal efficiency of 87 % included pristine CLI. Following the first cycle, both removal efficiency and CLI adsorption capacity remained relatively consistent over the next three cycles (87.50 ± 3 % and 2.34 ± 0.01 mg g^{-1},

respectively). Subsequently, the removal efficiency of CIP decreased to 80 % in the last cycle accompanied by a minor reduction in CLI capacity (2.17 mg g^{-1}).

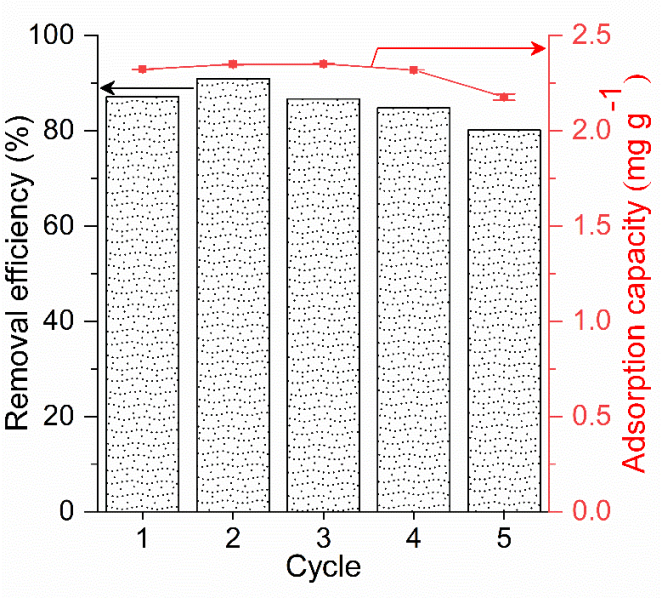

Figure 43. Reusability tests of CLI for the removal of CIP through five cycles (bar graph – removal efficiency (%), symbol-line graph – adsorption capacity (mg g^{-1}), C_0 = 25 mg dm^{-3}, adsorbent dosage = 10 g dm^{-3}, pH = 5, and contact time of 5 min).

Characterization of plasma regenerated clinoptilolite

The preservation of CLI's aluminosilicate lattice after plasma treatment has been confirmed by the PXRD measurements. The obtained results are in accordance with the literature data (de Velasco-Maldonado *et al*., 2018; Mirzaei *et al*., 2019). The crystallinity of CLI was tested after the first (CLI-CIP_PL1) and fifth (CLI-CIP_PL5) regeneration cycle. The obtained PXRD diffractograms are given in Figure 44, indicating that the plasma did not affect CLI's structural features even after 5 regeneration cycles. The obtained XRD reflections matched the natural clinoptilolite pattern (Favvas *et al*., 2016). Similar findings were reported for the low-pressure oxygen plasma activation of zeolite-A (Fahmy *et al*., 2019) and clinoptilolite (de Velasco-Maldonado *et al*., 2018), where the plasma treatment increased its adsorption capacity for cadmium ions and organic dyes.

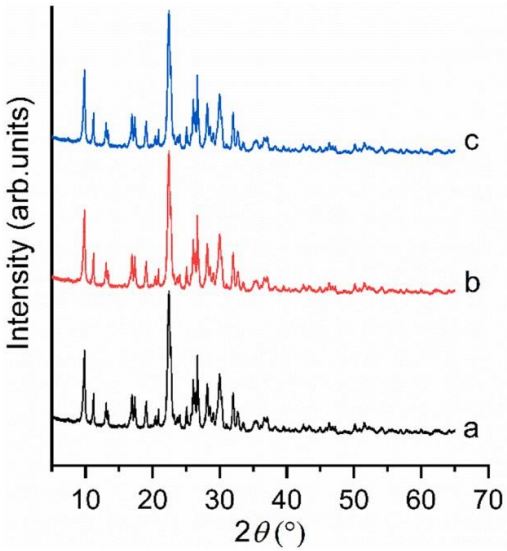

Figure 44. Diffractograms of (a) CLI, (b) CLI-CIP_PL1, and (c) CLI-CIP_PL5.

The impact of NTP on the textural properties of the spent adsorbent was examined using the N_2 adsorption/desorption experiments at –196 °C. The results, presented in Figure 45, indicate that the isotherms belong to the type IV per the IUPAC classification, which is characteristic of mesoporous solid materials (Sing, 1982). The presence of hysteresis loops of type H3, which is typical for clinoptilolite material, suggests that it exists in the form of non-rigid aggregates of plate-like particles, resulting in slit-shaped pores (Lowell *et al*., 2006). The results further demonstrate that CIP-CLI_PL1 had a greater N_2 adsorption capacity than the other samples due to an increased number of mesopores after plasma regeneration treatment. This could be also due to impurities slowing the diffusion of N_2 molecules through the CLI and CIP-CLI structures, thereby hindering their access to the clinoptilolite pore system.

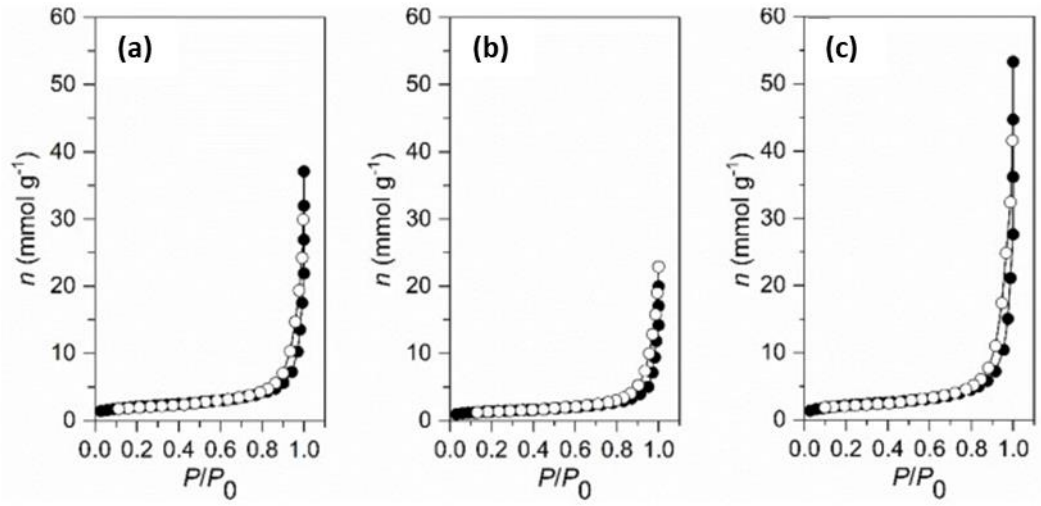

Figure 45. N_2 adsorption/desorption isotherms for (a) CLI, (b), CLI-CIP[25], and (c) CLI-CIP_PL1. Solid symbols – adsorption, open symbols – desorption.

The specific surface area of CLI was determined to be 32 $m^2\ g^{-1}$ using the BET equation, which is similar to the already reported value for raw clinoptilolite (Garcia-Basabe *et al*., 2010; Jevtić *et al*., 2014). The textural properties of CLI-CIP[25] (2.32 mg CIP g^{-1}) before and after NTP

treatment were also found to be similar to that of raw CLI (Table 20). Furthermore, the plasma treatment did not have a significant effect on the pore size distribution (Figure 46).

Table 20. Textural properties of pristine CLI, CIP-loaded CLI, and CLI after plasma treatment.

Sample	S_{BET} (m^2 g^{-1})	V_{mic} (cm^3 g^{-1})	D (nm)
CLI	33	0.0029	9
CLI-CIP[25]	29	0.0027	9
CLI-CIP_PL1	27	0.002	11

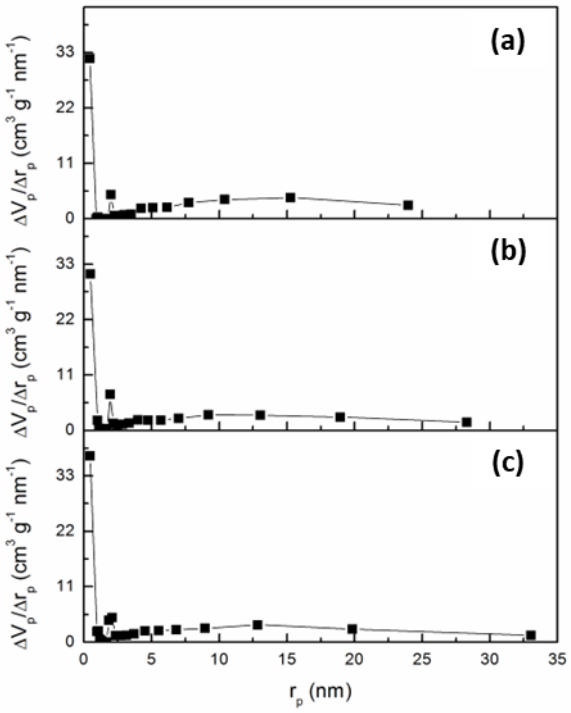

Figure 46. Pore size distribution of (a) CLI, (b), CLI-CIP, and (c) CLI-CIP_PL1.

The XPS analysis was performed to get an insight into the surface properties of CLI after plasma treatment. Figure 47 displays a typical XPS survey spectra from the surface of CLI, CLI-CIP, CLI-CIP_PL1 and CIP samples. The peaks of elements O, Fe, Si, Al, Ca, Mg and K were identified in XPS spectra originating from the CLI matrix. Additionally, carbon detected in CLI spectra (Figure 47a) originated from the contamination layer due to sample handling in air. The binding energy found in the carbon C 1 s XPS spectra of CLI-CIP (Figure 47b) and CLI-CIP_PL1 (Figure 47c) is 284.7 eV, and that can be assigned to C–C and C–H bonds (Tam et al., 2019). The XPS spectrum of CIP (Figure 47d) displayed F, N, C and O peaks. The F and N peaks are also evident in the spectra of CLI-CIP and CLI-CIP_PL1 (Figures 47b and 47c), confirming the presence of CIP. The intensity of F and N peaks was lower in the spectrum of CLI-CIP_PL1 than in CLI-CIP due to plasma treatment.

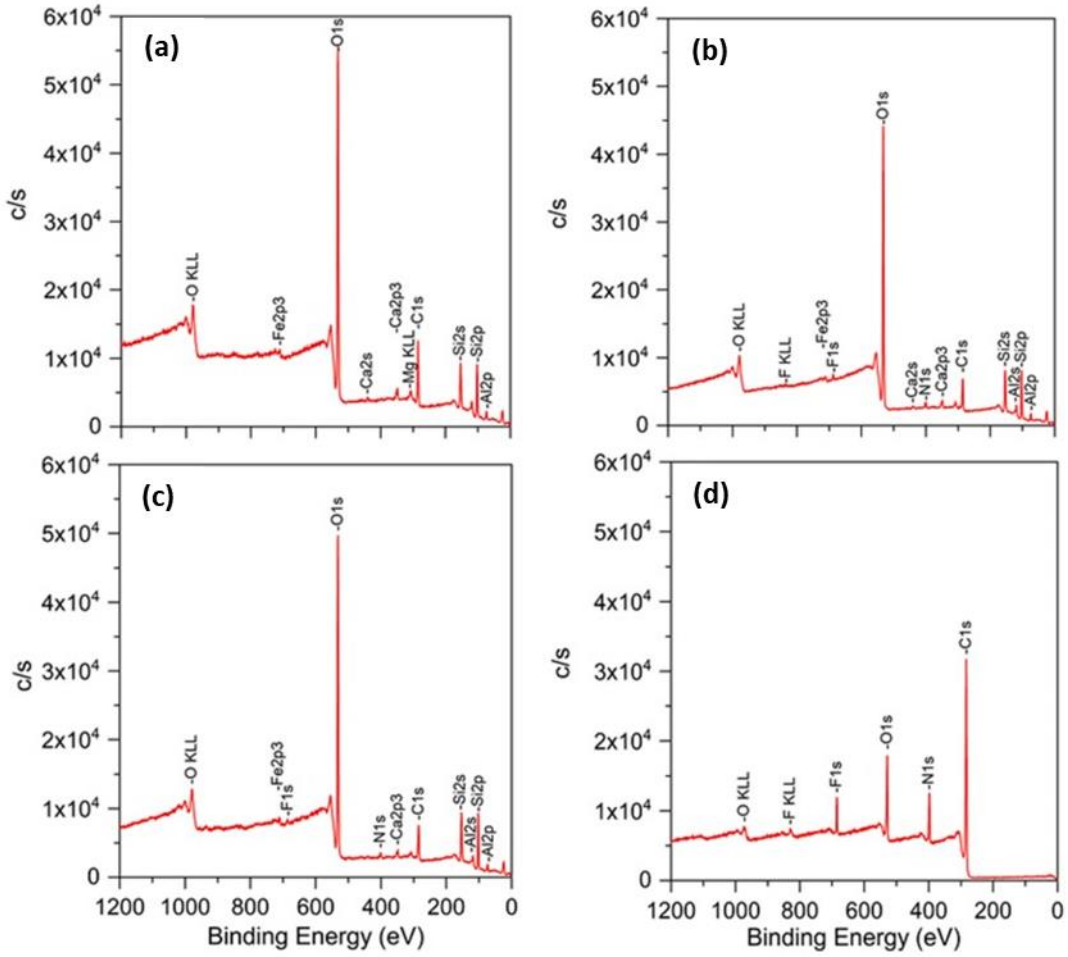

Figure 47. XPS survey spectra from the surface of (a) CLI, (b) CLI-CIP, (c) CLI-CIP_PL1, and (d) CIP.

Moreover, Figure 48 shows that the concentration of carbon was significantly higher for CLI-CIP and CLI-CIP_PL then for pristine CLI, suggesting that the:

1) CIP is present on the CLI, which results in an increase of C concentration onto CLI surface,
2) carbon concentration is lower for about 50% for the plasma treated CLI than for CLI-CIP, and
3) certain amount of carbon (≈ 10%) remained in the CLI lattice after the treatment, suggesting that the NTP did not completely remove the organic species present in CLI.

It should be noted that the Ar-ion sputtering process used on powder samples does not remove the surface layer uniformly on all particles because of the shadowing effect, caused by uneven sample surfaces. This effect could be the main reason why carbon was still present after different sputtering times, indicating that the particles have a carbon-based coating in the non-sputtered area. However, the carbon concentration in the XPS profiles is believed to represent the residual level of CIP after NTP treatment. Due to their low concentrations, the concentration of F and N was not followed during XPS depth profiling on the CLI-CIP and CLI-CIP_PL1 samples.

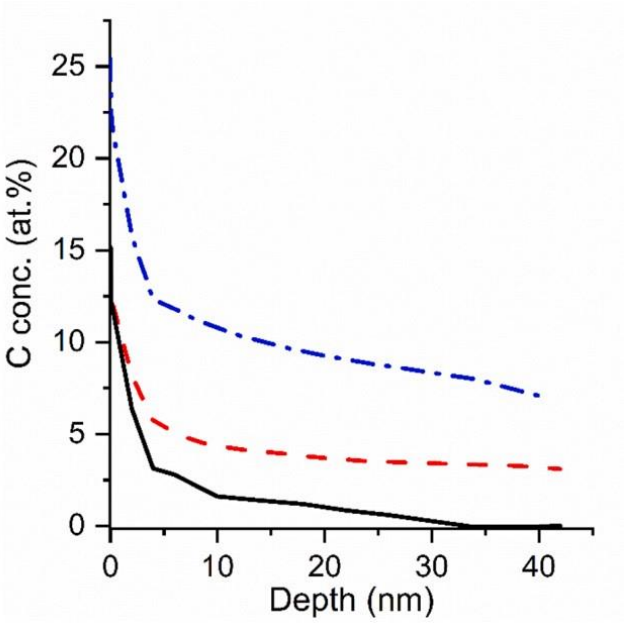

Figure 48. XPS depth profile for carbon obtained on the CLI, CLI-CIP and CLI-CIP_PL1 samples.

Mechanism of CLI regeneration by plasma

The results from several adsorption cycles demonstrated that plasma treatment effectively regenerates the adsorbent, resulting in recovered adsorption capacity. To assess the mechanisms involved in the regeneration process after exposure of the CIP-containing adsorbent to the plasma, three types of processes that could possibly play a role in the treatment were analysed as follows; (i) heating of the sample in the active plasma volume either due to gas heating or discharge current flow through the sample; (ii) the physical effects of plasma-generated reactive species on the CIP molecules; and (iii) the chemical interactions between reactive species and CIP molecules.

According to the literature data, CIP is thermally stable in the temperature range 25–50 °C. Decomposition of the CIP molecule starts at 50 °C and finishes at around 750 °C in three successive stages. The first stage includes the loss of CO molecules, followed by a loss of [$C_4H_8N_2H_2$ + CO]. The last stage is attributed to the removal of the residual drug ($C_{11}H_8FNO$) (Sadeek *et al.*, 2011; Valdés *et al.*, 2017).

The DBD plasma sources produce chemically reactive environment at nearly room-temperature since they are designed to prevent the emergence of higher currents that can heat up the gas and the sample. To exclude any thermal effect of the plasma treatment, the gas temperature inside the plasma volume directly at the position of the sample was measured during the sample treatment. It was found that the measured temperature never exceeded 30 °C and increased by an average of 2.5 °C during a 20-minute treatment. Based on the abovementioned information about the thermal decomposition of CIP, the temperature achieved by SDBD plasma was not high enough to induce thermal degradation of CIP.

The air SDBS plasma source operating at atmospheric pressure produces various reactive species, such as NO_X, ozone, hydroxyl radicals, and hydrogen peroxide that can chemically interact and participate in the CIP molecule degradation. Considering the presented results and

literature data, it is likely that the main mechanisms involved in the decomposition of CIP by air plasma are (Aggelopoulos *et al.*, 2020; Sarangapani *et al*., 2019):

- hydrogen attacking the piperidine ring followed by a recombination with OH, and
- ozone attacking the carboxyl group of the quinolone moiety followed by subsequent attack of the piperazinyl substituent.

Although these studies manly focused on plasma degradation of CIP dissolved in a liquid phase, the penetration of reactive species from the active plasma volume into the liquid creates similar environments as applied plasma treatment. For example, •OH are present in both the gas phase plasma and inside plasma-treated liquid sample. However, the concentration of O_3 is higher in the gas phase due to its low solubility in water, so its influence is more pronounced in gas phase treatment compared to liquid sample treatment. Additionally, fast species produced in plasma also physically scatter CIP molecules.

Considering the analysis, it seems likely that CIP was initially broken down into different intermediates species of masses ranging from 300 to 420 Da, which are then partially mineralized under exposure to NTP. Volatile by-products of these reactions were removed immediately during the plasma treatment, while others likely remain on the surface of the CLI and are detached in the following adsorption cycle. Some of the degradation products are highly polar and water-soluble, which makes them resistant to further oxidation (Aggelopoulos *et al*., 2020).

5. CONCLUSIONS

From all presented results, it can be concluded that natural Ca-rich-clinoptilolite from Serbian deposit Slanci can be transformed into efficient, environmentally friendly, and economically feasible adsorbents for application in wastewater treatment.

Clinoptilolite's surface was functionalized by iron oxide nanoparticles and graphene oxide by (i) conventional co-precipitation and (ii) non-conventional microwave-assisted method. The obtained magnetic samples were covered by graphene oxide, giving efficient adsorbents for ciprofloxacin.

Detailed characterization of the prepared samples showed the presence of nano-iron oxide particles onto clinoptilolite surface. The procedure of the preparation of the particles influenced crystallization of nano oxide phases. Both procedures led to the materials of similar magnetic properties. Moreover, graphene oxide coating was successfully immobilized onto the obtained magnetic CLI.

The study of adsorption capacity for ciprofloxacin was optimized by the response surface methodology through central composite factorial design. According to the statistical analysis, the considered levels of the initial ciprofloxacin concentration and pH have the most significant effect on the adsorption. The highest adsorption capacity was achieved under the optimal conditions: initial ciprofloxacin concentration of 48.47 mg dm^{-3}, pH = 5.10 at 24.78 °C within 19.20 minutes.

From adsorption experiments, the following conclusions can be derived:

- Adsorbed amount of ciprofloxacin increased with increasing the initial ciprofloxacin concentration.
- The ratio of 1:250 was found as an optimal mass: volume ratio for ciprofloxacin adsorption.
- The adsorption mechanism includes electrostatic interactions and ion exchange reaction between the cationic form of ciprofloxacin and negatively charged clinoptilolite surface.
- Ciprofloxacin adsorption is influenced by clinoptilolite modification. Graphene oxide-containing magnetic clinoptilolite shows the highest adsorption capacity.
- The adsorption is fast process. More than 80% of the maximum adsorption capacity was achieved within the first 10 minutes for the temperature range of 10 to 20 °C.
- Langmuir isotherm model can best describe ciprofloxacin adsorption, and the adsorption kinetics follow the pseudo-second-order kinetic model.

The impregnation of clinoptilolite by magnetic iron oxide nanoparticles does not improve the adsorption ability and capacity of clinoptilolite but brings magnetisms which allows easier clinoptilolite separation after saturation of the adsorbents by ciprofloxacin.

The results of leaching experiments suggest that ciprofloxacin is strongly adsorbed. Magnetic coverage protects ciprofloxacin saturated adsorbent from leaching through the interaction of carboxylic groups of the adsorbed ciprofloxacin and iron oxide particles onto clinoptilolite.

Ciprofloxacin-containing clinoptilolite showed strong antibacterial activity towards pathogens (*E. coli* and *S. aureus*). This finding recommends ciprofloxacin-containing clinoptilolite for use in a tertiary stage of water treatment (in disinfection).

The following conclusions can be derived from reusability experiments:

- The plasma treatment performed at atmospheric pressure in air regenerated the spent clinoptilolite adsorbent in a high rate (about 90%). The adsorption capacity of clinoptilolite remains stable after the five adsorption/regeneration cycles with less than 7% difference in the adsorption efficiency between the first and fifth adsorption cycles.
- The plasma treatment did not affect clinoptilolite crystallinity nor its textural properties. It was confirmed that plasma treatment decomposed majority of the adsorbed ciprofloxacin with about 10% of carbon left immobilized on the surface.
- Plasma treatment shows to be effective in ciprofloxacin-containing graphene oxide with more than 90% of the initial capacity recovered after five regeneration cycles. A good potential in magnetic and graphene oxide-loaded clinoptilolite regeneration was also observed.
- Performed electrical characterization of plasma source proved the stability of plasma properties in different treatments with a power consumption of 2.5 W. Optical emission measurements showed typical spectrum of an air plasma with OH radicals and excited N_2 species.
- The obtained results of the scaling-up the plasma source showed that doubling the treatment area and sample mass gave repeatable results.

Finally, all the obtained results clearly indicate that natural clinoptilolite from Slanci deposit can be converted to an efficient, low-cost, and environmentally friendly adsorbent for antibiotic ciprofloxacin. The spent adsorbent can be regenerated efficiently by an innovative plasma technique, which was tested and demonstrated for the first time.

All the obtained results point to the final conclusion that adsorption represents an effective approach for removing the antibiotic ciprofloxacin from model water solution. Furthermore, in combination with plasma, it can be a good basis for the design of a water treatment plant. Moving forward, it is essential for future research to focus on adsorption processes within complex water matrices to accurately simulate real wastewater conditions. This will enable a more comprehensive understanding of the efficacy and practical implementation of this method.

6. REFERENCES

Abdelaziz, A. A., Ishijima, T., & Seto, T. (2018). Humidity effects on surface dielectric barrier discharge for gaseous naphthalene decomposition. *Physics of Plasmas*, *25*(4).

Ackley, M. W., Rege, S. U., & Saxena, H. (2003). Application of natural zeolites in the purification and separation of gases. *Microporous and Mesoporous Materials*, *61*(1–3), 25–42.

Aeenjan, F., & Javanbakht, V. (2018). Methylene blue removal from aqueous solution by magnetic clinoptilolite/chitosan/EDTA nanocomposite. *Research on Chemical Intermediates*, *44*(3), 1459–1483.

Aggelopoulos, C. A., Hatzisymeon, M., Tataraki, D., & Rassias, G. (2020). Remediation of ciprofloxacin-contaminated soil by nanosecond pulsed dielectric barrier discharge plasma: Influencing factors and degradation mechanisms. *Chemical Engineering Journal*, *393*.

Ahribesh, A. A., Lazarević, S., Janković-Častvan, I., Jokić, B., Spasojević, V., Radetić, T., Janaćković, Đ., & Petrović, R. (2017). Influence of the synthesis parameters on the properties of the sepiolite-based magnetic adsorbents. *Powder Technology*, *305*, 260–269.

Alejandro, S., Valdés, H., Manéro, M. H., & Zaror, C. A. (2014). Oxidative regeneration of toluene-saturated natural zeolite by gaseous ozone: The influence of zeolite chemical surface characteristics. *Journal of Hazardous Materials*, *274*, 212–220.

Al-Gaashani, R., Najjar, A., Zakaria, Y., Mansour, S., & Atieh, M. A. (2019). XPS and structural studies of high quality graphene oxide and reduced graphene oxide prepared by different chemical oxidation methods. *Ceramics International*, *45*(11), 14439–14448.

Al-Musawi, T. J., Mahvi, A. H., Khatibi, A. D., & Balarak, D. (2021a). Effective adsorption of ciprofloxacin antibiotic using powdered activated carbon magnetized by iron(III) oxide magnetic nanoparticles. *Journal of Porous Materials*, *28*(3), 835–852.

Alver, B. E., Sakizci, M., & Yörükoğullari, E. (2010). Investigation of clinoptilolite rich natural zeolites from Turkey: A combined XRF, TG/DTG, DTA and DSC study. *Journal of Thermal Analysis and Calorimetry*, *100*(1), 19–26.

Antimicrobial resistance, WHO (2020): https://www.who.int/news-room/fact-sheets/detail/antimicrobial-resistance (Accessed on October 23, 2022)

Armbruster, T. (2001). Clinoptilolite-heulandite: applications and basic research. In *Zeolites and Mesoporous Materials at the Dawn of the 21st Century* (Vol. 135, pp. 13–27). Elsevier.

Ashiq, A., Sarkar, B., Adassooriya, N., Walpita, J., Rajapaksha, A. U., Ok, Y. S., & Vithanage, M. (2019). Sorption process of municipal solid waste biochar-montmorillonite composite for ciprofloxacin removal in aqueous media. *Chemosphere*, *236*.

Awwad, N. S., Eed, E. M., el Askary, A., Ibrahium, H. A., Moustapha, M. E., & Ahmed, M. K. (2022). Development of nanocomposite based on hydroxyapatite/hematite/graphene oxide for medical applications. *Journal of Materials Research and Technology*, *18*, 4340–4352.

Baig, N., Ihsanullah, Sajid, M., & Saleh, T. A. (2019). Graphene-based adsorbents for the removal of toxic organic pollutants: A review. *Journal of Environmental Management*, *244*, 370–382.

Baugh, O. F., Barrett, E. P., Joyner, L. G., & Halenda, P. P. (1951). The volume and area distributions in porous substances.

Berlanga, M., Montero, M. T., Hernández-Borrell, J., & Viñas, M. (2004). Influence of the cell wall on ciprofloxacin susceptibility in selected wild-type Gram-negative and Gram-positive bacteria. *International Journal of Antimicrobial Agents*, *23*(6), 627–630.

Bijekar, S., Padariya, H. D., Yadav, V. K., Gacem, A., Hasan, M. A., Awwad, N. S., Yadav, K. K., Islam, S., Park, S., & Jeon, B. H. (2022). The State of the Art and Emerging Trends in the Wastewater Treatment in Developing Nations. *Water*, *14*(16).

Brandenburg, R. (2018). Corrigendum: Dielectric barrier discharges: progress on plasma sources and on the understanding of regimes and single filaments. *Plasma Sources Science and Technology*, *27*(7).

Brunauer, S., Emmett, P. H., & Teller, E. (2002). Adsorption of Gases in Multimolecular Layers. *Journal of the American Chemical Society*, *60*(2), 309–319.

Cakicioglu-Ozkan, F., & Ulku, S. (2005). The effect of HCl treatment on water vapor adsorption characteristics of clinoptilolite rich natural zeolite. *Microporous and Mesoporous Materials*, *77*(1), 47–53.

Carabineiro, S. A. C., Thavorn-Amornsri, T., Pereira, M. F. R., Serp, P., & Figueiredo, J. L. (2012). Comparison between activated carbon, carbon xerogel and carbon nanotubes for the adsorption of the antibiotic ciprofloxacin. *Catalysis Today*, *186*(1), 29–34.

Castro, C. J., Shyu, H. Y., Xaba, L., Bair, R., & Yeh, D. H. (2021). Performance and onsite regeneration of natural zeolite for ammonium removal in a field-scale non-sewered sanitation system. *Science of the Total Environment*, *776*.

Cerjan-Stefanović, Š., Ćurković, L., & Filipan, T. (1996). Metal ion exchange by natural zeolites. *Croatica Chemica Acta*, *69*(1), 281–290.

Chalkley, L. J., & Koornhof, H. J. (1985). Antimicrobial activity of ciprofloxacin against *Pseudomonas aeruginosa*, *Escherichia coli*, and *Staphylococcus aureus* determined by the killing curve method: antibiotic comparisons and synergistic interactions. *Antimicrobial Agents and Chemotherapy*, *28*(2).

Chávez-Mejía, A. C., Navarro-González, I., Magaña-López, R., Uscanga-Roldán, D., Zaragoza-Sánchez, P. I., & Jiménez-Cisneros, B. E. (2019). Presence and natural treatment of organic micropollutants and their risks after 100 years of incidental water reuse in agricultural irrigation. *Water*, *11*(10).

Chen, H., Gao, B., & Li, H. (2015). Removal of sulfamethoxazole and ciprofloxacin from aqueous solutions by graphene oxide. *Journal of Hazardous Materials*, *282*, 201–207.

Cheng, R., Li, H., Liu, Z., & Du, C. (2018). Halloysite nanotubes as an effective and recyclable adsorbent for removal of low-concentration antibiotics ciprofloxacin. *Minerals*, *8*(9).

Chinemerem Nwobodo, D., Ugwu, M. C., Oliseloke Anie, C., Al-Ouqaili, M. T. S., Chinedu Ikem, J., Victor Chigozie, U., & Saki, M. (2022). Antibiotic resistance: The challenges and some emerging strategies for tackling a global menace. *Journal of Clinical Laboratory Analysis*, *36*(9).

Cinar, S., & Beler-Baykal, B. (2005). Ion exchange with natural zeolites: an alternative for water softening? *Water Science & Technology*, *51*(11), 71–77.

Coelho, A. (2007). TOPAS Academic 4.1 Coelho Software, Brisbane, Australia.

Cotton, A. (2008). Dissolution kinetics of clinoptilolite and heulandite in alkaline conditions. *Bioscience Horizons*, *1*(1), 38–43.

Ćurković, L., Bolanča, T., Šiljeg, M., & Foglar, L. (2014). Kinetic modelling of Fe^{3+} ion uptake by zeolite from water monolithic and composite advanced ceramics for wear and corrosion protection. *Indian Journal of Chemical Technology*.

Daghooghi-Mobarakeh, H., Campbell, N., Bertrand, W. K., Kumar, P. G., Tiwari, S., Wang, L., Wang, R., Miner, M., & Phelan, P. E. (2020). Ultrasound-assisted regeneration of zeolite/water adsorption pair. *Ultrasonics Sonochemistry*, *64*.

Damjanović, L., Rakić, V., Rac, V., Stošić, D., & Auroux, A. (2010). The investigation of phenol removal from aqueous solutions by zeolites as solid adsorbents. *Journal of Hazardous Materials*, *184*(1–3), 477–484.

de Andrade, J. R., Oliveira, M. F., da Silva, M. G. C., & Vieira, M. G. A. (2018). Adsorption of Pharmaceuticals from Water and Wastewater Using Nonconventional Low-Cost Materials: A Review. *Industrial and Engineering Chemistry Research*, *57*(9), 3103–3127.

de Ilurdoz, M. S., Sadhwani, J. J., & Reboso, J. V. (2022). Antibiotic removal processes from water & wastewater for the protection of the aquatic environment - a review. *Journal of Water Process Engineering*, *45*.

de Velasco Maldonado, P. S., Hernández-Montoya, V., Concheso, A., & Montes-Morán, M. A. (2016). Formation of cerussite and hydrocerussite during adsorption of lead from aqueous solution on oxidized carbons by cold oxygen plasma. *Applied Surface Science*, *386*, 381–388.

de Velasco-Maldonado, P. S., Hernández-Montoya, V., Montes-Morán, M. A., Vázquez, N. A. R., & Pérez-Cruz, M. A. (2018). Surface modification of a natural zeolite by treatment with cold oxygen plasma: Characterization and application in water treatment. *Applied Surface Science*, *434*, 1193–1199.

Deere, J. R., Moore, S., Ferrey, M., Jankowski, M. D., Primus, A., Convertino, M., Servadio, J. L., Phelps, N. B. D., Hamilton, M. C., Chenaux-Ibrahim, Y., Travis, D. A., & Wolf, T. M. (2020). Occurrence of contaminants of emerging concern in aquatic ecosystems utilized by Minnesota tribal communities. *Science of the Total Environment*, *724*.

Dosa, M., Grifasi, N., Galletti, C., Fino, D., & Piumetti, M. (2022). Natural Zeolite Clinoptilolite Application in Wastewater Treatment: Methylene Blue, Zinc and Cadmium Abatement Tests and Kinetic Studies. *Materials*, *15*(22).

Duan, S., Liu, X., Wang, Y., Meng, Y., Alsaedi, A., Hayat, T., & Li, J. (2017). Plasma surface modification of materials and their entrapment of water contaminant: A review. *Plasma Processes and Polymers*, *14*(9).

Dutta, T., Kim, T., Vellingiri, K., Tsang, D. C. W., Shon, J. R., Kim, K. H., & Kumar, S. (2019). Recycling and regeneration of carbonaceous and porous materials through thermal or solvent treatment. *Chemical Engineering Journal*, *364*, 514–529.

El-Shafey, E. S. I., Al-Lawati, H., & Al-Sumri, A. S. (2012). Ciprofloxacin adsorption from aqueous solution onto chemically prepared carbon from date palm leaflets. *Journal of Environmental Sciences*, *24*(9), 1579–1586.

Enyoh, C. E., Verla, A. W., Qingyue, W., Ohiagu, F. O., Chowdhury, A. H., Enyoh, E. C., Chowdhury, T., Verla, E. N., & Chinwendu, U. P. (2020). An overview of emerging pollutants in air: Method of analysis and potential public health concern from human environmental exposure. *Trends in Environmental Analytical Chemistry*, *28*.

EU Directive 2015/495 (2015).

EU Directive 2020/1161 (2020).

Fahmy, A., Elzaref, A., Youssef, H., Shehata, H., Wassel, M., Friedrich, J., Poncin-Epaillard, F., & Debarnot, D. (2019). Plasma O 2 modifies the structure of synthetic zeolite-A to improve the removal of cadmium ions from aqueous solutions. *Turkish Journal of Chemistry*, *43*(1), 172–184.

Fan, H., Ma, Y., Wan, J., Wang, Y., Li, Z., & Chen, Y. (2020). Adsorption properties and mechanisms of novel biomaterials from banyan aerial roots via simple modification for ciprofloxacin removal. *Science of the Total Environment*, *708*.

Favvas, E. P., Tsanaktsidis, C. G., Sapalidis, A. A., Tzilantonis, G. T., Papageorgiou, S. K., & Mitropoulos, A. C. (2016). Clinoptilolite, a natural zeolite material: Structural characterization and performance evaluation on its dehydration properties of hydrocarbon-based fuels. *Microporous and Mesoporous Materials*, *225*, 385–391.

Frade, V. M. F., Dias, M., Teixeira, A. C. S. C., & Palma, M. S. A. (2014). Environmental contamination by fluoroquinolones. *Brazilian Journal of Pharmaceutical Sciences*, *50*(1), 41–54.

Freundlich, H. M. F. (1906). Over the adsorption in solution. *Journal of Physical Chemistry*, *57*, 385–470.

Gahrouei, Z. E., Imani, M., Soltani, M., & Shafyei, A. (2020). Synthesis of iron oxide nanoparticles for hyperthermia application: Effect of ultrasonic irradiation assisted co-precipitation route. *Advances in Natural Sciences: Nanoscience and Nanotechnology*, *11*(2).

Garcia-Basabe, Y., Rodriguez-Iznaga, I., de Menorval, L. C., Llewellyn, P., Maurin, G., Lewis, D. W., Binions, R., Autie, M., & Ruiz-Salvador, A. R. (2010). Step-wise dealumination of natural clinoptilolite: Structural and physicochemical characterization. *Microporous and Mesoporous Materials*, *135*(1–3), 187–196.

Gebhardt, P., Pattinson, S. W., Ren, Z., Cooke, D. J., Elliott, J. A., & Eder, D. (2014). Crystal engineering of zeolites with graphene. *Nanoscale*, *6*(13), 7319–7324.

Genç, N., & Dogan, E. C. (2015). Adsorption kinetics of the antibiotic ciprofloxacin on bentonite, activated carbon, zeolite, and pumice. *Desalination and Water Treatment*, *53*(3), 785–793.

Gerrity, D., Gamage, S., Holady, J. C., Mawhinney, D. B., Quiñones, O., Trenholm, R. A., & Snyder, S. A. (2011). Pilot-scale evaluation of ozone and biological activated carbon for trace organic contaminant mitigation and disinfection. *Water Research*, *45*(5), 2155–2165.

Golovko, O., Rehrl, A. L., Köhler, S., & Ahrens, L. (2020). Organic micropollutants in water and sediment from Lake Mälaren, Sweden. *Chemosphere*, *258*.

Grifoni, E., Piccini, G. M., Lercher, J. A., Glezakou, V. A., Rousseau, R., & Parrinello, M. (2021). Confinement effects and acid strength in zeolites. *Nature Communications*, *12*(1).

Gulicovski, J. J., Čerović, L. S., & Milonjić, S. K. (2008). Point of zero charge and isoelectric point of alumina. *Materials and Manufacturing Processes*, *23*(6), 615–619.

Han, R., Wang, Y., Sun, Q., Wang, L., Song, J., He, X., & Dou, C. (2010). Malachite green adsorption onto natural zeolite and reuse by microwave irradiation. *Journal of Hazardous Materials*, *175*(1–3), 1056–1061.

Hawash, H. B. I., Chmielewska, E., Netriová, Z., Majzlan, J., Pálková, H., Hudec, P., & Sokolík, R. (2018). Innovative comparable study for application of iron oxyhydroxide and manganese dioxide modified clinoptilolite in removal of Zn(II) from aqueous medium. *Journal of Environmental Chemical Engineering*, *6*(5), 6489–6503.

Hazra, M., & Durso, L. M. (2022). Performance Efficiency of Conventional Treatment Plants and Constructed Wetlands towards Reduction of Antibiotic Resistance. *Antibiotics*, *11*(1).

Hidayat, R., Wahyuningsih, S., & Ramelan, A. H. (2020). Simple synthesis of rGO (reduced graphene oxide) by thermal reduction of GO (graphene oxide). *IOP Conference Series: Materials Science and Engineering*, *858*(1).

Hovhannisyan, V., Siposova, K., Musatov, A., & Chen, S. J. (2021). Development of multifunctional nanocomposites for controlled drug delivery and hyperthermia. *Scientific Reports*, *11*(1).

Hrenovic, J., Milenkovic, J., Daneu, N., Kepcija, R. M., & Rajic, N. (2012). Antimicrobial activity of metal oxide nanoparticles supported onto natural clinoptilolite. *Chemosphere*, *88*(9), 1103–1107.

Huang, A., Yan, M., Lin, J., Xu, L., Gong, H., & Gong, H. (2021). A review of processes for removing antibiotics from breeding wastewater. *International Journal of Environmental Research and Public Health*, *18*(9).

Igwegbe, C. A., Oba, S. N., Aniagor, C. O., Adeniyi, A. G., & Ighalo, J. O. (2021). Adsorption of ciprofloxacin from water: A comprehensive review. *Journal of Industrial and Engineering Chemistry*, *93*, 57–77.

International Zeolite Association (2022): http://www.iza-online.org/ (Accessed on 7th December 2022)

Iskandar, F., Fitriani, P., Merissa, S., Mukti, R. R., Khairurrijal, & Abdullah, M. (2014). Fe3O4/Zeolite nanocomposites synthesized by microwave assisted coprecipitation and its performance in reducing viscosity of heavy oil. *AIP Conference Proceedings*, *1586*, 132–135.

Javanbakht, V., Ghoreishi, S. M., Habibi, N., & Javanbakht, M. (2016). A novel magnetic chitosan/clinoptilolite/magnetite nanocomposite for highly efficient removal of Pb(II) ions from aqueous solution. *Powder Technology*, *302*, 372–383.

Jevtić, S., Arčon, I., Rečnik, A., Babić, B., Mazaj, M., Pavlović, J., Matijaševic, D., Nikšić, M., & Rajić, N. (2014). The iron(III)-modified natural zeolitic tuff as an adsorbent and carrier for selenium oxyanions. *Microporous and Mesoporous Materials*, *197*, 92–100.

Jia, A., Wan, Y., Xiao, Y., & Hu, J. (2012). Occurrence and fate of quinolone and fluoroquinolone antibiotics in a municipal sewage treatment plant. *Water Research*, *46*(2).

Johnson, A. C., Keller, V., Dumont, E., & Sumpter, J. P. (2015). Assessing the concentrations and risks of toxicity from the antibiotics ciprofloxacin, sulfamethoxazole, trimethoprim and erythromycin in European rivers. *Science of the Total Environment*, *511*, 747–755.

Johra, F. T., Lee, J. W., & Jung, W. G. (2014). Facile and safe graphene preparation on solution based platform. *Journal of Industrial and Engineering Chemistry*, *20*(5), 2883–2887.

Jones, O. A. H., Voulvoulis, N., & Lester, J. N. (2002). Aquatic environmental assessment of the top 25 English prescription pharmaceuticals. *Water Research*, *36*.

Joos, A., Rümenapp, C., Wagner, F. E., & Gleich, B. (2016). Characterisation of iron oxide nanoparticles by Mössbauer spectroscopy at ambient temperature. *Journal of Magnetism and Magnetic Materials*, *399*, 123–129.

Kalló, D. (2001). Applications of natural zeolites in water and wastewater treatment. *Reviews in Mineralogy and Geochemistry*, *45*, 518–550.

Kaplanec, I., Rečnik, A., Mali, G., & Rajić, N. (2017). Study of the iron(III)-modified clinoptilolite in the adsorption of phosphate from aqueous medium: Mechanism and kinetics. *Desalination and Water Treatment*, *78*, 231–240.

Kasonga, T. K., Coetzee, M. A. A., Kamika, I., Ngole-Jeme, V. M., & Benteke Momba, M. N. (2021). Endocrine-disruptive chemicals as contaminants of emerging concern in wastewater and surface water: A review. *Journal of Environmental Management*, *277*.

Katsou, E., Malamis, S., Tzanoudaki, M., Haralambous, K. J., & Loizidou, M. (2011). Regeneration of natural zeolite polluted by lead and zinc in wastewater treatment systems. *Journal of Hazardous Materials*, *189*(3), 773–786.

Khalil, M. I. (2015). Co-precipitation in aqueous solution synthesis of magnetite nanoparticles using iron(III) salts as precursors. *Arabian Journal of Chemistry*, *8*(2), 279–284.

Kim, D. W., Han, H., Kim, H., Guo, X., & Tsapatsis, M. (2018). Preparation of a graphene oxide/faujasite composite adsorbent. *Microporous and Mesoporous Materials*, *268*, 243–250.

Kim, W., Suh, C. Y., Cho, S. W., Roh, K. M., Kwon, H., Song, K., & Shon, I. J. (2012). A new method for the identification and quantification of magnetite-maghemite mixture using conventional X-ray diffraction technique. *Talanta*, *94*, 348–352.

Klein, E. Y., van Boeckel, T. P., Martinez, E. M., Pant, S., Gandra, S., Levin, S. A., Goossens, H., & Laxminarayan, R. (2018). Global increase and geographic convergence in antibiotic consumption between 2000 and 2015. *Proceedings of the National Academy of Sciences of the United States of America*, *115*(15), E3463–E3470.

Kogelschatz, U. (2003). Dielectric-barrier Discharges: Their History, Discharge Physics, and Industrial Applications. In *Plasma Chemistry and Plasma Processing* (Vol. 23, Issue 1).

Kouli, M. E., Banis, G., Tsarabaris, P., Ferraro, A., & Hristoforou, E. (2018). A study on magnetic removal of sodium, calcium and potassium ions from seawater using magnetite/clinoptilolite–Na composite nanoparticles. *Journal of Magnetism and Magnetic Materials*, *465*, 692–699.

Kovalova, L., Siegrist, H., Von Gunten, U., Eugster, J., Hagenbuch, M., Wittmer, A., Moser, R., & McArdell, C. S. (2013). Elimination of micropollutants during post-treatment of hospital wastewater with powdered activated carbon, ozone, and UV. *Environmental Science and Technology*, *47*(14), 7899–7908.

Kozakova, Z., Kuritka, I., Kazantseva, N. E., Babayan, V., Pastorek, M., Machovsky, M., Bazant, P., & Saha, P. (2015). The formation mechanism of iron oxide nanoparticles within the microwave-assisted solvothermal synthesis and its correlation with the structural and magnetic properties. *Dalton Transactions*, *44*(48), 21099–21108.

Kraemer, S. A., Ramachandran, A., & Perron, G. G. (2019). Antibiotic pollution in the environment: From microbial ecology to public policy. *Microorganisms*, *7*(6).

Kragović, M., Daković, A., Marković, M., Krstić, J., Gatta, G. D., & Rotiroti, N. (2013). Characterization of lead sorption by the natural and Fe(III)-modified zeolite. *Applied Surface Science*, *283*, 764–774.

Krishnamoorthy, K., Veerapandian, M., Yun, K., & Kim, S. J. (2013). The chemical and structural analysis of graphene oxide with different degrees of oxidation. *Carbon*, *53*, 38–49.

Kümmerer, K. (2011). Emerging Contaminants versus Micro-pollutants. *Clean - Soil, Air, Water*, *39*(10), 889–890.

Lagergren, S. (1898). About the theory of so-called adsorption of soluble substances. *K. Sven. Vetenskapsakad. Handl.*, *24*, 1–39.

Langmuir, I. (1918). The adsorption of gases on plane surface of glass, mica, and platinum. *Journal of American Chemical Society*, *40*, 1361–1403.

Le, G. T. T., Chanlek, N., Manyam, J., Opaprakasit, P., Grisdanurak, N., & Sreearunothai, P. (2019). Insight into the ultrasonication of graphene oxide with strong changes in its

properties and performance for adsorption applications. *Chemical Engineering Journal*, *373*, 1212–1222.

Lee, J., Lee, C. W., Yong, H. I., Lee, H. J., Jo, C., & Jung, S. (2017). Use of atmospheric pressure cold plasma for meat industry. *Korean Journal for Food Science of Animal Resources*, *37*(4), 477–485.

Lei, X., Li, M., Zhang, Z., Feng, C., Bai, W., & Sugiura, N. (2009). Electrochemical regeneration of zeolites and the removal of ammonia. *Journal of Hazardous Materials*, *169*(1–3), 746–750.

Lin, C. C., & Lee, C. Y. (2020). Adsorption of ciprofloxacin in water using Fe3O4 nanoparticles formed at low temperature and high reactant concentrations in a rotating packed bed with co-precipitation. *Materials Chemistry and Physics*, *240*.

Lin, H., Liu, Q. L., Dong, Y. B., He, Y. H., & Wang, L. (2015). Physicochemical properties and mechanism study of clinoptilolite modified by NaOH. *Microporous and Mesoporous Materials*, *218*, 174–179.

Lin, J., Chen, J., Cai, X., Qiao, X., Huang, L., Wang, D., & Wang, Z. (2007). Evolution of toxicity upon hydrolysis of fenoxaprop-p-ethyl. *Journal of Agricultural and Food Chemistry*, *55*(18), 7626–7629.

Liu, L., Liu, C., Zheng, J., Huang, X., Wang, Z., Liu, Y., & Zhu, G. (2013). Elimination of veterinary antibiotics and antibiotic resistance genes from swine wastewater in the vertical flow constructed wetlands. *Chemosphere*, *91*(8), 1088–1093.

Lofthus, A., & Krupenie, P. H. (1977). *The Spectrum of Molecular Nitrogen*.

Lofù, A., Mastrorilli, P., Dell'Anna, M. M., Mali, M., Sisto, R., & Vignola, R. (2016). Iron(II) modified natural zeolites for hexavalent chromium removal from contaminated water. *Archives of Environmental Protection*, *42*(1), 35–40.

Lowell, S., Shields, J., Thomas, M. A., & Thommes, M. (2006). Characterization of Porous Solids and Powders: Surface Area, Pore Size and Density. *42*(09), 42-5288-42–5288.

Lu, X. F., Chen, X. Y., Zhou, W., Tong, Y. X., & Li, G. R. (2015). α-Fe_2O_3@PANI core-shell nanowire arrays as negative electrodes for asymmetric supercapacitors. *ACS Applied Materials and Interfaces*, *7*(27), 14843–14850.

Luo, Y., Guo, W., Ngo, H. H., Nghiem, L. D., Hai, F. I., Zhang, J., Liang, S., & Wang, X. C. (2014). A review on the occurrence of micropollutants in the aquatic environment and their fate and removal during wastewater treatment. *Science of the Total Environment*, *473–474*, 619–641.

Ma, S., Si, Y., Wang, F., Su, L., Xia, C. C., Yao, J., Chen, H., & Liu, X. (2017). Interaction processes of ciprofloxacin with graphene oxide and reduced graphene oxide in the presence of montmorillonite in simulated gastrointestinal fluids. *Scientific Reports*, *7*(1).

Maddela, N. R., Ramakrishnan, B., Kakarla, D., Venkateswarlu, K., & Megharaj, M. (2022). Major contaminants of emerging concern in soils: a perspective on potential health risks. *RSC Advances*, *12*(20), 12396–12415.

Magureanu, M., Bilea, F., Bradu, C., & Hong, D. (2021). A review on non-thermal plasma treatment of water contaminated with antibiotics. *Journal of Hazardous Materials, 417*.

Manjili, M., Silva, M. R., Garman, D., & Zhang, H. F. (2020). Graphene oxide and thiol functionalized natural zeolite for the removal of lead from water. *Water Science and Technology: Water Supply*, *20*(7), 2577–2588.

Marciuš, M., Ristić, M., Grenèche, J. M., Musić, S., Krehula, S., Kuzmann, E., & Homonnay, Z. (2021). One-pot synthesis and properties of Mn-doped maghemite nanoparticles using acetylacetonate precursors. *Journal of Radioanalytical and Nuclear Chemistry*, *328*(3), 1181–1187.

Meador, J. P., Yeh, A., & Gallagher, E. P. (2018). Adverse metabolic effects in fish exposed to contaminants of emerging concern in the field and laboratory. *Environmental Pollution, 236*, 850–861.

Miądlicki, P., Wróblewska, A., Kiełbasa, K., Koren, Z. C., & Michalkiewicz, B. (2021). Sulfuric acid modified clinoptilolite as a solid green catalyst for solvent-free *α*-pinene isomerization process. *Microporous and Mesoporous Materials*, *324*.

Mirzaei, H., Almasian, M. R., Mousavian, S. M. A., & Sid Kalal, H. (2019). Plasma modification of a natural zeolite to improve its adsorption capacity of strontium ions from water samples. *International Journal of Environmental Science and Technology*, *16*(10), 6157–6166.

Mohsen, E., El-Borady, O. M., Mohamed, M. B., & Fahim, I. S. (2020). Synthesis and characterization of ciprofloxacin loaded silver nanoparticles and investigation of their antibacterial effect. *Journal of Radiation Research and Applied Sciences*, *13*(1), 416–425.

Mohseni-Bandpi, A., Al-Musawi, T. J., Ghahramani, E., Zarrabi, M., Mohebi, S., & Vahed, S. A. (2016). Improvement of zeolite adsorption capacity for cephalexin by coating with magnetic Fe_3O_4 nanoparticles. *Journal of Molecular Liquids*, *218*, 615–624.

Mojiri, A., Zhou, J. L., Robinson, B., Ohashi, A., Ozaki, N., Kindaichi, T., Farraji, H., & Vakili, M. (2020). Pesticides in aquatic environments and their removal by adsorption methods. *Chemosphere*, *253*.

Morais, A., Alves, J. P. C., Lima, F. A. S., Lira-Cantu, M., & Nogueira, A. F. (2015). Enhanced photovoltaic performance of inverted hybrid bulk-heterojunction solar cells using TiO_2 /reduced graphene oxide films as electron transport layers. *Journal of Photonics for Energy*, *5*(1), 057408.

Motsi, T., Rowson, N. A., & Simmons, M. J. H. (2009). Adsorption of heavy metals from acid mine drainage by natural zeolite. *International Journal of Mineral Processing*, *92*(1–2), 42–48.

Moulder, J. F., Stickle, W. F., Sobol, P. E., Bomben, K. D., & Chastain, J. (1992). Handbook of X-ray Photoelectron Spectroscopy: A Reference Book of Standard Spectra for Identification and Interpretation of XPS Data.

Muhamad, K. S. S. K., Mohamed, F., Radiman, S., Hamzah, A., Sarmani, S., Siong, K. K., Yasir, M. S., Rahman, I. A., & Rosli, N. R. A. M. (2016). Synthesis and characterization of exfoliated graphene oxide. *AIP Conference Proceedings*, *1784*.

Muir, B., Wołowiec, M., Bajda, T., Nowak, P., & Czupryński, P. (2016). The Removal of Organic Compounds by Natural and Synthetic Surface-Functionalized Zeolites: A Mini-Review. *Mineralogia*, *48*(1–4), 145–156.

Najafpoor, A. A., Nemati Sani, O., Alidadi, H., Yazdani, M., Navaei Fezabady, A. A., & Taghavi, M. (2019). Optimization of ciprofloxacin adsorption from synthetic wastewaters using γ-Al_2O_3 nanoparticles: An experimental design based on response surface methodology. *Colloids and Interface Science Communications*, *33*.

Nan, L., Yingying, L., Jixiang, L., Dujuan, O., & Wenjuan, W. (2019). Study on the removal of high contents of ammonium from piggery wastewater by clinoptilolite and the corresponding mechanisms. *Open Chemistry*, *17*(1), 1393–1402.

Naveed, S., & Waheed, N. (2014). Simple UV spectrophotometric assay of ciprofloxacin. *3*.

Neustroev, E. P. (2018). Plasma Treatment of Graphene Oxide. *Graphene Oxide - Applications and Opportunities*.

Nezamzadeh-Ejhieh, A., & Tavakoli-Ghinani, S. (2014). Effect of a nano-sized natural clinoptilolite modified by the hexadecyltrimethyl ammonium surfactant on cephalexin drug delivery. *Comptes Rendus Chimie*, *17*(1), 49–61.

Ngeno, E. C., Shikuku, V. O., Orata, F., Baraza, L. D., & Kimosop, S. J. (2019). Caffeine and ciprofloxacin adsorption from water onto clinoptilolite: Linear isotherms, kinetics, thermodynamic and mechanistic studies. *South African Journal of Chemistry*, *72*, 136–142.

Nuić, I., Gosar, M., Ugrina, M., & Trgo, M. (2022). Assessment of Natural Zeolite Clinoptilolite for Remediation of Mercury-Contaminated Environment. *Processes*, *10*(4).

Patel, M., Kumar, R., Kishor, K., Mlsna, T., Pittman, C. U., & Mohan, D. (2019). Pharmaceuticals of emerging concern in aquatic systems: Chemistry, occurrence, effects, and removal methods. *Chemical Reviews*, *119*(6), 3510–3673.

Pati, S. S., Kalyani, S., Mahendran, V., & Philip, J. (2014). Microwave assisted synthesis of magnetite nanoparticles. *Journal of Nanoscience and Nanotechnology*, *14*(8), 5790–5797.

Pavlinović, A., Novaković, M., & Nuić, I. (2021). Removal of carbendazim from aqueous solutions by adsorption on different types of zeolite. *St Open*, *2*, 1–11.

Pavlovic, J., Popova, M., Mihalyi, R. M., Mazaj, M., Mali, G., Kovač, J., Lazarova, H., & Rajic, N. (2019). Catalytic activity of SnO_2- and SO_4/SnO_2-containing clinoptilolite in the esterification of levulinic acid. *Microporous and Mesoporous Materials*, *279*, 10–18.

Pendyala, S. K., Thyagarajan, K., Gurusampath Kumar, A., & Obulapathi, L. (2019). Investigations on physical properties of Mg ferrite nanoparticles for microwave applications. *Journal of Microwave Power and Electromagnetic Energy*, *53*(1), 3–11.

Petrie, B., Barden, R., & Kasprzyk-Hordern, B. (2015). A review on emerging contaminants in wastewaters and the environment: Current knowledge, understudied areas and recommendations for future monitoring. *Water Research*, *72*, 3–27.

Polat, E., Karaca, M., & Demir, H. (2004). Use of Natural Zeolite (Clinoptilolite) in Agriculture. *Journal of Fruit and Ornamental Plant Research*, *12*.

Qiu, M., Qian, C., Xu, J., Wu, J., & Wang, G. (2008). Studies on the adsorption of dyes into clinoptilolite. *Desalination*, *243*, 286–292.

Rajic, N., Stojakovic, D., Daneu, N., & Recnik, A. (2011). The formation of oxide nanoparticles on the surface of natural clinoptilolite. *Journal of Physics and Chemistry of Solids*, *72*(6), 800–803.

Rajic, N., Stojakovic, D., Jovanovic, M., Logar, N. Z., Mazaj, M., & Kaucic, V. (2010). Removal of nickel(II) ions from aqueous solutions using the natural clinoptilolite and preparation of nano-NiO on the exhausted clinoptilolite. *Applied Surface Science*, *257*(5), 1524–1532.

Rajput, S., Pittman, C. U., & Mohan, D. (2016). Magnetic magnetite (Fe_3O_4) nanoparticle synthesis and applications for lead (Pb^{2+}) and chromium (Cr^{6+}) removal from water. *Journal of Colloid and Interface Science*, *468*, 334–346.

Rakshit, S., Sarkar, D., Elzinga, E. J., Punamiya, P., & Datta, R. (2013). Mechanisms of ciprofloxacin removal by nano-sized magnetite. *Journal of Hazardous Materials*, *246–247*, 221–226.

Rečnik, A., Nyir-Kósa, I., Dódony, I., & Pósfai, M. (2013). Growth defects and epitaxy in Fe_3O_4 and γ-Fe_2O_3 nanocrystals. *CrystEngComm*, *15*(37), 7539–7547.

Rodeghero, E., Martucci, A., Cruciani, G., Sarti, E., Cavazzini, A., Costa, V., Bagatin, R., & Pasti, L. (2017). Detailed Investigation of Thermal Regeneration of High-Silica ZSM-5 Zeolite through in Situ Synchrotron X-ray Powder Diffraction and Adsorption Studies. *Journal of Physical Chemistry C*, *121*(33), 17958–17968.

Rosenfeldt, E. J., Linden, K. G., Canonica, S., & von Gunten, U. (2006). Comparison of the efficiency of •OH radical formation during ozonation and the advanced oxidation processes O_3/H_2O_2 and UV/H_2O_2. *Water Research*, *40*(20), 3695–3704.

Rožić, M., Cerjan-Stefanović, Š., & Ćurković, L. (2002). Evaluation of Croatian Clinoptilolite- and Montmorillonite-rich Tuffs for Ammonium Removal. *Croatia Chemica Acta*, *75*(1), 255–269.

Rzodkiewicz, L. D., Annis, M. L., & Woolnough, D. A. (2022). Contaminants of emerging concern may pose prezygotic barriers to freshwater mussel recruitment. *Journal of Great Lakes Research*, *48*(3), 768–781.

Sabbagh, N., Tahvildari, K., & Mehrdad Sharif, A. A. (2021). Application of chitosan-alginate bio composite for adsorption of malathion from wastewater: Characterization and response surface methodology. *Journal of Contaminant Hydrology*, *242*.

Saber Braim, F., Noor Ashikin Nik Ab Razak, N., Abdul Aziz, A., Qasim Ismael, L., & Kayode Sodipo, B. (2022). Ultrasound assisted chitosan coated iron oxide nanoparticles: Influence

of ultrasonic irradiation on the crystallinity, stability, toxicity and magnetization of the functionalized nanoparticles. *Ultrasonics Sonochemistry*, *88*.

Sadeek, S. A., El-Shwiniy, W. H., Zordok, W. A., & El-Didamony, A. M. (2011). Spectroscopic, structure and antimicrobial activity of new Y(III) and Zr(IV) ciprofloxacin. *Spectrochimica Acta - Part A: Molecular and Biomolecular Spectroscopy*, *78*(2), 854–867.

Sahoo, T. R., & Prelot, B. (2020). Adsorption processes for the removal of contaminants from wastewater: The perspective role of nanomaterials and nanotechnology. In *Nanomaterials for the Detection and Removal of Wastewater Pollutants* (pp. 161–222).

Sakiyama, Y., Graves, D. B., Chang, H. W., Shimizu, T., & Morfill, G. E. (2012). Plasma chemistry model of surface microdischarge in humid air and dynamics of reactive neutral species. *Journal of Physics D: Applied Physics*, *45*(42).

Salem Attia, T. M., Hu, X. L., & Yin, D. Q. (2013). Synthesized magnetic nanoparticles coated zeolite for the adsorption of pharmaceutical compounds from aqueous solution using batch and column studies. *Chemosphere*, *93*(9), 2076–2085.

Salem Attia, T. M., Hu, X. L., & Yin, D. Q. (2014). Synthesised magnetic nanoparticles coated zeolite (MNCZ) for the removal of arsenic (As) from aqueous solution. *Journal of Experimental Nanoscience*, *9*(6), 551–560.

Salvador, F., Martin-Sanchez, N., Sanchez-Hernandez, R., Sanchez-Montero, M. J., & Izquierdo, C. (2015). Regeneration of carbonaceous adsorbents. Part I: Thermal Regeneration. In *Microporous and Mesoporous Materials* (Vol. 202, pp. 259–276). Elsevier.

Santos, L. H. M. L. M., Araújo, A. N., Fachini, A., Pena, A., Delerue-Matos, C., & Montenegro, M. C. B. S. M. (2010). Ecotoxicological aspects related to the presence of pharmaceuticals in the aquatic environment. *Journal of Hazardous Materials*, *175*(1–3), 45–95.

Sarangapani, C., O'toole, G., & Bourke, P. (2017). Atmospheric cold plasma dissipation efficiency of atmospheric cold plasma dissipation efficiency of agrochemicals on blueberries agrochemicals on blueberries. *School of Food Science and Environmental Health.*

Sarangapani, C., Ziuzina, D., Behan, P., Boehm, D., Gilmore, B. F., Cullen, P. J., & Bourke, P. (2019). Degradation kinetics of cold plasma-treated antibiotics and their antimicrobial activity. *Scientific Reports*, *9*(1).

Sarma, G. K., Sen Gupta, S., & Bhattacharyya, K. G. (2019). Nanomaterials as versatile adsorbents for heavy metal ions in water: a review. *Environmental Science and Pollution Research*, 26(7), 6245–6278.

Savić, A. B., Čokeša, D., Lazarević, S., Jokić, B., Janaćković, D., Petrović, R., & Živković, L. S. (2016). Tailoring of magnetite powder properties for enhanced phosphate removal: Effect of PEG addition in the synthesis process. *Powder Technology*, *301*, 511–519.

Schollenberger, C. J., & Simon, R. H. (1945). Determination of exchange capacity and exchangeable basis in soil – ammonium acetate method. *Ohio Agriculture Experimental Station.*

Schwaminger, S. P., Bauer, D., Fraga-García, P., Wagner, F. E., & Berensmeier, S. (2017). Oxidation of magnetite nanoparticles: impact on surface and crystal properties. *CrystEngComm*, *19*(2), 246–255.

Semmens, M. J., & Goodrich, R. I. Jr. (1977). Biological regeneration of ammonium-saturated clinoptilolite.*Current Research, 1*(1).

Shafeeyan, M. S., Wan Daud, W. M. A., Houshmand, A., & Arami-Niya, A. (2012). The application of response surface methodology to optimize the amination of activated carbon for the preparation of carbon dioxide adsorbents. *Fuel*, *94*, 465–472.

Shahbazi Rad, Z., & Abbasi Davani, F. (2020). Measurements of the electrical parameters and wound area for investigation on the effect of different non-thermal atmospheric pressure plasma sources on wound healing time. *Measurement: Journal of the International Measurement Confederation*, *155*.

Shang, K., Wang, M., Peng, B., Li, J., Lu, N., Jiang, N., & Wu, Y. (2020). Characterization of a novel volume-surface DBD reactor: Discharge characteristics, ozone production and benzene degradation. *Journal of Physics D: Applied Physics*, *53*(6).

Shao, Y., Chen, Z., Hollert, H., Zhou, S., Deutschmann, B., & Seiler, T. B. (2019). Toxicity of 10 organic micropollutants and their mixture: Implications for aquatic risk assessment. *Science of the Total Environment*, *666*, 1273–1282.

Silva, B. S., Ribeiro, M. C. B., Ramos, B., & de Castro Peixoto, A. L. (2022). Removal of Amoxicillin from Processing Wastewater by Ozonation and UV-Aided Ozonation: Kinetic and Economic Comparative Study. *Water*, *14*(20).

Silva, M. R., Lecus, A., Gajdardziska-Josifovska, M., Schofield, M., Virnoche, M., Chang, J., Chen, J., & Garman, D. (2020). Graphene-oxide loading on natural zeolite particles for enhancement of adsorption properties. *RSC Advances*, *10*(8), 4589–4597.

Simões, M., Rocha, S., Coimbra, M. A., & Vieira, M. J. (2008). Enhancement of Escherichia coli and Staphylococcus aureus Antibiotic Susceptibility Using Sesquiterpenoids. *Medicinal Chemistry*, *4*.

Simona, M., & Camelia, T. (2019). Zeolites Applications in Veterinary Medicine. In *Zeolites – New Challenges.* IntechOpen.

Sing, K. S. W. (1982). Reporting physisorption data for gas/solid systems. *Pure and Applied Chemistry*, *54*(11), 2201–2218.

Sobuś, N., Czekaj, I., Diichuk, V., & Kobasa, I. M. (2020). Characteristics of the structure of natural zeolites and their potential application in catalysis and adsorption processes. *Technical Transactions*, 1–20.

Sohrabi, N., Mohammadi, R., Ghassemzadeh, H. R., & Heris, S. S. S. (2021). Equilibrium, kinetic and thermodynamic study of diazinon adsorption from water by clay/GO/Fe_3O_4:

Modeling and optimization based on response surface methodology and artificial neural network. *Journal of Molecular Liquids, 328.*

Stojakovic, D., Milenkovic, J., Daneu, N., & Rajic, N. (2012). A Study of the Removal of Copper Ions from Aqueous Solution Using Clinoptilolite from Serbia. *Clays and Clay Minerals*, *59*(3), 277–285.

Suarez, S., Lema, J. M., & Omil, F. (2009). Pre-treatment of hospital wastewater by coagulation-flocculation and flotation. *Bioresource Technology*, *100*(7), 2138–2146.

Tam, N. T. M., Liu, Y., Bashir, H., Yin, Z., He, Y., & Zhou, X. (2019). Efficient Removal of Diclofenac from Aqueous Solution by Potassium Ferrate-Activated Porous Graphitic Biochar: Ambient Condition Influences and Adsorption Mechanism. *International Journal of Environmental Research and Public Health*, *17*(1), 291.

Thy, L. T. M., Linh, N. T. C., Tram, N. T. T., Tu, T. H., Tai, L. T., Khang, P. T., Nam, H. M., Hieu, N. H., & Phong, M. T. (2021). Fabrication and Response Surface Methodology for the Adsorption of Nickel Ferrite-Graphene Oxide Nanocomposite for the Removal of Methylene Blue from Water. *Journal of Nanomaterials*.

Tian, J., Guan, J., Gao, H., Wen, Y., & Ren, Z. (2016). The adsorption and mass-transfer process of cationic red X-GRL dye on natural zeolite. *Water Science and Technology*, *73*(9), 2119–2131.

Trachta, M., Bulánek, R., Bludský, O., & Rubeš, M. (2022). Brønsted acidity in zeolites measured by deprotonation energy. *Scientific Reports*, *12*(1).

Tran, Q. T., Do, T. H., Ha, X. L., Nguyen, H. P., Nguyen, A. T., Ngo, T. C. Q., & Chau, H. D. (2022). Study of the Ciprofloxacin Adsorption of Activated Carbon Prepared from Mangosteen Peel. *Applied Sciences*, *12*(17).

Trivedi, P., & Vasudevan, D. (2007). Spectroscopic investigation of ciprofloxacin speciation at the goethite-water interface. *Environmental Science and Technology*, *41*(9), 3153–3158.

Tušek, D., Ašperger, D., Bačić, I., Ćurković, L., & Macan, J. (2017). Environmentally acceptable sorbents of chemical warfare agent simulants. *Journal of Materials Science*, *52*(5), 2591–2604.

Valdés, L., Pérez, I., de Ménorval, L. C., Altshuler, E., Fossum, J. O., & Rivera, A. (2017). A simple way for targeted delivery of an antibiotic: In vitro evaluation of a nanoclay-based composite. *PLoS ONE*, *12*(11).

Van Reeuwijk, L. P. (1974). *The Thermal Dehydration of Natural Zeolites*. Mededelingen Landbouwhogeschool, Wageningen, Nederland, *74*(9).

Veloso, C. H., Filippov, L. O., Filippova, I. V., Ouvrard, S., & Araujo, A. C. (2020). Adsorption of polymers onto iron oxides: Equilibrium isotherms. *Journal of Materials Research and Technology*, *9*(1), 779–788.

Verlicchi, P., Al Aukidy, M., & Zambello, E. (2012). Occurrence of pharmaceutical compounds in urban wastewater: Removal, mass load and environmental risk after a secondary treatment-A review. *Science of the Total Environment*, *429*, 123–155.

Wang, F., Yang, B., Wang, H., Song, Q., Tan, F., & Cao, Y. (2016). Removal of ciprofloxacin from aqueous solution by a magnetic chitosan grafted graphene oxide composite. *Journal of Molecular Liquids*, *222*, 188–194.

Wang, J. C., Ren, J., Yao, H. C., Zhang, L., Wang, J. S., Zang, S. Q., Han, L. F., & Li, Z. J. (2016). Synergistic photocatalysis of Cr(VI) reduction and 4-Chlorophenol degradation over hydroxylated α-Fe_2O_3 under visible light irradiation. *Journal of Hazardous Materials*, *311*, 11–19.

Wang, S., Li, H., Xie, S., Liu, S., & Xu, L. (2006). Physical and chemical regeneration of zeolitic adsorbents for dye removal in wastewater treatment. *Chemosphere*, *65*(1), 82–87.

Watkinson, A. J., Murby, E. J., & Costanzo, S. D. (2007). Removal of antibiotics in conventional and advanced wastewater treatment: Implications for environmental discharge and wastewater recycling. *Water Research*, *41*(18), 4164–4176.

Weber, W. J., Jr., & Morris, J. C. (1962). Advances in Water Pollution Research: Removal of Biologically Resistant Pollutants from Waste Waters by Adsorption. *Proceedings of the International Conference on Water Pollution Symposium*.

Whalley, C. (2018). Chemicals in European waters Knowledge developments.

Wilkinson, J., Hooda, P. S., Barker, J., Barton, S., & Swinden, J. (2017). Occurrence, fate and transformation of emerging contaminants in water: An overarching review of the field. *Environmental Pollution*, *231*, 954–970.

Wojciechowska, A., & Lendzion-Bielun, Z. (2020). Synthesis and characterization of magnetic nanomaterials with adsorptive properties of arsenic ions. *Molecules*, *25*(18). https://doi.org/10.3390/molecules25184117

Xiao, W., Jiang, X., Liu, X., Zhou, W., Garba, Z. N., Lawan, I., Wang, L., & Yuan, Z. (2021). Adsorption of organic dyes from wastewater by metal-doped porous carbon materials. In *Journal of Cleaner Production*, *284*.

Xu, W., Chen, Y., Zhang, W., & Li, B. (2019). Fabrication of graphene oxide/bentonite composites with excellent adsorption performances for toluidine blue removal from aqueous solution. *Advanced Powder Technology*, *30*(3), 493–501.

Xu, Y.-H., Nakajima, T., & Ohki, A. (2002). Adsorption and removal of arsenic(V) from drinking water by aluminum-loaded Shirasu-zeolite. *Journal of Hazardous Materials*, *92*.

Xue, P., Zhao, Y., Zhao, D., Chi, M., Yin, Y., Xuan, Y., & Wang, X. (2021). Mutagenicity, health risk, and disease burden of exposure to organic micropollutants in water from a drinking water treatment plant in the Yangtze River Delta, China. *Ecotoxicology and Environmental Safety*, *221*.

Yaneva, Z., Ivanova, D., & Popov, N. (2021). Clinoptilolite microparticles as carriers of catechin-rich acacia catechu extracts: Microencapsulation and in vitro release study. *Molecules*, *26*(6).

Yavuz, Ö., & Saka, C. (2013). Surface modification with cold plasma application on kaolin and its effects on the adsorption of methylene blue. *Applied Clay Science*, *85*(1), 96–102.

Yu, Y., Murthy, B. N., Shapter, J. G., Constantopoulos, K. T., Voelcker, N. H., & Ellis, A. V. (2013). Benzene carboxylic acid derivatized graphene oxide nanosheets on natural zeolites as effective adsorbents for cationic dye removal. *Journal of Hazardous Materials*, *260*, 330–338.

Zabochnicka-Świątek, M., & Malińska, K. (2010). Removal of ammonia by clinoptilolite. *Global NEST Journal*, *12*(3).

Zahoor, M., Ullah, A., Alam, S., Muhammad, M., Setyobudi, R. H., Zekker, I., & Sohail, A. (2022). Novel Magnetite Nanocomposites (Fe_3O_4/C) for Efficient Immobilization of Ciprofloxacin from Aqueous Solutions through Adsorption Pretreatment and Membrane Processes. *Water*, *14*(5).

Zendelska, A., Lisichkov, K., Kuvendziev, S., Golomeova, M., Jakupi, Š., Lisičkov, K., Kuvendžiev, S., & Marinkovski, M. (2018). Characterization and application of clinoptilolite for removal of heavy metal ions from water resources. *Geologica Macedonica*, *32*(1).

Zhang, B., Han, X., Gu, P., Fang, S., & Bai, J. (2017). Response surface methodology approach for optimization of ciprofloxacin adsorption using activated carbon derived from the residue of desilicated rice husk. *Journal of Molecular Liquids*, *238*, 316–325.

Zhang, J., Yan, M., Sun, G., & Liu, K. (2021). An environment-friendly Fe_3O_4@CFAS porous ceramic: Adsorption of Cu(II) ions and process optimisation using response surface methodology. *Ceramics International*, *47*(6), 8256–8264.

Zhang, W., Zhou, Z., An, Y., Du, S., Ruan, D., Zhao, C., Ren, N., & Tian, X. (2017). Optimization for zeolite regeneration and nitrogen removal performance of a hypochlorite-chloride regenerant. *Chemosphere*, *178*, 565–572.

Zhou, W., Ye, Z., Nikiforov, A., Chen, J., Wang, J., Zhao, L., & Zhang, X. (2021). The influence of relative humidity on double dielectric barrier discharge plasma for chlorobenzene removal. *Journal of Cleaner Production*, *288*.

Zhu, X., Tsang, D. C. W., Chen, F., Li, S., & Yang, X. (2015). Ciprofloxacin adsorption on graphene and granular activated carbon: Kinetics, isotherms, and effects of solution chemistry. *Environmental Technology*, *36*(24), 3094–3102.

Zide, D., Fatoki, O., Oputu, O., Opeolu, B., Nelana, S., & Olatunji, O. (2018). Zeolite 'adsorption' capacities in aqueous acidic media; The role of acid choice and quantification method on ciprofloxacin removal. *Microporous and Mesoporous Materials*, *255*, 226–241.

Zieliński, M., Zielińska, M., & Dębowski, M. (2016). Ammonium removal on zeolite modified by ultrasound. *Desalination and Water Treatment*, *57*(19), 8748–8753.

Author’s biography

Barbara Kalebić was born on December 14, 1994, in Zagreb, Croatia. In 2018, she completed her undergraduate and postgraduate studies in Environmental Engineering at the University of Zagreb, Faculty of Chemical Engineering and Technology. Her bachelor and master's theses centered on innovative water treatment methodologies aimed at eliminating contaminants of emerging concern, with a focus on photocatalytic degradation of estrogen hormones and salicylic acid mineralization via ozonation under the supervision of Prof. Hrvoje Kušić.

In 2019, driven by her interest in (waste)water treatment, Barbara joined the NOWELTIES project as an early-stage researcher. This Innovative Training Network was part of the European Union's Horizon 2020 Marie Skłodowska-Curie Actions framework. Her research primarily focused on development and optimization of natural zeolite-based adsorption technologies for removing contaminants of emerging concern from water sources. Throughout the project, Barbara spent two and a half years at the University of Belgrade, Faculty of Technology and Metallurgy in Serbia, and an additional eight months at the University of Zagreb, Faculty of Mechanical Engineering and Naval Architecture in Croatia.

Author's published works

B. Kalebić, A. Bafti, H. Cajner, M. Marciuš, G. Matijašić, L. Ćurković, Optimization of ciprofloxacin adsorption on clinoptilolite-based adsorbents using response surface methodology, *Nanomaterials* 13(4) (2023) 740.

B. Kalebić, N. Škoro, J. Kovač, N. Rajić, Regeneration of the ciprofloxacin-loaded clinoptilolite by non-thermal atmospheric plasma, *Applied Surface Science* 593 (2022) 153379.

B. Kalebić, J. Pavlović, J. Dikić, A. Rečnik, S. Gyergyek, N. Škoro, N. Rajić, Use of natural clinoptilolite in the preparation of an efficient adsorbent for ciprofloxacin removal from aqueous media, *Minerals* 11 (2021) 518.

APPENDIX A

Изјава о ауторству

Име и презиме аутора Барбара Калебић

Број индекса 4035/2019

Изјављујем

да је докторска дисертација под насловом

„Површинска модификација и функционализација природнога зеолита – клиноптилолита“

„Surface modification and functionalization of natural zeolite – clinoptilolite“

- резултат сопственог истраживачког рада;
- да дисертација у целини ни у деловима није била предложена за стицање друге дипломе према студијским програмима других високошколских установа;
- да су резултати коректно наведени и
- да нисам кршио/ла ауторска права и користио/ла интелектуалну својину других лица.

Потпис аутора

У Београду, _____

_____

APPENDIX B

Изјава о истоветности штампане и електронске верзије докторског рада

Име и презиме аутора Барбара Калебић

Број индекса 4035/2019

Студијски програм Инжењерство заштите животне средине

Наслов рада Површинска модификација и функционализација природнога зеолита – клиноптилолита / Surface modification and functionalization of natural zeolite – clinoptilolite

Ментор Проф. Др Невенка Рајић и Проф. Др Лидија Ћурковић

Изјављујем да је штампана верзија мог докторског рада истоветна електронској верзији коју сам предао/ла ради похрањена у **Дигиталном репозиторијуму Универзитета у Београду.**

Дозвољавам да се објаве моји лични подаци везани за добијање академског назива доктора наука, као што су име и презиме, година и место рођења и датум одбране рада.

Ови лични подаци могу се објавити на мрежним страницама дигиталне библиотеке, у електронском каталогу и у публикацијама Универзитета у Београду.

Потпис аутора

У Београду, _____

_____

APPENDIX C

Изјава о коришћењу

Овлашћујем Универзитетску библиотеку „Светозар Марковић“ да у Дигитални репозиторијум Универзитета у Београду унесе моју докторску дисертацију под насловом:

Површинска модификација и функционализација природнога зеолита – клиноптилолита

Surface modification and functionalization of natural zeolite – clinoptilolite

која је моје ауторско дело.

Дисертацију са свим прилозима предао/ла сам у електронском формату погодном за трајно архивирање.

Моју докторску дисертацију похрањену у Дигиталном репозиторијуму Универзитета у Београду и доступну у отвореном приступу могу да користе сви који поштују одредбе садржане у одабраном типу лиценце Креативне заједнице (Creative Commons) за коју сам се одлучио/ла.

1. Ауторство (CC BY)

2. Ауторство – некомерцијално (CC BY-NC)

3. Ауторство – некомерцијално – без прерада (CC BY-NC-ND)

4. Ауторство – некомерцијално – делити под истим условима (CC BY-NC-SA)

5. Ауторство – без прерада (CC BY-ND)

6. Ауторство – делити под истим условима (CC BY-SA)

(Молимо да заокружите само једну од шест понуђених лиценци.
Кратак опис лиценци је саставни део ове изјаве).

Потпис аутора

У Београду, _____

_____

1. **Ауторство**. Дозвољавате умножавање, дистрибуцију и јавно саопштавање дела, и прераде, ако се наведе име аутора на начин одређен од стране аутора или даваоца лиценце, чак и у комерцијалне сврхе. Ово је најслободнија од свих лиценци.

2. **Ауторство – некомерцијално**. Дозвољавате умножавање, дистрибуцију и јавно саопштавање дела, и прераде, ако се наведе име аутора на начин одређен од стране аутора или даваоца лиценце. Ова лиценца не дозвољава комерцијалну употребу дела.

3. **Ауторство – некомерцијално – без прерада**. Дозвољавате умножавање, дистрибуцију и јавно саопштавање дела, без промена, преобликовања или употребе дела у свом делу, ако се наведе име аутора на начин одређен од стране аутора или даваоца лиценце. Ова лиценца не дозвољава комерцијалну употребу дела. У односу на све остале лиценце, овом лиценцом се ограничава највећи обим права коришћења дела.

4. **Ауторство – некомерцијално – делити под истим условима**. Дозвољавате умножавање, дистрибуцију и јавно саопштавање дела, и прераде, ако се наведе име аутора на начин одређен од стране аутора или даваоца лиценце и ако се прерада дистрибуира под истом или сличном лиценцом. Ова лиценца не дозвољава комерцијалну употребу дела и прерада.

5. **Ауторство – без прерада**. Дозвољавате умножавање, дистрибуцију и јавно саопштавање дела, без промена, преобликовања или употребе дела у свом делу, ако се наведе име аутора на начин одређен од стране аутора или даваоца лиценце. Ова лиценца дозвољава комерцијалну употребу дела.

6. **Ауторство – делити под истим условима**. Дозвољавате умножавање, дистрибуцију и јавно саопштавање дела, и прераде, ако се наведе име аутора на начин одређен од стране аутора или даваоца лиценце и ако се прерада дистрибуира под истом или сличном лиценцом. Ова лиценца дозвољава комерцијалну употребу дела и прерада. Слична је софтверским лиценцама, односно лиценцама отвореног кода.